The Dissertation Committee for Meijuan Jiang Certifies that this is the approved version of the following dissertation:

Seismic reservoir characterization of the Haynesville Shale: rock-physics modeling, prestack seismic inversion and grid searching

Committee:

Kyle T. Spikes, Supervisor

Mrinal K. Sen

Robert H. Tatham

Sanjay Srinivasan

Ursula Hammes

Seismic reservoir characterization of the Haynesville Shale: rock-physics modeling, prestack seismic inversion and grid searching

by

Meijuan Jiang, B.S.; M.S.

Dissertation

Presented to the Faculty of the Graduate School of

The University of Texas at Austin

in Partial Fulfillment

of the Requirements

for the Degree of

Doctor of Philosophy

The University of Texas at Austin

May 2014

Dedication

To my family

Acknowledgements

There are many people who have helped me during my graduate studies at The University of Texas at Austin (UT). I would like to express my sincere appreciation to all of them.

First and foremost, I would like to thank my advisor Dr. Kyle Spikes. With his outstanding guidance, suggestions, and encouragement, I have had great opportunities to explore geophysics and unconventional gas shales. Kyle has always been patient, kind, and approachable whenever I had questions. He creates relaxing yet most efficient study environment, expresses praises when I make progresses, and offers encouragement and advice when I face challenges. Kyle has been a mentor, colleague, and also a friend. His guidance made my graduate studies at UT a delightful, thoughtful, rewarding and worthwhile journey.

I would like to thank my dissertation committee members, Dr. Mrinal Sen, Dr. Robert Tatham, Dr. Ursula Hammes, and Dr. Sanjay Srinivasan for their support and help on my PhD research. In particular, Dr. Sen helped me a lot with the seismic inversion, and Dr. Hammes provided composition measurements and microstructure images for one of the two wells that I studied. The committee's feedbacks and comments were very helpful in improving this dissertation.

During my graduate studies, I took many useful classes from excellent teachers. I want to express my deep appreciation to them: Kyle, Dr. Clark Wilson, Dr. Mrinal Sen,

Dr. Robert Tatham, Dr. Paul Stoffa, and Steffen Saustrup in Jackson School of Geosciences (JSG), Dr. Carlos Torres-Verdin in the Department of Petroleum and Geosystems Engineering, Dr. Farzam Javadpour in the Bureau of Economic Geology (BEG), and Dr. Jay Boisseau and John Lockman in the Texas Advanced Computing Center (TACC). The knowledge I learned from their classes has turned out to be very useful to my research.

In the past four years, I have benefited a lot from the weekly BEG-UTIG Geophysical Research Seminar in which faculty and students report their research progresses, share their research ideas, and raise their ongoing problems. Thanks to Dr. Sergey Fomel for organizing this great seminar.

There are also some staff members I want to thank. Philip Guerrero, as the graduate program coordinator, has always made sure that my class registration, forms, and graduation steps were done on time. Tom Hess provided a lot of support on commercial software, such as Hampson-Russell Software and Landmark, which I used throughout my research. Margo Grace helped me with the logistics of attending conferences and arrangement of presentations for our annual consortium meetings. Thank you all!

I enjoyed discussing research and having fun with the fellow students and postdocs at UT. Russell Carter, who has been my officemate for four years, provided help not only on my research, but also on my English. Yi Tao, Yu Xia and Tie Sun, who I have known since in college, provided my first impression of UT and JSG. They helped me with both my studies and life at UT. My thanks also go to Kwon-Taek Oh, Qi Ren,

Seismic reservoir characterization of the Haynesville Shale: rock-physics modeling, prestack seismic inversion and grid searching

Meijuan Jiang, Ph.D.

The University of Texas at Austin, 2014

Supervisor: Kyle T. Spikes

This dissertation focuses on interpreting the spatial variations of seismic amplitude data as a function of rock properties for the Haynesville Shale. To achieve this goal, I investigate the relationships between the rock properties and elastic properties, and calibrate rock-physics models by constraining both P- and S-wave velocities from well log data. I build a workflow to estimate the rock properties along with uncertainties from the P- and S-wave information. I correlate the estimated rock properties with the seismic amplitude data quantitatively.

The rock properties, such as porosity, pore shape and composition, provide very useful information in determining locations with relatively high porosities and large fractions of brittle components favorable for hydraulic fracturing. Here the brittle components will have the fractures remain opened for longer time than the other components. Porosity helps to determine gas capacity and the estimated ultimate recovery (EUR); composition contributes to understand the brittle/ductile strength of shales, and pore shape provides additional information to determine the brittle/ductile strength of the

shale. I use effective medium models to constrain P- and S-wave information. The rock-physics model includes an isotropic and an anisotropic effective medium model. The isotropic effective medium model provides a porous rock matrix with multiple mineral phases and pores with different aspect ratios. The anisotropic effective medium model provides frequency- and pore-pressure-dependent anisotropy.

I estimate the rock properties with uncertainties using grid searching, conditioned by the calibrated rock-physics models. At well locations, I use the sonic log as input in the rock-physics models. At areas away from the well locations, I use the prestack seismic inverted P- and S-impedances as input in the rock-physics models. The estimated rock properties are correlated with the seismic amplitude data and help to interpret the spatial variations observed from seismic data. I check the accuracy of the estimated rock properties by comparing the elastic properties from seismic inversion and the ones derived from estimated rock properties. Furthermore, I link the estimated rock properties to the microstructure images and interpret the modeling results using observations from microstructure images.

The characterization contributes to understand what causes the seismic amplitude variations for the Haynesville Shale. The same seismic reservoir characterization procedure could be applied to other unconventional gas shales.

Table of Contents

xi

List of Tables

List of Figures

Chapter 1: Introduction

1.1 MOTIVATIONS AND OBJECTIVES

Reservoir characterization of unconventional gas shales is challenging due to their heterogeneity and anisotropy. Shales are heterogeneous in terms of depth, thickness, rock matrix, organic maturity, porosity, permeability, pressure, temperature, and fractures. Although the estimation of reservoir properties from seismic data for conventional clastic systems has been performed for several decades, seismic characterization of gas-bearing organic-rich shales (gas shales) in terms of their reservoir properties is a young and active area of research.

The reservoir properties, such as porosity, composition, and pore shape are important for understanding the gas shales. These reservoir properties contribute to identifying zones of economic production and locating sweet spots for hydraulic fracturing. Porosity estimation helps to determine gas capacity, as well as the bulk density of shales. The pore shape distribution and composition estimations help to understand where the stiffest or softest intervals are, and along with density, more favorable for hydraulic fracturing. Estimating the reservoir properties for areas away from wells requires seismic data. The seismic responses depend on impedance contrasts, and the responses often vary spatially in the reservoirs. Understanding which rock properties or combination of properties cause these spatial variations is important.

Rock-physics models describe the relationships between reservoir properties and the elastic properties, calibrated by well log and core data at well locations. Numerous contact-theory models, empirical rock-physics relationships and inclusion-based models

have been developed. However, few of them are capable of modeling complex shales in terms of pore and grain shapes, composition, and anisotropy. Therefore, to model and understand gas shales, we must utilize more complicated and more physically representative models. In addition, most of the existing studies focus on modeling only P-wave velocity or P-impedance, whereas very few of them model both P- and S-wave velocities or P- and S-impedances simultaneously. This S-wave information is important to have because it adds another piece of independent information in the seismic reservoir characterization of the unconventional gas shales.

The main contribution of this dissertation is building a workflow to estimate the porosity, composition, and pore shape distributions of the Haynesville Shale constrained by both P- and S-wave velocities or P- and S-impedances. This workflow contains both forward and inverse calculations, including rock-physics modeling and grid searching (a grid-based modeling) at well log scale, as well as prestack seismic inversion at the seismic scale. The forward calculation is rock-physics modeling, which combines an isotropic effective medium model with an anisotropic effective medium model. The isotropic effective medium model provides a porous rock matrix with multiple mineral phases and pores with different shapes. The anisotropic effective medium model provides frequency- and pore-pressure-dependent anisotropy. The inverse calculation is grid searching, which provides probabilistic estimates of reservoir properties conditioned by the relationships between reservoir properties and elastic properties from the rock-physics modeling. Rock properties are estimated at the well log scale using P- and S-impedance logs, and at the seismic scale using prestack seismic inverted P- and S-impedances.

The variations of these estimated rock properties help to interpret the spatial variations in the seismic amplitude data, including P- and S-impedances and V_P/V_S. The results show that P- and S-impedances correlated negatively with porosity, and the V_P/V_S correlated positively with clay fraction and negatively with the pore-shape distribution and quartz fraction. These rock properties are validated through the comparisons between the elastic properties inverted from seismic data and derived from the estimated rock. The two sets of elastic properties are similar.

1.2 STRUCTURE OF THE DISSERTATION

Chapter 2 introduces the study area and the data used in the project. The geologic background of the Haynesville Shale is reviewed. The data, including prestack and poststack seismic data from a 3D seismic survey, well log data from two vertical wells, and core measurements, are described in detail. In addition, the mineral and fluid properties used in each chapter are presented in this chapter.

Chapter 3 investigates the rock-physics relationships between elastic and reservoir properties in the Haynesville Shale. An effective medium model, the self-consistent model, is applied to accommodate the composition and pore shape. The chapter shows that the physical rock properties that significantly affect the elastic properties include porosity, composition and pore shape. The best modeling results explain trends in velocity measurements corresponding to joint variations of composition and pore shape.

Chapter 4 is the most important contribution to the dissertation. It presents a workflow to invert for the reservoir properties from the elastic properties of the

Haynesville Shale. The workflow combines the isotropic self-consistent model and the anisotropic Chapman's model with a grid-search method. The self-consistent model accounts for the complex mineral grains and pores of different shapes and sizes, and Chapman's model accounts for the anisotropy of shales through aligned fractures. Both P- and S-wave velocities are modeled by the rock-physics modeling. The grid searching provides distributions of porosity, composition, and pore shapes by considering all the possible modeled solutions without bias. The feasibility of the workflow is examined at the well log scale. The porosity and composition estimations at the well location matches the observations from log and core data quite well. The pore shape estimation suggests that the pores, cracks, and fractures within the Haynesville Shale have elongated shapes.

Chapter 5 estimates the rock properties (porosity, pore shape distribution and composition) at the seismic scale by applying the workflow in Chapter 4 to the prestack seismic inversion results. It shows that all the above rock properties affect the seismic velocities, and the combined effects of these rock properties on the seismic amplitude need to be investigated simultaneously. The P- and S-impedances correlates negatively with porosity. The V_P/V_S correlates positively with clay fraction and negatively with the pore-shape distribution and quartz fraction. These estimated rock properties at the seismic scale are validated further through the comparisons between the elastic properties derived from the estimated rock properties and the ones inverted from the prestack seismic data. These correlations between the seismic amplitude variations and the rock properties contribute to the seismic reservoir characterization of the Haynesville Shale.

4

Chapter 6 presents the overall conclusions of the dissertation, as well as possible future work. The relationships between the rock properties and elastic properties of the Haynesville Shale are investigated, the rock properties are estimated with both P- and S-wave velocities or P- and S-impedances constrained, and the seismic amplitude variations are quantitatively interpreted through the rock properties. All the investigated rock properties, including porosity, pore shape and composition, affect the seismic velocities. The P- and S-impedances correlate negatively with porosity, and the V_P/V_S correlate positively with clay fraction and negatively with the pore-shape distribution and quartz fraction. The rock property derived elastic properties are very similar to the seismic inverted elastic properties, with differences less than a few percent.

This dissertation also contains several appendices: Appendix A, B, C, and D. Appendix A presents the composition percentage at different depths within the Haynesville Shale. The core analysis and XRD measurement provides accurate matrix density assumption for porosity calculation, as well as provides composition constraint for calibrating the rock-physics models. Appendix B shows another isotropic modeling work for the Haynesville Shale in addition to the self-consistent model. It uses isotropic differential effective medium (DEM) model to obtain the relationships between the P-wave velocity and porosity, pore shape and composition. The DEM modeling results are similar to the self-consistent modeling results in Chapter 3. Appendix C uses the isotropic self-consistent model and grid searching to estimate the porosity and pore shape of the Haynesville Shale. Two separate algorithms are built for estimating porosity and for estimating pore shape. In the algorithms, porosity is estimated by assuming the pore

aspect ratio, and pore aspect ratio is estimated by assuming the porosity. The porosity estimation matches with the observed porosity in terms of both overall trend and absolute value; the pore shape estimation indicates that the pores in the Haynesville Shale are mostly flattened. Appendix D shows the details of Chapman's model, which comes from Chapman (2003).

Chapter 2: Study Area and Data

This chapter introduces the study area and used data in the project. This project focused on the upper Jurassic Haynesville Shale, located in the East Texas basin of East Texas and northwestern Louisiana at the boundary between Texas and Louisiana. The data in this project came from eastern Texas, donated by BP. The prestack and poststack seismic data from a 3D seismic survey in eastern Texas, well log data from two vertical wells, and core measurements from one of the two wells were analyzed. The mineral and fluid properties are also presented in this chapter.

2.1 GEOLOGY

The Haynesville Shale is an upper Jurassic organic-rich mudrock in the East Texas basin of East Texas and northwestern Louisiana at the boundary between Texas and Louisiana (Figure 2.1). It lies stratigraphically above the Smackover formation and beneath the Cotton Valley Group (Figure 2.2). Although debate exists for the interpretation of the depositional setting and sequence stratigraphy, its general depositional environment has been suggested as an offshore setting with water depth no more than 100 m. Deposition was below wave action, in a relatively quiet environment, but susceptible to small changes in sea level (Hammes et al., 2011). This formation is relatively deep (about 3000 to 4000 m) with extremely low permeability low (less than

---

Figures 2.12–14 were published in Jiang, M., and K. T. Spikes, 2013a, Estimation of reservoir properties of the Haynesville Shale by using rock physics modeling and grid searching: *Geophysical Journal International*, **195**, 315-329. The coauthor Spikes supervised the project.

0.001 mD on average), and moderate porosity, ranging from about 3% to 14% (Wang and Hammes, 2010. Few natural fractures were apparent in core samples that we examined. However, the burial and thermal history of the Haynesville indicate high temperatures and overpressure (Ewing, 2001; Becker et al., 2010; and Nunn, 2011). The overpressure brings high initial production rate, as well as a dramatic decline rate (Hammes et al., 2011). The Haynesville Shale has been shown to exhibit vertical transverse isotropy (VTI) at the well log scale (Horne et al., 2012). At the lab scale, the pores and clay platelets are mostly aligned along the horizontal bedding direction (Chalmers et al., 2012; Curtis et al., 2010), supporting that the Haynesville Shale exhibits VTI anisotropy.

Based on Hammes et al. (2011), the facies of the Haynesville Shale include bioturbated calcareous mudstone, laminated calcareous mudstone, silty peloidal siliceous mudstone, and unlaminated siliceous organic-rich mudstone. The more calcareous areas are in the south and southwest, and the more siliceous areas are in the north and northeast of the Haynesville Shale depositional extent. The major mineralogic components are clay, quartz and calcite, and the gas capacity is estimated at more than 2.8×10^{10} m^3. The Haynesville Shale has two depocenters: one in east Texas and northwest Louisiana, and one within the East Texas Salt Basin, separated by carbonate platform (Gilmer platform) (Figure 2.3). The thickness of the Haynesville Shale varies spatially for both of the two depocenters, from less than 15 m to more than 106 m. For the eastern depocenter, the Haynesville Shale is thicker in the north and northeast and thinner in the south and west. For the western depocenter, the Haynesville Shale is thicker in the southwest and thinner in the northeast. Besides thickness, the depth of the Haynesville Shale also varies

spatially (Figure 2.4), from about 3030 m in the northeast to about 4545 m in the southwest for the eastern depocenter, and from about 4848 m in the east to about 3030 m in the west for the western depocenter.

2.2 DATA DESCRIPTION

The data used in the project includes prestack and poststack seismic data from a proprietary 3D seismic survey, well log data from two vertical wells, and core measurements from one of the two wells. The survey area and the two wells (Well A and Well B) are shown in Figure 2.5. The seismic survey area is about 4 by 4 km^2. Totally, there are 341 inlines (1001 to 1341) and 347 crosslines (2001 to 2367), with line spacing of about 12 m. Both prestack and poststack seismic data are available. Well log data from two vertical wells (Well A and Well B) are available. Well A is within the seismic block, and Well B is about 1 km east of the seismic block. Well A is the vertical pilot hole of a horizontal well, and its core data is available. The core analysis and x-ray diffraction (XRD) measurements were used to constrain the composition. The borehole environment of Well A is very rugose. Therefore, the log data from Well B was used to calibrate the rock physics model. The colors in the white square indicate the maximum negative seismic amplitudes from the base of the Haynesville Shale, with hot colors representing smaller negative values and cold colors representing larger negative values. The thick white line marks the seismic profile (crossline 2184) shown in Figure 2.6.
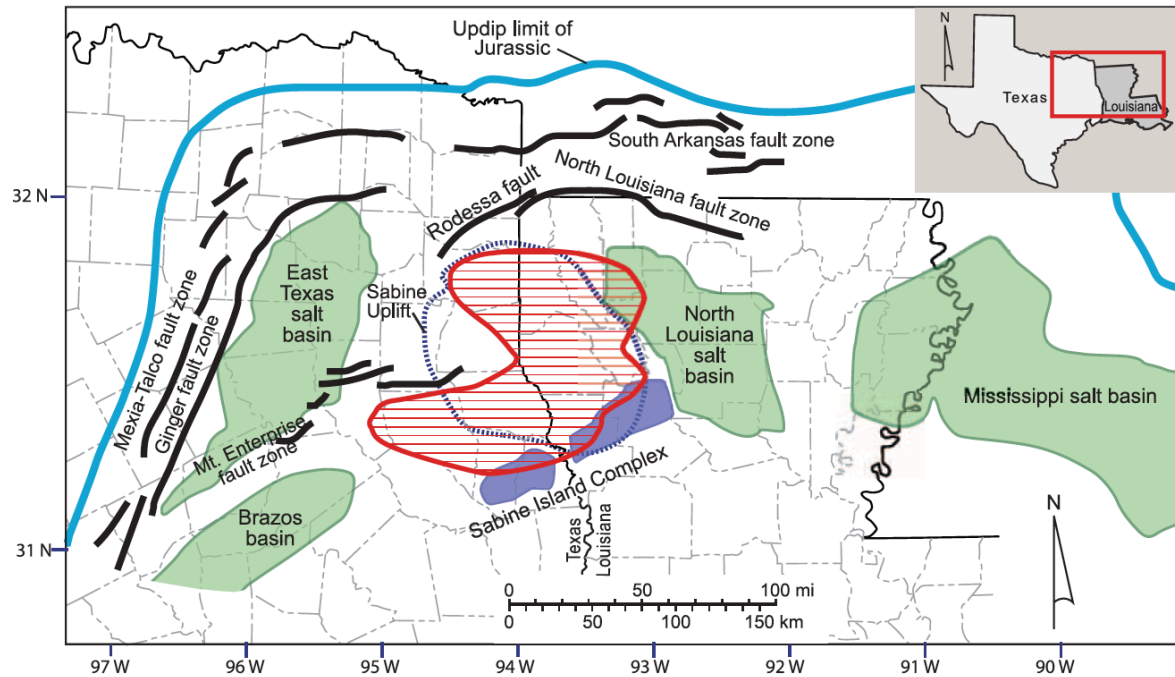
Figure 2.1: From Hammes et al. (2011), the red striped area marks the Haynesville Shale productive area as of 2010. Green areas are basins, and blue areas are structural highs. The extent of the Sabine Uplift is marked by the blue dotted area.
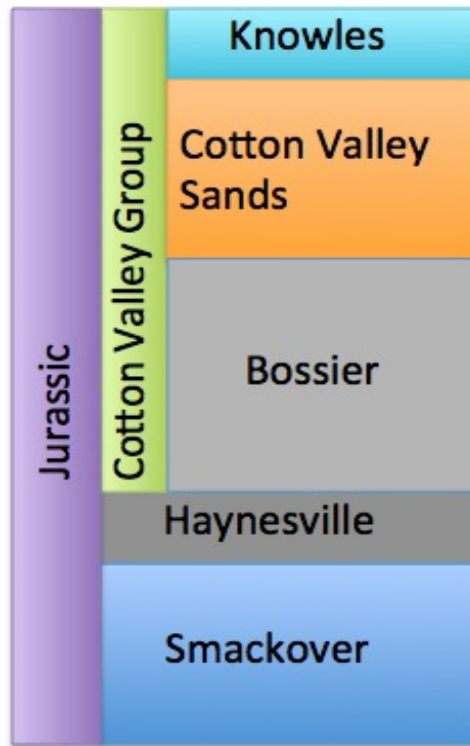
Figure 2.2: Stratigraphic column for the Haynesville Shale. The Haynesville Shale is a Jurassic-aged rock formation (about 150 Ma) below the Cotton Valley Group and above the Smackover Formation.
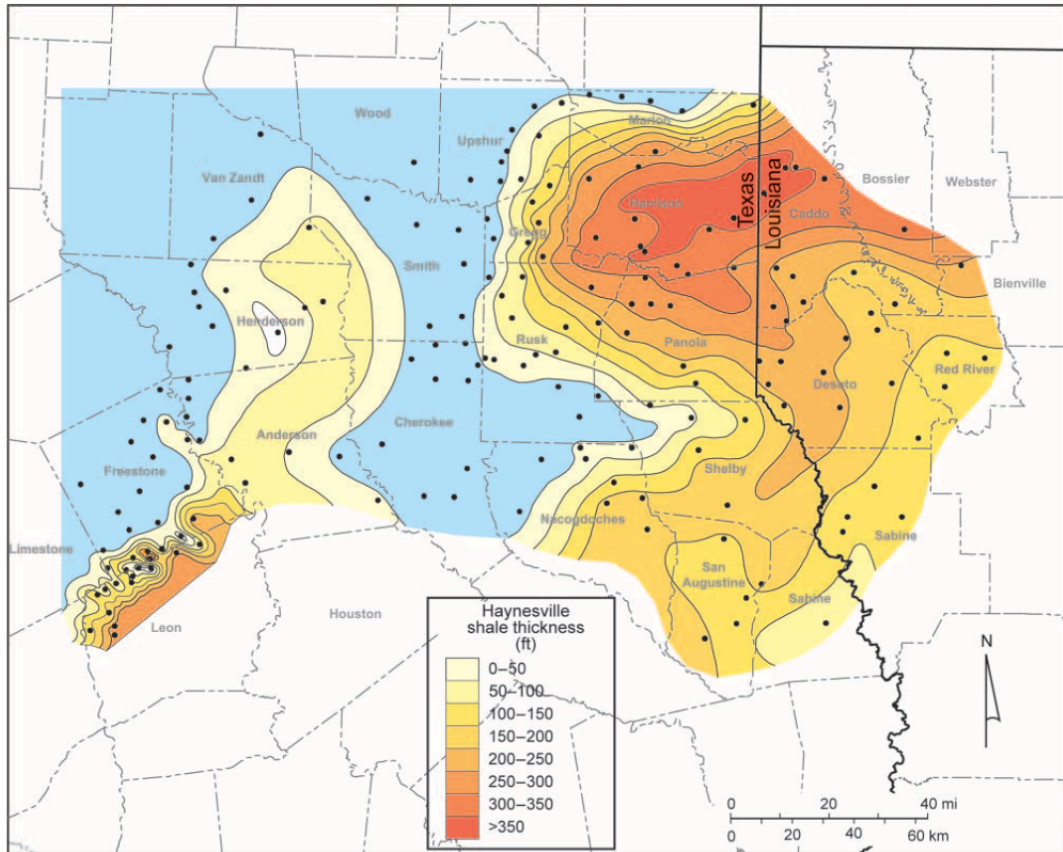
Figure 2.3: From Hammes et al. (2011), a thickness map (in ft) of the Haynesville Shale for the eastern and western depocenters. The blue area is the carbonate platform, and black dots represent well control studied in Hammes et al. (2011).
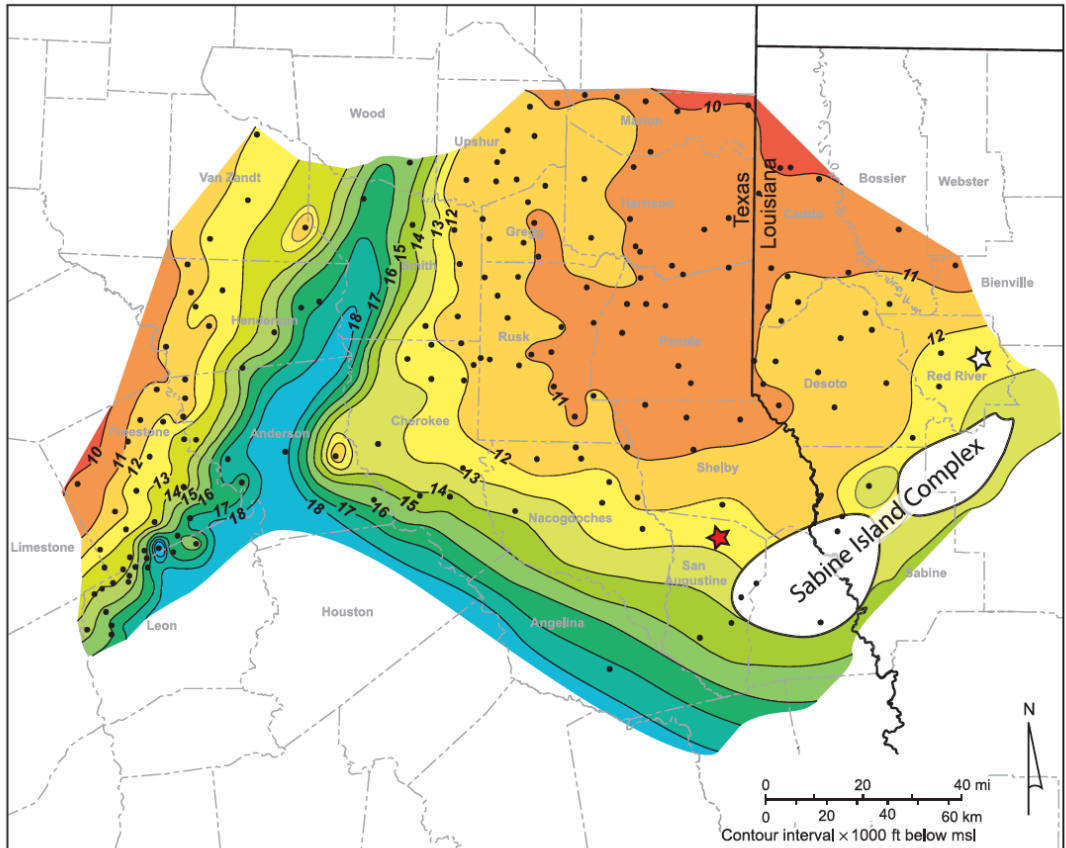
Figure 2.4: From Hammes et al. (2011), depth map of the Haynesville Shale. Shallow depths are marked by yellow and orange colors and deep depths are marked by green and blue colors. The black numbers in the map mark the depth (×1000 ft) below mean sea level.

2.2.1 Seismic Data

The 3D seismic survey area is about 4 by 4 km^2, composed of 341 inlines and 367 crosslines, and the tracing space is about 12 m. Both prestack and poststack seismic data were available in the study area. Figure 2.6 shows an example of the poststack P-wave seismic along the profile (roughly east-west direction) marked in Figure 2.5. The blue colors (Figure 2.6) represent positive amplitudes and red colors represent negative amplitudes. The Haynesville Shale top and bottom are marked by the two gray arrows at about 700 ms and 750 ms (the two-way artificial time is used due to the confidence of the true data). The bottom of the Haynesville Shale can be clearly seen by the strong positive reflection event at about 750 ms, due to the transition from the Haynesville Shale to Smackover Limestone that sits below. The top of the Haynesville Shale (~700 ms) is not as clearly seen as the bottom because the impedance contrast between the Haynesville Shale and Bossier shale is not large. More accurate identification of the top and bottom of the Haynesville Shale comes from the well log data. At the lower part of the Haynesville Shale between 720 ms and 740 ms, there is a strong negative reflection. The color intensity changes from trace to trace, indicating the amplitude of this negative reflection varies spatially. Accordingly, the colors in Figure 2.5 show the negative base of the Haynesville Shale between about 720 ms and 740 ms in the map view. The spatial variation of the P-wave seismic data can be clearly seen from the different colors.

The amplitude spectrum (Figure 2.7) was extracted from the poststack seismic data along crossline 2184, with a time range from 0 ms to 3000 ms. It shows that the dominant frequency range is 25 to 30 Hz. Assuming the average P-wave velocity within

14

the Haynesville Shale is about 3 km/s, then the wavelength is about 100 m for frequency of 30 Hz. Therefore, the vertical resolution of the seismic data, one fourth of the wavelength, is about 25 m.
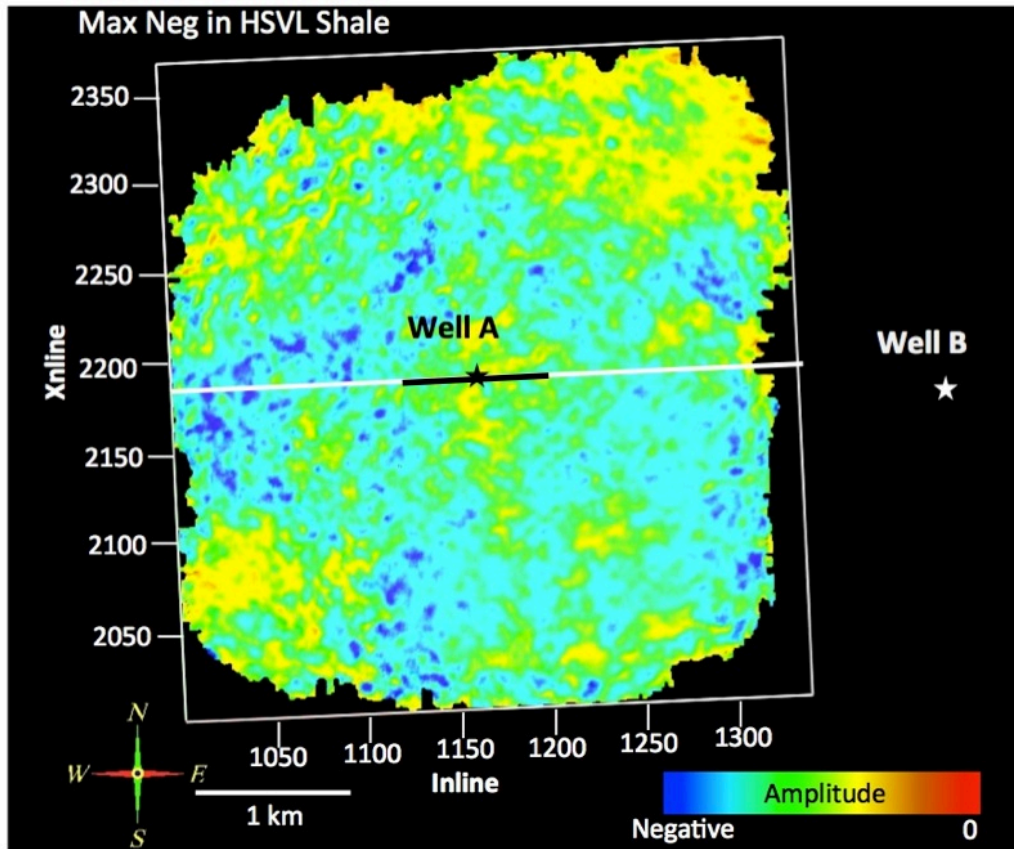
Figure 2.5: A map view showing the relative locations of the 3D seismic survey area (white block) and the two vertical wells (Well A as black star and Well B as white star). The white horizontal ticks show the crossline from 2001 to 2367, and white vertical ticks show the inline from 1001 to 1341. The thick white line marks the seismic profile (crossline 2184) shown in Figure 2.6. The black line marks the seismic profile shown in Chapter 5. The colors in the white square indicate the maximum negative seismic amplitudes from the base of the Haynesville Shale.
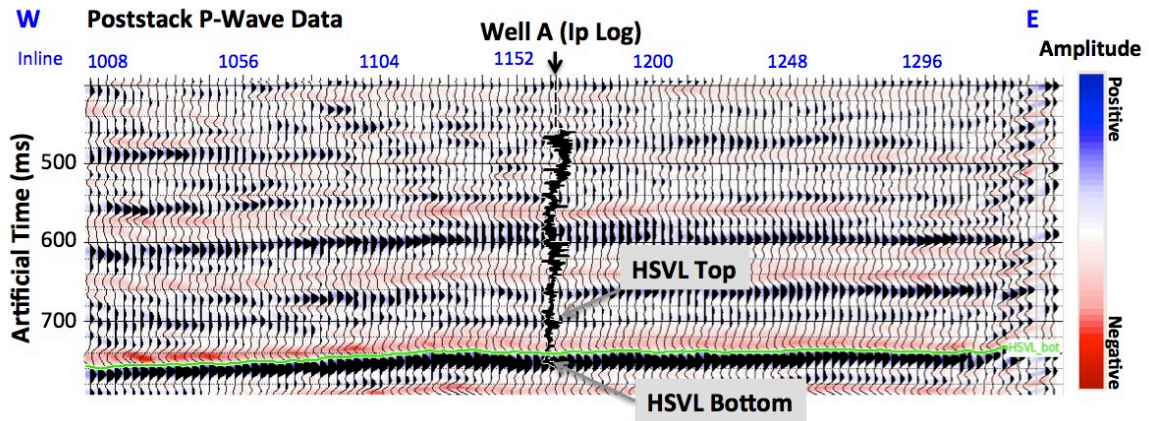
Figure 2.6: Poststack P-wave seismic data. Blue colors represent positive reflections and red colors represent negative reflections. The seismic profile is marked by the thick white line in Figure 2.5, and the profile is oriented roughly along the east-west direction. Well A is in the middle of the seismic profile, at inline 1166, with the top and bottom of the Haynesville Shale marked by gray arrows. The green curve shows the horizon at the bottom of the Haynesville Shale. The correlation coefficient of the seismic well tie was 0.79. The artificial tow-way reflection time is used to maintain confidence of the true data location.
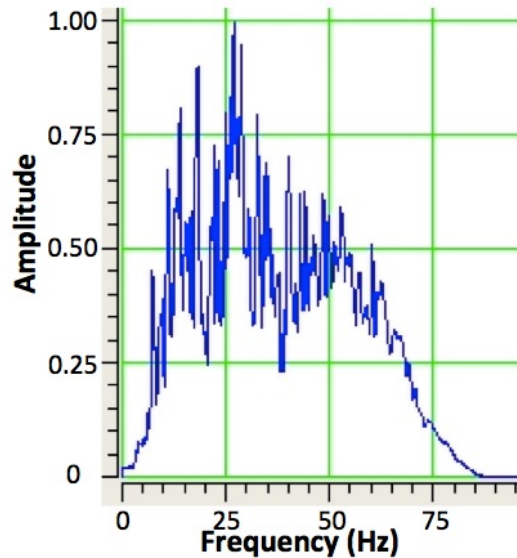
Figure 2.7: Amplitude spectrum of the poststack seismic data. The dominant frequency is about 25 to 30 Hz.

16

An example of prestack seismic data is shown in Figure 2.8. Offset gathers from three inlines (1165, 1166, and 1167) are plotted along the same crossline (crossline 2184). Well A is at inline 1166, whose P-impedance is plotted in red. The offset ranges from about 273 m to 4242 m, with increment of about 61 m. Therefore, the fold is about 66 on average. For the displayed inlines, the seismic amplitudes are larger at the far offsets than at the near offsets. Similar to the poststack seismic data, the bottom of the Haynesville Shale is indicated by the positive reflection at about 745 ms for these three inlines close to Well A. The amplitude spectrum (Figure 2.9) was extracted from the prestack seismic data along crossline 2184 between 0 ms and 3500 ms. It shows that the dominant frequency is about 25 Hz, which is similar to the one from the poststack seismic data as expected. Because there are much more traces in prestack seismic data, its amplitude spectrum looks smoother than the one from poststack seismic data. There is almost no energy from about 0 to 5 Hz in the seismic data, and the well log data provides part of the low frequency information.

Figure 2.10 shows the extracted root mean square (RMS) velocity field along the profile, which generally increases from shallow to deep formations, and with little lateral variation. Based on the RMS velocity, the CDP offset gathers was converted to angle gathers (Figure 2.11). At inline location 1166 (Well A), the angle gathers range from about 4° to 50°. Similar to offset gathers, the seismic amplitudes at larger angles are larger than the ones at smaller angles for the displayed angle gathers at the well location. The signal-to-noise ratio at the larger angles is smaller than the one at the small angles.
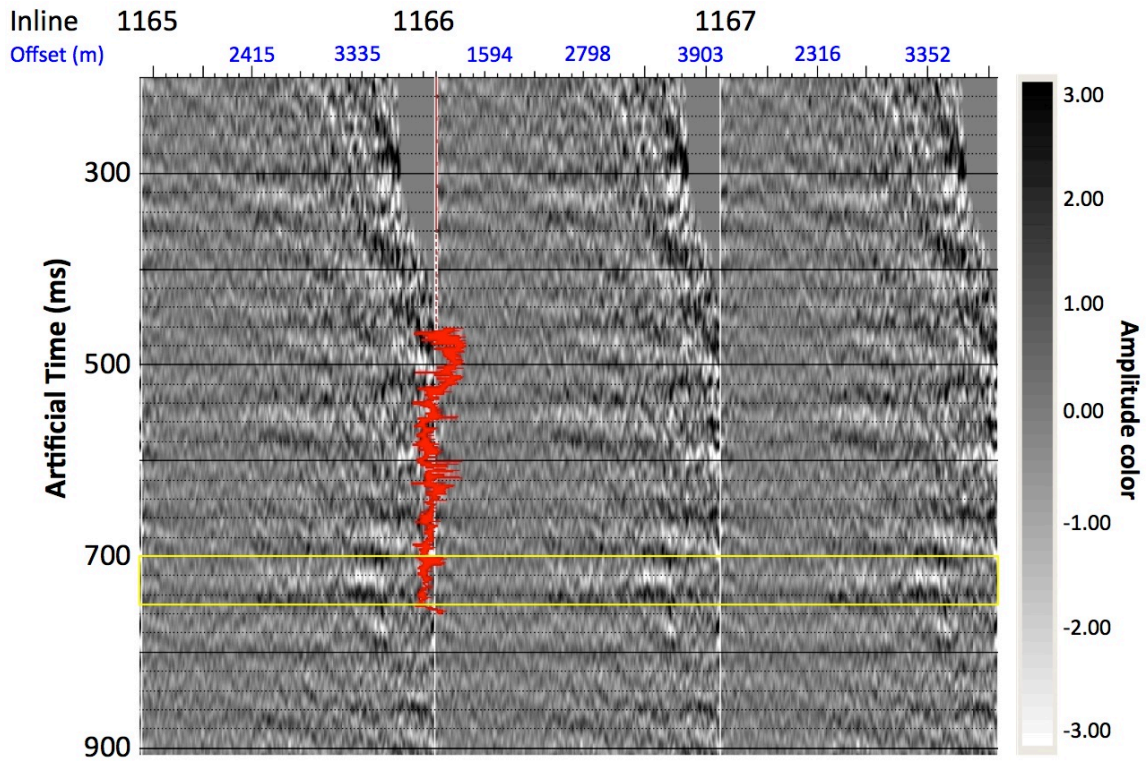
Figure 2.8: The prestack CDP offset gathers. Three CDPs along one crossline are shown with different offsets. The offset range is from about 273 m to 4242 m. The seismic amplitudes in the far offsets are larger than the ones in the near offsets. In the shallower part (above about 400 ms), the far offset gathers were muted. The red curve in the vertical direction shows the P-impedance log from Well A. The yellow box indicates the Haynesville Shale.
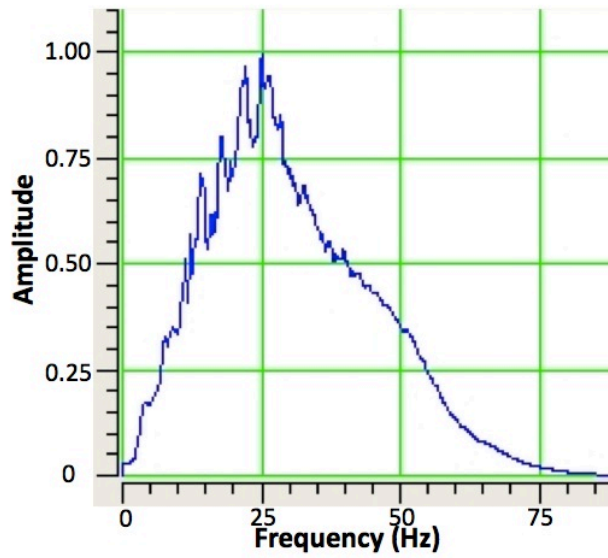
Figure 2.9: Amplitude spectrum of the prestack seismic data. The dominant frequency is about 25 Hz.
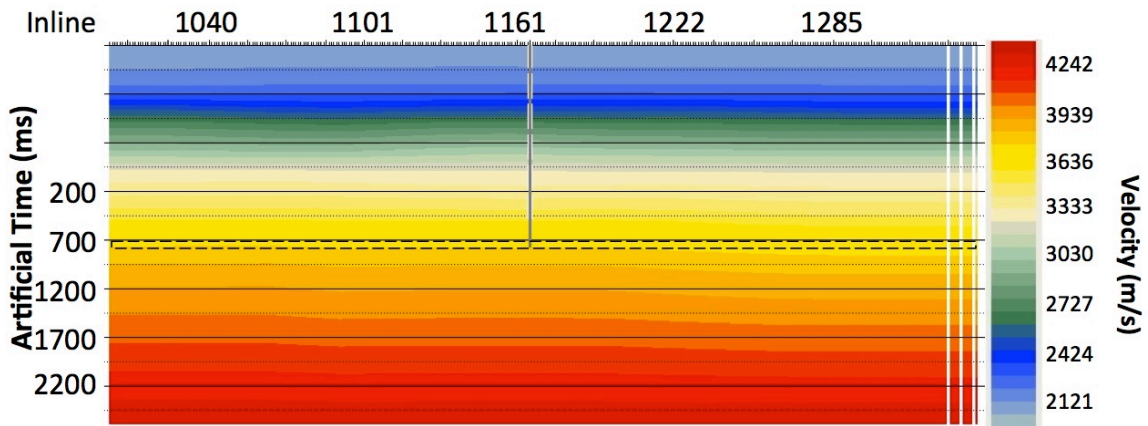
Figure 2.10: The root mean square (RMS) velocity that was used to convert CDP offset gathers to angle gathers. The RMS velocity generally increases from shallow to deep depth. The gray dashed vertical line marks the location of Well A. The black dashed square between about 700 ms and 750 ms marks the Haynesville Shale.

19
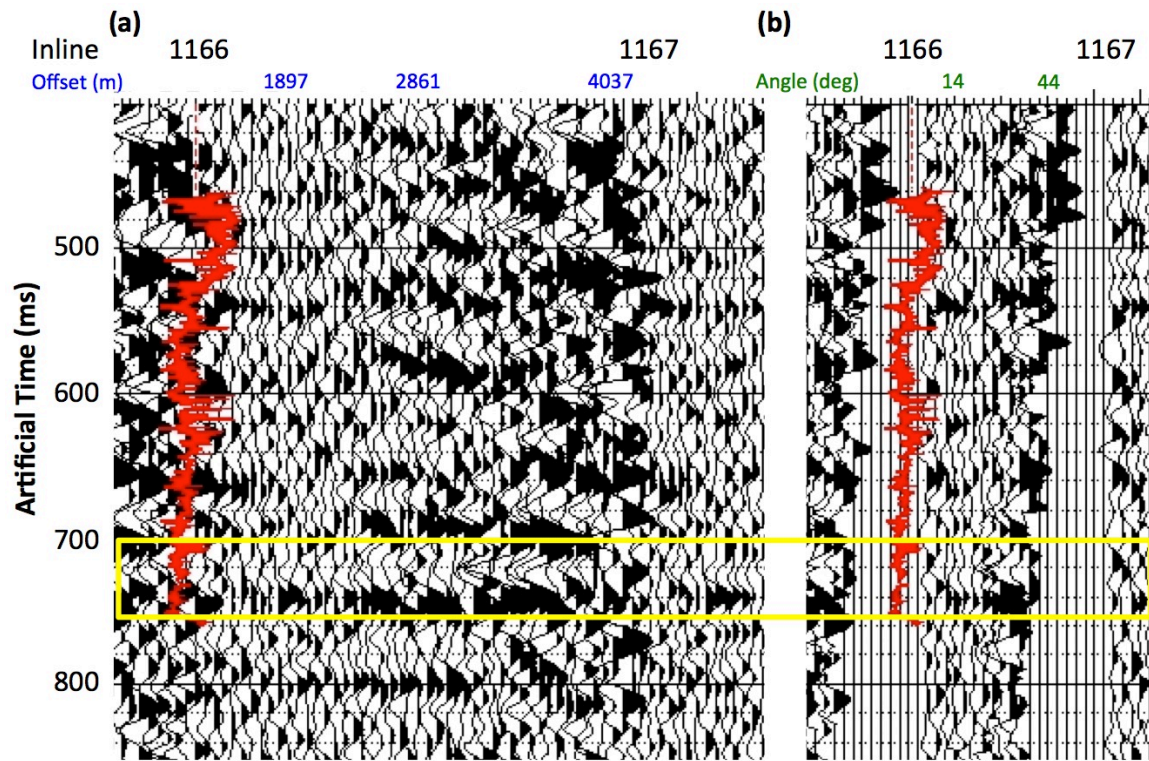
Figure 2.11: The prestack CDP offset gathers (a) and angle gathers (b). The angle gathers were calculated from offset gathers using the RMS velocity model from Figure 2.10. Similar as shown in Figure 2.8, the offset range is from about 273 m to 4242 m, and the angle range is from about 4° to 50°. The red curve in each panel shows P-impedance log from Well A. The yellow box indicates the range of the Haynesville Shael. From near to far offset or small to large angles, the seismic amplitude is increasing and the signal-to-noise ratio is decreasing.

2.2.2 Well Log Data

The logs (gamma ray, sonic, caliper, density, and resistivity) from two vertical wells (Well A and Well B) are available. The logs were edited using the caliper curve in an attempt to eliminate questionable measurements that corresponded to local borehole conditions. However, uncertainty remains in some of the data. The data from Well A comes from the vertical pilot hole through the entire Haynesville Shale of a horizontal well (Figure 2.12). Curves shown are the gamma ray, caliper, density, P-wave velocity, dipole S-wave velocity and P-impedance. Depth on the vertical axis is artificial for confidentiality purposes. The Haynesville Shale (gray shaded zone) was identified based on the increase of gamma ray log (Well A) and decrease of the density log (Well B, Figure 2.13). Overall, P- and S-wave velocities in each well show very similar pattern, and they present roughly inverse pattern from the gamma ray log. The logs from these two wells show very similar features. Well B has better data quality than Well A whose borehole environment is rugose within the Haynesville Shale as indicated by the caliper log. Therefore, the log data from Well B was used to calibrate the rock physics models. In Well A, within the Haynesville Shale formation, density varies from 2.35 to 2.64 g/cm^3 with an average of 2.49 g/cm^3, P-wave velocity varies from 2.75 to 4.42 km/s, with an average of 3.29 km/s, and S-wave velocity varies from 1.67 to 2.53 km/s, with an average of 1.97 km/s. In Well B, within the Haynesville Shale formation, density varies from 2.43 to 2.67 g/cm^3 with an average of 2.53 g/cm^3, P-wave velocity varies from 2.93 to 4.07 km/s, with an average of 3.26 km/s, and S-wave velocity varies from 1.68 to 2.47 km/s, with an average of 1.94 km/s.

21
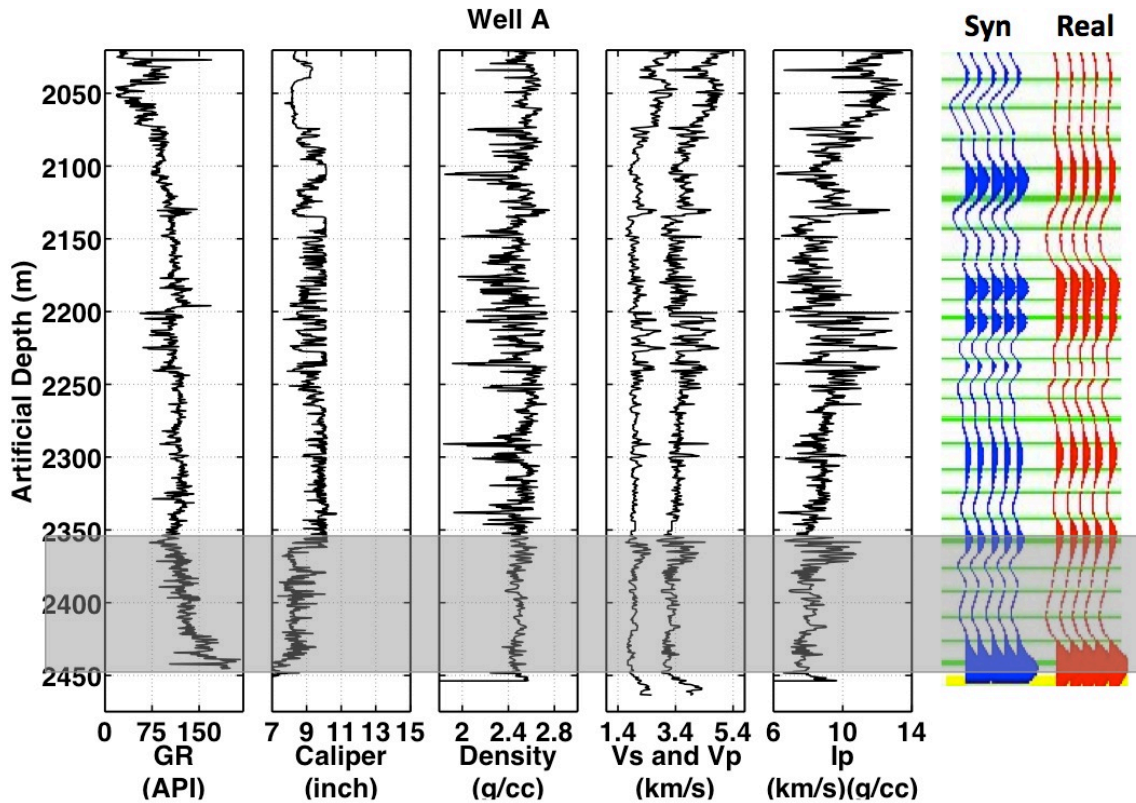
Figure 2.12: Well log data and seismic data from Well A. Gamma ray, caliper, density, P- and dipole S-wave velocities (V_P and V_S), and P-impedance are plotted. Depth is artificial for confidentiality. The Haynesville Shale is marked as the gray shaded zone. It is identified based on the increase of gamma ray log. On the right seismic data at Well A is plotted. The caliper log has many fluctuations, indicating a rugose borehole environment that causes fluctuations in the density and velocity logs. The blue seismograms are five duplicates of the synthetic seismic data, and red seismograms are five duplicates of the observed full stacked seismic data at the well location. Seismic data were tied to the well log data with a correlation coefficient of 0.79. The seismic data indicate large reflectivity at the bottom of the Haynesville Shale, whereas the top of Haynesville Shale is not as clearly identifiable as the bottom.

22
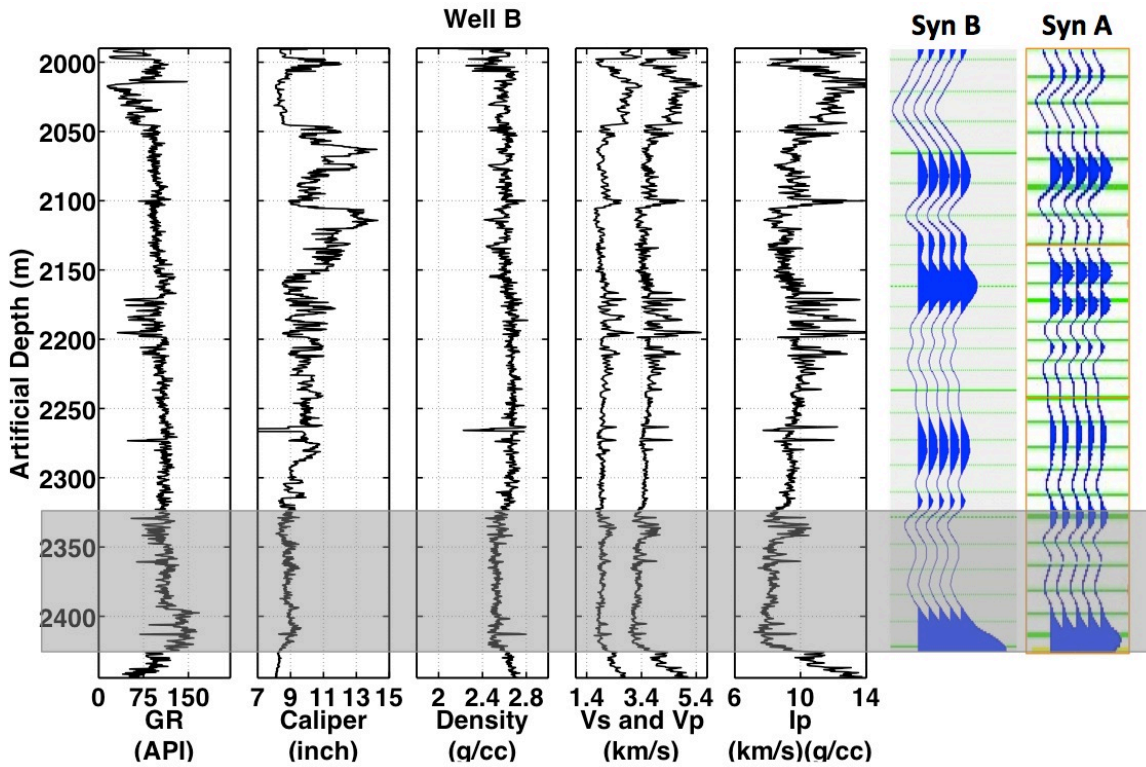
Figure 2.13: Well log data from Well B. Gamma ray, caliper, density, P- and dipole S-wave velocities (V_P and V_S), and P-impedance are plotted. Depth is artificial. The Haynesville Shale is marked as the gray shaded zone, identified by the decrease of density due to high kerogen content. Well B has better data quality than Well A. On the right, synthetic seismic data from Well B is plotted, generated by the same wavelet from Well A. Both have five duplicates. Because these two wells are close to each other (less than 3 km), their synthetic seismograms are similar.

For both wells, we generated the zero-offset synthetic seismograms from the impedance logs using the convolutional model (Yilmaz, 2001). These synthetic seismograms are plotted with the log data. In Well A (Figure 2.12), the observed poststack seismic data (red seismograms) were tied with the log data by using time-to-depth information generated by VSP travel times from an adjacent well, which was not included in this work. The observed seismic data and synthetic seismic data are very similar with a correlation coefficient of 0.79. Because no observed seismic data were available for Well B, its synthetic seismograms were compared with the synthetic ones from Well A. The same wavelet (extracted from observed seismic data at Well A) were used for both Well A and Well B. Because the impedance log of Well A fluctuated due to the rugose borehole environment, the synthetic seismogram for Well A contained higher frequencies than the one from Well B. The seismic data indicate a large reflectivity difference between the Haynesville Shale and the underlying Smackover Limestone due to the large increase of P-wave velocity and density. However, the boundary between the Hayesville Shale and Bossier Shale is not as clearly defined as the one between the Haynesville Shale and Smackover Limestone.

In this project, the porosity log was calculated using

$$\phi = \frac{\rho_m - \rho_b}{\rho_m - \rho_{fl}} \qquad (2.1)$$

as a function of measured density log (ρ_b), density of the rock matrix (ρ_m), and density of the pore fluid (ρ_{fl}). The pore fluid density was computed as an arithmetic average of the water and gas densities, weighted from the water saturation and gas saturation calculated

from the resistivity log. In the early stage of this study, the rock matrix was assumed to be calcite (Chapter 3 and Appendix B). Later on, the rock matrix was updated to the combination of different minerals from core analysis and XRD measurements Chapters 4 and 5, and Appendix C) to more accurately represent the shale.

2.2.3 Core Data

In addition to log and seismic data, Well A also has cores, providing both composition percentages and scanning electron microscope (SEM) images (courtesy Dr. Ursula Hammes).

2.2.3.1 Composition Percentage

Core analysis and x-ray diffraction (XRD) measurements were done for composition percentage on forty-eight samples within the Bossier and Haynesville Shale formations at about a 3-m interval (Appendix A, courtesy Dr. Ursula Hammes). Among these 48 samples, 20 samples were for Bossier and 28 samples were for Haynesville Shale. Both the Bossier and Haynesville Shales contain quartz, feldspar (potassium feldspar), plagioclase (calcium feldspar), calcite, dolomite, pyrite, kerogen and clay (Figure 2.14). A clear boundary exists between the Bossier and Haynesville Shale due to the composition change at about 2350 m. From the Bossier to the Haynesville, the average quartz percentage increases from 28.9% to 31.6%, average calcite percentage increases from 4.8% to 14.2%, average kerogen percentage increases from 1.2% to 5.3%, and average clay percentage decreases from 56.1% to 35.3%. In general, the Haynesville

Shale is richer in organic matter but contains less clay than the Bossier Shale, with an accompanying increase in carbonate.
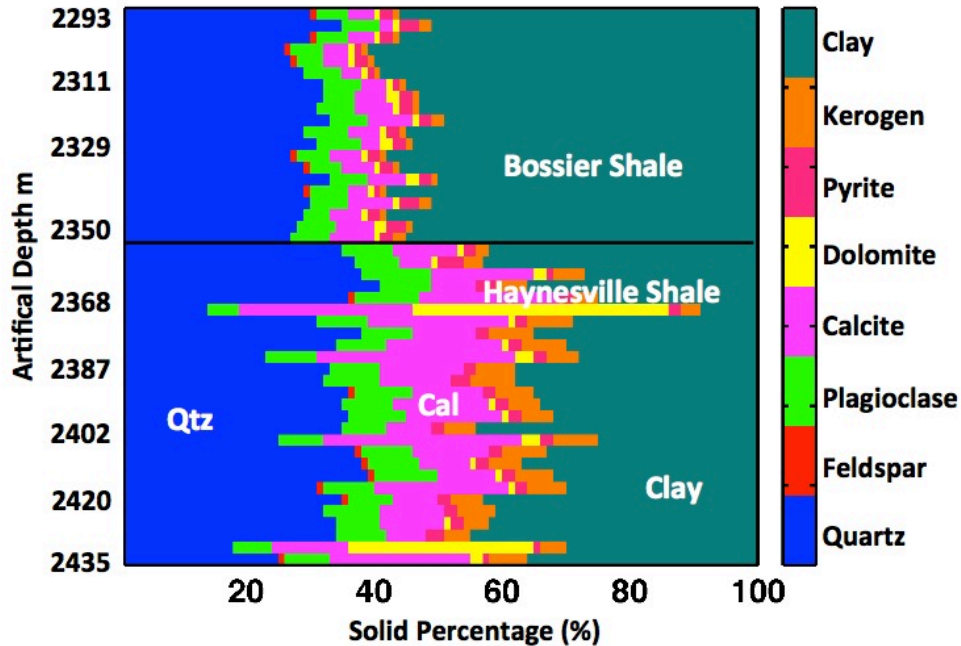
Figure 2.14: Mineralogic composition of the Bossier and Haynesville Shale from core analysis and XRD (in volume) for Well A. The depth scale is not linear because the 48 samples were not measured at exactly equal spacing along depth. A clear boundary exists between Bossier and Haynesville Shale due to the increase of quartz, calcite and kerogen and the decrease of clay at about 2350 m.

Because core analysis and XRD measurement was done at every 3 m, whereas log data was measured at a 0.15-m interval, we interpolated the 28 samples linearly within the Haynesville Shale formation when calculating the porosities in Chapters 4 and 5, and Appendix C.

2.2.3.2 Microstructure Images

At the micro- and nano-scales scale, the Haynesville Shale tends to have flattened or elongated grains and pores (Curtis et al., 2010; Chalmers et al., 2012). Figure 2.15a (from Curtis et al., 2010) is a back-scatter electron (BSE) image that shows the microstructure of the Haynesville Shale. Overall, the pores and the clay platelets appear flat and elongated, aligned along the bedding direction. The field emission scanning electron microscope (FE-SEM) image (Figure 2.15b) shows that the interparticle pores around quartz grains and macropores created from dissolution of carbonate matrix or cement are aligned horizontally (Chalmers et al., 2012).

The porosity in the Haynesville Shale is mostly interparticle along the quartz or calcite grains (Figure 2.16). The SEM image from a sample of Well A at artificial depth of 2434 m (Figure 2.16a) shows a lot of quartz grain related interparticle pores. Similarly, the field emission scanning electron microscope (FE-SEM) image of the Haynesville Shale (Figure 2.16b) from Chalmers et al. (2012) shows that at the given scale and resolution, the porosity in the Haynesville Shale is mostly interparticle, sitting in between quartz grains. Besides the interparticle pores associated with quartz or calcite grains, the Haynesville Shale also contains other types of pores (Figure 2.17), such as moldic porosity, pores in the organic matter, pores associated with clay mineral grains, and pores between the crystals of pyrite framboids.
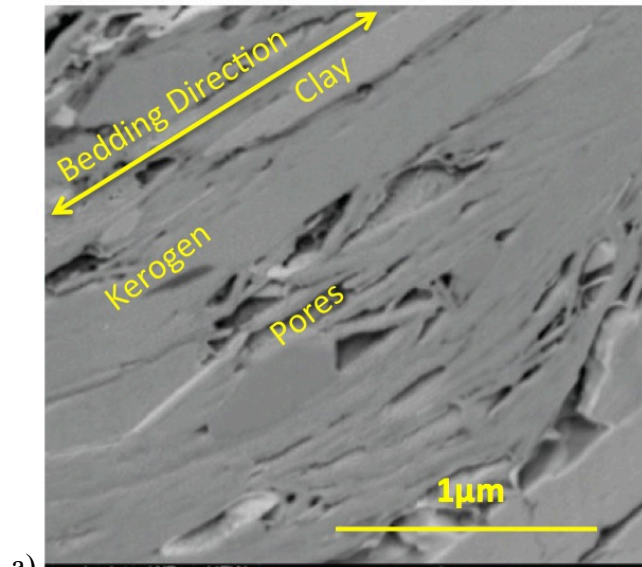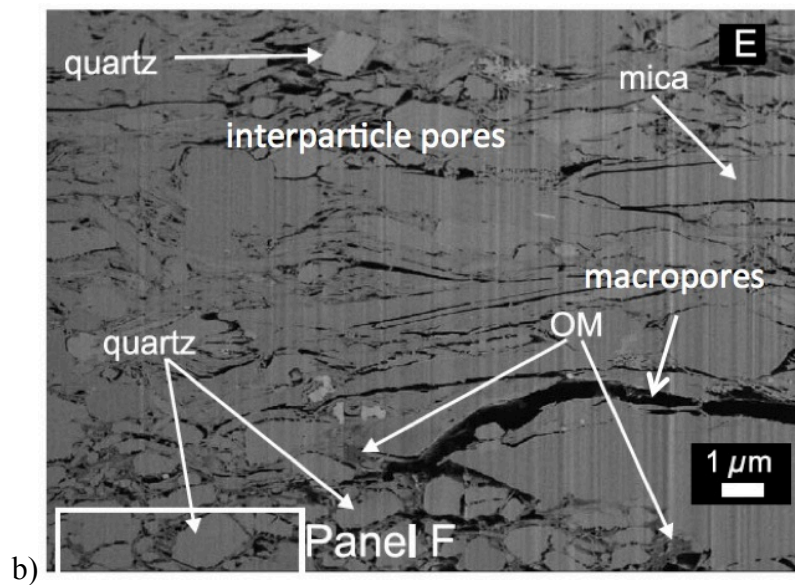
Figure 2.15: a) From Curtis et al. (2010). A back-scatter electron (BSE) image showing the microstructure of the Haynesville Shale. The clay platelets and pores are elongated, aligned along the bedding direction. b) From Chalmers et al. (2012). A field emission scanning electron microscope (FE-SEM) image of the Haynesville Shale. The macropores are created from dissolution of carbonate matrix or cement. The pores are mostly interparticle, and are aligned horizontally. Quartz, mica, and organic matter (OM) can also be observed from the image.
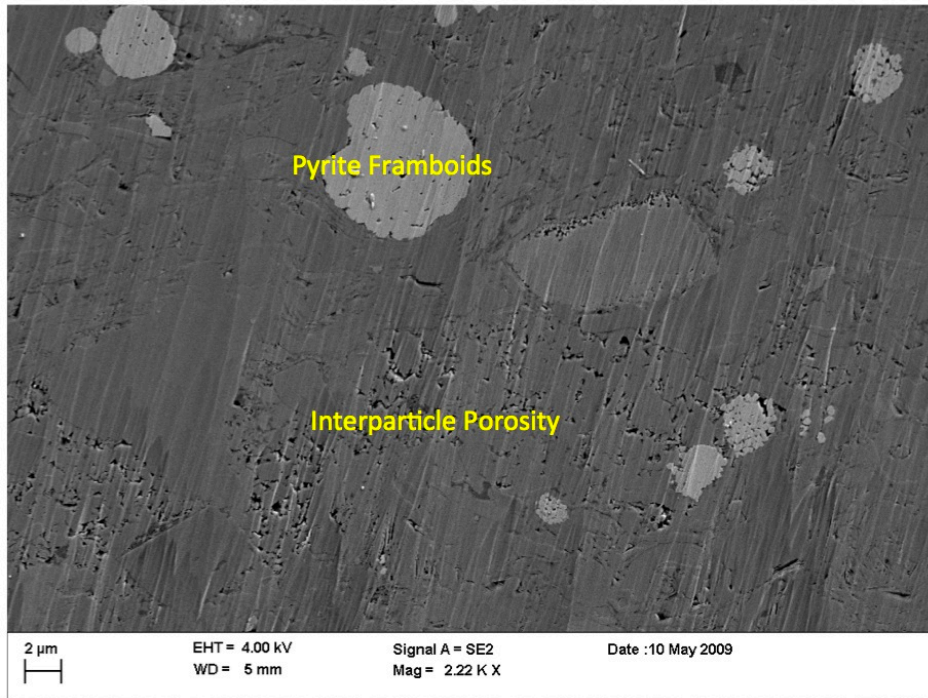
a)
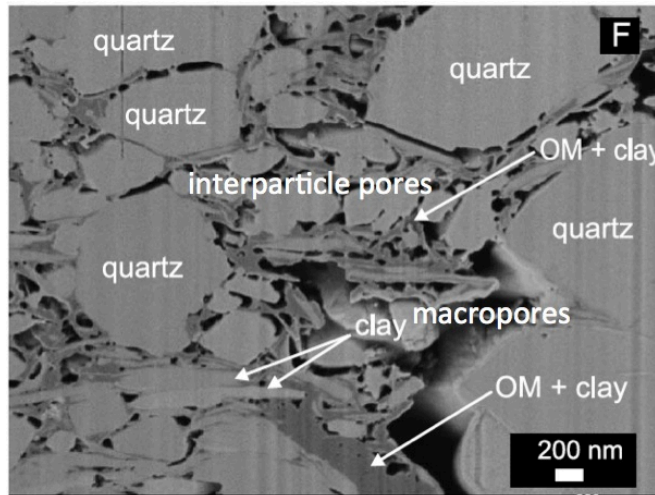
b)

Figure 2.16: a) Courtesy Dr. Ursula Hammes. A Ar-ion milled scanning electron microscope (SEM) image of the Haynesville Shale. The sample is from Well A at artificial depth of 2434 m. Most of the pores are interparticle pores, related to quartz or calcite grains. The very bright spots are pyrite framboids. b) From Chalmers et al. (2012). A field emission scanning electron microscope (FE-SEM) image of the Haynesville Shale. At the given scale and resolution, the porosity in the Haynesville Shale is mostly interparticle, sitting in between quartz grains.

29
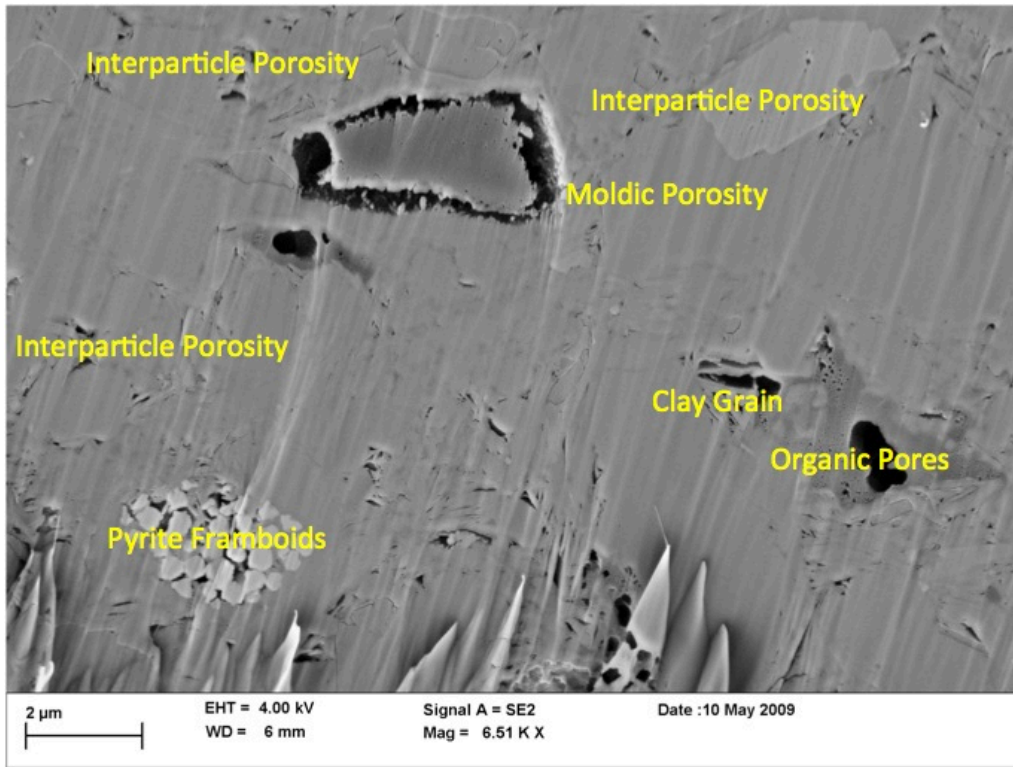
Figure 2.17: Courtesy Dr. Ursula Hammes. A scanning electron microscope (SEM) image of the Haynesville Shale. The sample is from Well A at artificial depth of 2434 m. The image shows moldic porosity, interparticle pores associated with quartz grains and clay mineral grains, pores associated with organic matter, and pores between the crystals of pyrite framboids.

2.3 MINERAL AND FLUID PROPERTIES

In the rock physics modeling, the effective moduli and density of the shale depend on the moduli of each inclusion, including solid and fluid inclusions. Table 2.1 lists these properties used in my early research stage (Chapter 3 and Appendix B) and table 2.2 lists these properties in my later research stage (Chapters 4 and 5, and Appendix C). The main difference between the two tables comes from the elastic properties for clay, kerogen and

30

fluids that are less certain. The elastic properties for quartz, calcite, pyrite, and dolomite are relatively well-known.

Table 2.1. Moduli and densities of the solids and fluids (Chapters 3 and Appendix B) (Mavko et al., 2009; Ward, 2010; Lucier et al., 2011)

Mineral/Fluid	Density (g/cm^3)	Bulk modulus (GPa)	Shear modulus (GPa)
Quartz	2.65	36	45
Calcite	2.71	69	33
Clay	2.58	18	7
Pyrite	4.93	147.4	132.5
Kerogen	1.3	7	4
Water	1.29	2.8	N/A
Gas	0.16	0.07	N/A
Dolomite	2.87	45	95

Table 2.2. Moduli and densities of the solids and fluids (Chapters 3, 4 and Appendix C)

Mineral/Fluid	Density (g/cm^3)	Bulk modulus (GPa)	Shear modulus (GPa)
Quartz	2.65	36.6	45
Calcite	2.71	69	33
Clay[4, 5]	2.58	21	7
Pyrite	4.93	147.4	132.5
Kerogen[1,2,3]	1.45	2.9	2.7
Brine	1.09	2.8	N/A
Gas	0.16	0.07	N/A

Chapter 3: Rock-physics relationships between elastic and reservoir properties in the Haynesville Shale

3.1 ABSTRACT

Modeling the elastic properties of the Haynesville Shale using rock-physics techniques is part of characterizing this shale that could be used to improve predictions of economic drilling locations. The goal of this modeling is to relate the reservoir properties of interest (e.g., porosity, pore shape, and composition) to the elastic properties. Rock physics modeling for conventional reservoirs has similar goals, but the modeling approach for shale is more complex. Within the Haynesville Shale, the physical rock properties that significantly affect the elastic properties include not only porosity, but also include composition and pore shape. Accordingly, the rock-physics modeling requires an effective-medium theory, notably the self-consistent model, to accommodate the composition and pore shape. Composition was estimated through a combination of well log and core data. Pore shapes were estimated using estimated stress conditions and numerical studies. The best modeling results explain trends in velocity measurements corresponding to correlated variations of composition and pore shape. Accordingly, this rock-physics model could be used in conjunction with seismic data interpretation to identify locations with low velocity and potentially higher organic content and zones with faster velocity more suitable for fracturing.

3.2 INTRODUCTION

For the last several decades, measurements of seismic data have been related to lithology, porosity, and fluid content and volume for reservoir characterization. The most successful applications have been for reservoirs consisting of clean sandstones, clay-bearing sandstones, and to some extent carbonate rocks. However, a similar approach for gas shale has not been explored extensively, particularly in the Haynesville Shale, likely because of the relative lack of experience with shale plays and their natural complexity. The goal of modeling velocity data using a rock-physics model or transform is to relate the reservoir properties to the elastic (seismic) properties. This is important, especially in North America, because of the need to identify locations from surface seismic observations where hydrocarbon production in shale may be optimal.

Rock-physics modeling in clastic reservoirs relates the measured compressional and shear velocity to the porosity, lithology or mineralogy, fluid type, and volume. One reliable approach is to apply an empirical law derived from laboratory measurements of velocity and reservoir properties (Tosaya, 1982; Greenberg and Castagna, 1992). These laws typically are for very specific lithologies, fluids, and porosity ranges. In addition, theoretical models have been developed (Mindlin, 1949; Dvorkin and Nur, 1996; Norris and Johnson, 1997; and Jenkins et al., 2005) to approximate sands with spherical particles under different conditions of grain-to-grain contacts and normal and tangential stresses. Carbonate reservoirs tend to be more complex, in which pore type and fractures are added to the list. Rock-physics models applicable to carbonate reservoirs also include empirical laws. Theoretical models can account for fractures (e.g., Hudson, 1980;

Schoenberg and Douma, 1988), different porosity types (Eberli et al., 2003) and in some cases for both fractures and porosities (Chapman, 2003).

For clastic and carbonates systems, typically the lithology is fairly well constrained, and petroleum systems analyses have helped to predict fluid migration pathways. Gas shales may be composed of a much wider range of lithologies than either clastic or carbonate reservoirs, and in particular kerogen or organic matter. Furthermore, fractures (both in situ and induced) may prove to provide a significant role in some shale plays (Gale et al., 2007). One advantage in terms of characterizing gas shales is that the fluid type might be better known from regional information compared to either a clastic or carbonate system because these shales are often the source rocks for themselves and for formations in close stratigraphic proximity. However, predicting the volume of the fluid is difficult because it depends on the kerogen type and quantity.

This chapter shows a modeling routine in the Haynesville Shale to relate the composition, pore stiffness, and fluid content to the velocity and density through an effective-medium model. An effective-medium model is one that characterizes a complex medium, whether it is heterogeneous and/or anisotropic, as a single homogeneous (and potentially isotropic) medium. In terms of seismic velocity and resolution, this can be considered as finding a single seismic velocity that represents multiple layers (each with different velocities and each below seismic resolution) as a single layer. A correct application of an effective-medium model results in identical seismic responses if either the original layers were in place or if the effective-medium model replaced them. More specific to our purposes, seismic velocities are affected by composition, pore shape, fluid

34

content, grain shape, grain contacts, pore size, and fluid distribution, among others. These are inputs into the effective medium model. The outputs are effective elastic properties that can be compared with measured seismic velocity.

The effective-medium model chosen in this chapter is the *n*-phase self-consistent approximation (SCA) of Berryman (1980, 1995). It links the composition, total porosity, and fluid saturation to the elastic properties by mixing together matrix components and pores, each with different shapes. Composition was estimated from observations from core data. Pore shapes were estimated from in situ stress and numerical experimentation. SEM images could be used if available. We use a statistical formulation of the model by implementing distributions of solid and pore aspect ratios to extend the possible ranges of velocity values to match the well data.

Modeling results for two wells provide different sets of theoretical model curves that explain the data in terms of variable composition, variable distributions of pore shapes, and a combination of the two. One major limitation of this model is that it is isotropic and does not account for anisotropy of shales, whereas shales are anisotropic due to the alignment of clay platelets, pores, and/or fractures. Other limitations of this model are that it includes neither temperature nor pressure variations. Furthermore, grain and pore shapes are approximated with regular, geometrically convenient shapes. These approximations, and the lack of pressure and temperature parameters, prevent us from incorporating diagenetic effects likely present in the shale. Despite these limitations, this work, consistent with present knowledge, ultimately could be applicable to field seismic data to identify locations within the Haynesville Shale that contain more organic material,

35

which might be more productive. This may be in contrast to more brittle zones where hydraulically induced fractures might remain open for longer durations, thus increasing permeability. The modeling here does not attempt to explain every single point measurement; rather, model trends in the data. The disadvantage of this approach is that the rock-physics model does not provide a succinct combination of reservoir properties for every velocity. The advantage is that the modeling of the trends allows for extrapolations to other rock-property combinations not necessarily observed in the data. This is important for quantitative interpretation of surface seismic data when rock property combinations in between wells may not be represented at well locations.

Measurements of seismic wave velocity acquired in a laboratory setting, in a wellbore, or from field seismic data (crosswell, VSP, or surface) are dynamic measurements. The dynamic bulk and shear moduli are computed from seismic wave velocity and density. Alternatively, values of elastic moduli can be obtained by deforming the rock with a known applied stress. In general, the dynamic values are greater than the static values. The difference typically is attributed to anelastic effects during deformation as opposed to elastic deformation during seismic wave propagation. The modeling performed in this work is done based on measurements of dynamic P-wave and S-wave velocities, and thus dynamic elastic properties are modeled. However, it should be noted that the static properties (i.e., the geomechanical properties) are of interest for drilling applications and hydraulic fracturing in shale (Sayers, 2010). To relate the dynamic properties to static properties, a transformation must be performed.

The focus here is not in this transformation; rather, we concentrate on the dynamic moduli and relate the measured velocities to shale reservoir properties.

3.3 THE SELF-CONSISTENT APPROXIMATION

To investigate the effects of pore shape and composition, we modeled observations from well-log data in the Haynesville Shale using the self-consistent approximation (O'Connell and Budiansky, 1974; Berryman, 1980). Contact-theory models (e.g., Norris and Johnson, 1997) and empirical rock-physics relationships (e.g., Greenberg and Castagna, 1992) do not provide the flexibility to model heterogeneous compositions or specific distributions of pore shapes. The self-consistent approximation (SCA) is not limited to specific compositions. It is capable of modeling multiple mineralogical phases, as well as approximations to their shapes and spatial distributions, for an elastically isotropic rock. Similar models exist that could be used for modeling isotropic distributions of solid materials and pores. These include the Kuster-Toksöz model (e.g., Kuster and Toksöz, 1974; O'Connell and Budiansky, 1974) and differential effective media (DEM, Norris, 1985). The DEM models two-phase composites. The inclusion phase is incrementally added into the matrix phase, and the order of adding in phase affects the effective moduli of the rock. Yet the SCA is a multiple-phase model, and the order of adding in phases does not affect the effective moduli of the rock.

The generalized version of the SCA provides the use of *n* phases, including multiple solid and multiple pore-space phases (equations 3.1–3.2). These two equations must be solved iteratively to find the yet-to-be determined values of K_{SC}^* and μ_{SC}^* (the

37

self-consistent or effective bulk and shear moduli, respectively) as a function of the volumetric quantities and elastic moduli of the constituents.

$$\sum_{j=1}^{N} f_j (K_j - K^*_{SC})\beta^{*j} = 0,$$ (3.1)

$$\sum_{j=1}^{N} f_j (\mu_j - \mu^*_{SC})\zeta^{*j} = 0.$$ (3.2)

Each j denotes a phase, either a material or pore space, with a corresponding volume fraction f_j and bulk (K_j) and shear (μ_j) modulus for that phase. The shapes of all grains and pores to be modeled must also be described. Every grain and pore is considered to be an ellipsoidal-shaped inclusion. The shape is described by the aspect ratio (α), which is the ratio of the shortest to the longest axis. We considered only prolate ellipsoidal inclusions where $\alpha \leq 1$. The factors β^{*j} and ζ^{*j} (equations 3.3 and 3.4) describe the geometry of an inclusion made of phase j within a background medium (denoted with the m subscript).

$$\beta^{*j} = \frac{K_m + \frac{4}{3}\mu_j}{K_j + \frac{4}{3}\mu_j + \pi\alpha\mu_m \frac{3K_m+\mu_m}{3K_m+4\mu_m}}$$ (3.3)

$$\zeta^{*j} = \frac{1}{5}\left[\frac{8\mu_m}{4\mu_j + \pi\alpha\mu_m\left(1 + 2\frac{3K_m+\mu_m}{3K_m+4\mu_m}\right)} + 2\frac{K_j + \frac{2}{3}\left(\mu_j + \mu_m\right)}{K_j + \frac{4}{3}\mu_j + \pi\alpha\mu_m \frac{3K_m+\mu_m}{3K_m+4\mu_m}}\right]$$ (3.4)

Then the seismic velocities can then be calculated from the effective bulk and shear moduli and density (equation 3.5).

$$V_P = \sqrt{\dfrac{K_{SC}^{*} + \dfrac{4}{3}\mu_{SC}^{*}}{\rho}}$$

$$V_S = \sqrt{\dfrac{\mu_{SC}^{*}}{\rho}} \qquad\qquad (3.5)$$

Figure 3.1 is a schematic illustration of the self-consistent model. A rock to be modeled (the circle) is embedded in an infinite matrix (the square). The rock consists of isolated mineral grain inclusions (white ellipses) and pore inclusions (black ellipses) with different aspect ratios. The self-consistent elastic moduli of the rock depend on the elastic properties of the solid and pore inclusions.

Figure 3.1: Illustration of the self-consistent model. The square represents an infinite matrix with a given effective moduli, and the circle represents a rock. Inside the rock, white ellipses represent mineral grain inclusions, and black ellipses represent pore inclusions. The elastic moduli of the rock and the infinite matrix depend on the elastic properties of grain and pore inclusions. The moduli of the infinite matrix and rock are made the same by iteratively solving for the effective elastic moduli.

The SCA isolates the pores from each other, so they are not in hydraulic communication. As a result, this model is considered to be high frequency. High frequency in this case refers to seismic wave propagation and pressures within the pore

space. More specifically, as a seismic wave passes through the rock, pore pressures within the pore space do not have sufficient time to equilibrate during one wave period. The effect is that pore space acts more stiffly, and the rock as a whole behaves as if it is stiffer than it would be if a low-frequency wave propagated through the rock. If the pores are in hydraulic communication (connected porosity), and the frequency is low, then the pore space stiffness will not be affected by the fluid.

3.3.1 Model Parameters: Composition

Visual examination of cores from a well drilled through the Haynesville Shale does not reveal distinct lithologies, fluid content, or pore structure. In addition, vertical natural fractures were not observed in the cores that we observed. Core analysis and XRD data provided a range of mineralogies (Figure 2.14). The structure of the shale has been observed in terms of size and shapes from micro- and nano-scale imaging techniques (Curtis et al., 2010). Accordingly, the rock-physics modeling we perform combines variations in likely lithologies. Modeling velocities with different mineral assemblages requires defining the elastic properties of each mineral constituent. The minerals chosen to model (guided by the core analysis and XRD data) include kerogen, clay, quartz, calcite, and pyrite. The latter three have relatively well-known values (Table 2.1) for their mineral moduli and density (Mavko et al., 2009). On the other hand, kerogen and clay have very poorly determined elastic moduli and density, but published information provides some useful values (Ward, 2010; Lucier et al., 2011).

3.3.2 Model Parameters: Pore Shapes

To model pore shapes with different aspect ratios, we first determined a minimum and maximum α that could be present at the depths under consideration. Pores will be closed at different depths because of effective stress, depending on the aspect ratio. Images of pores (Curtis et al., 2010) illustrate that in the Haynesville Shale, elongated and isolated pores exist at the nano- and micro-scales that appear to be open. Thus, the range of aspect ratios is designed to include these. An analytical expression (equation 3.6) relates the confining stress needed to close a single, isolated ellipsoidal pore to its aspect ratio and an infinite elastic solid surrounding that pore (Mavko et al., 2009). In this equation, σ_0 is the confining stress, v_m is the solid Poisson's ratio, K_m is solid bulk modulus, μ_m is solid shear modulus, and α_0 is pore aspect ratio that is closed at the confining stress σ_0.

$$\alpha_0 = \frac{2\sigma_0(1 - v_m^2)(3K_m + \mu_m)}{9K_m\mu_m} . \qquad (3.6)$$

This equation indicates a simple linear relationship between pore aspect ratio (α_0) and the confining stress (σ_0): the larger the aspect ratio of a pore, then a larger stress is required to close it. Pores with small aspect ratios are considered soft or compressible and more easily closed. Those with large aspect ratios are considered incompressible. An example of quartz mineral (K_m = 36 GPa, μ_m = 45 GPa) containing a single pore indicates that the closing stress of the pores can vary from 76 MPa with aspect ratio of 0.001 to ~75500 MPa with aspect ratio of 1. From this argument, we can obtain a lower

bound for the open pores at the depth ($\alpha \approx 0.001$) of the Haynesville Shale (about 3000 to 4000 m). If pore pressure is high, then the minimum value of α can be much smaller. The upper bound for the open shape is more difficult to obtain because nearly any pore with $\alpha > 0.001$ can be open. If multiple pores exist, this expression does not work, because when there are more pores, the rock is more compliant.

3.3.3 Model Parameters: Fluid

The fluid type in a gas shale is a combination of gas and water. The volume of each, however, can be uncertain. Calculated water saturation curves obtained from the use of conventional techniques, specifically Archie's (1942) law, yielded an average value of about 0.3 in both wells within the Haynesville. This matches published values (Hammes et al., 2011). However, we recognize that the calculated values from well logs may not be accurate because Archie's law is based on calculating saturations for clean sandstones. This issue is not part of our modeling scheme. In our work, two choices had to be made: (1) When to include the fluid, and (2) how to mix fluids.

The first choice must be made because the SCA is a high-frequency model (the pores are isolated from each other). If we believe that this accurately represents the pore space, relative to the frequency of measurement, then it is appropriate to include the fluid directly in the SCA. If the pores are connected, then the preferred operation is to model the dry-rock properties of the rock and then add the fluid afterward using Gassmann (1951) fluid substitution. Both options were explored, revealing small differences in the modeled elastic properties between the two, regardless of the pore shapes. Thus, the

42

former option was chosen, where the fluid was considered directly within the SCA. This also eliminates the requirement of knowing the exact mineral moduli for Gassmann's equation.

Options for how to mix together different fluid components were a homogeneous, fine-scale mixture of the fluid bulk moduli versus a patchy mixture (Knight and Nolen-Hoeksema, 1990). Assuming that the gas should be located in close proximity to kerogen, and that clay in different locations contains bound water, the two fluids may not be mixed homogeneously. Thus, we used a patchy mixture. The fluid used throughout the modeling was a mixture of 70% gas and 30% water. The resulting bulk modulus, using the arithmetic average, of the fluid was 0.89 GPa and density 0.5 g/cm^3. Initially, the fluid was varied in the modeling, but the results showed little sensitivity to this. Thus, variable fluid saturations are not discussed in this chapter.

3.4 MODELING RESULTS

3.4.1 Pore-Shape Analysis

The first set of modeling results corresponds to an analysis of the variable α for the pores. The SCA requires definitions of α for both the solid and pore constituents. The Haynesville Shale includes calcite, quartz, clay, kerogen and pyrite, and their percentages was assigned as 55%, 10%, 26%, 3%, and 4%, respectively. A constant value for the solids was selected at $\alpha = 0.8$. Here the aspect ratio is relatively large considering the solids are relatively stiff. The resulting density of this mixture is 2.72 g/cc, very close to that of pure calcite. This definition is important because it allows for modeling the data as

a function of only the pore shape, without considering variable composition. Moreover, this allows us to examine velocity as a function of density porosity, as calculated from equation 2.1.

Figure 3.2a is a crossplot of V_P versus ϕ_{Den} for Well A. The data from the Haynesville are the points, and the correlation between them is about –0.67. Also in the plot are five lines and a shaded region. Each line represents the modeling result for a normal distribution of the aspect ratio for the 50 pores. In each line, each point corresponds to a case that has a particular porosity composed by 50 pores with 50 aspect ratios. The uppermost line corresponds to a normal distribution of α for those 50 pores with mean 10^{-1} and standard deviation 10^{-2}. The next line down is for a distribution of mean $10^{-1.25}$ and standard deviation $10^{-2.5}$. The lowermost line corresponds to a distribution of mean 10^{-3} with standard deviation 10^{-5}. Histograms for these distributions are displayed in Figure 3.2e. These were generated numerically, so their apparent lack of smoothness is a function of the number of values drawn (50) and the number of bins (10) used to plot each. The shaded region in Figure 3.2a represents the interpolated values of those pore shapes. On any individual line, the highest velocity corresponds to the stiffest pore in the normal distribution. Thus, the decrease in velocity along a line corresponds to an increase in the porosity and to more compliant pore shapes. The model lines explain the data in that a given velocity can be related to both porosity and aspect ratio.

44
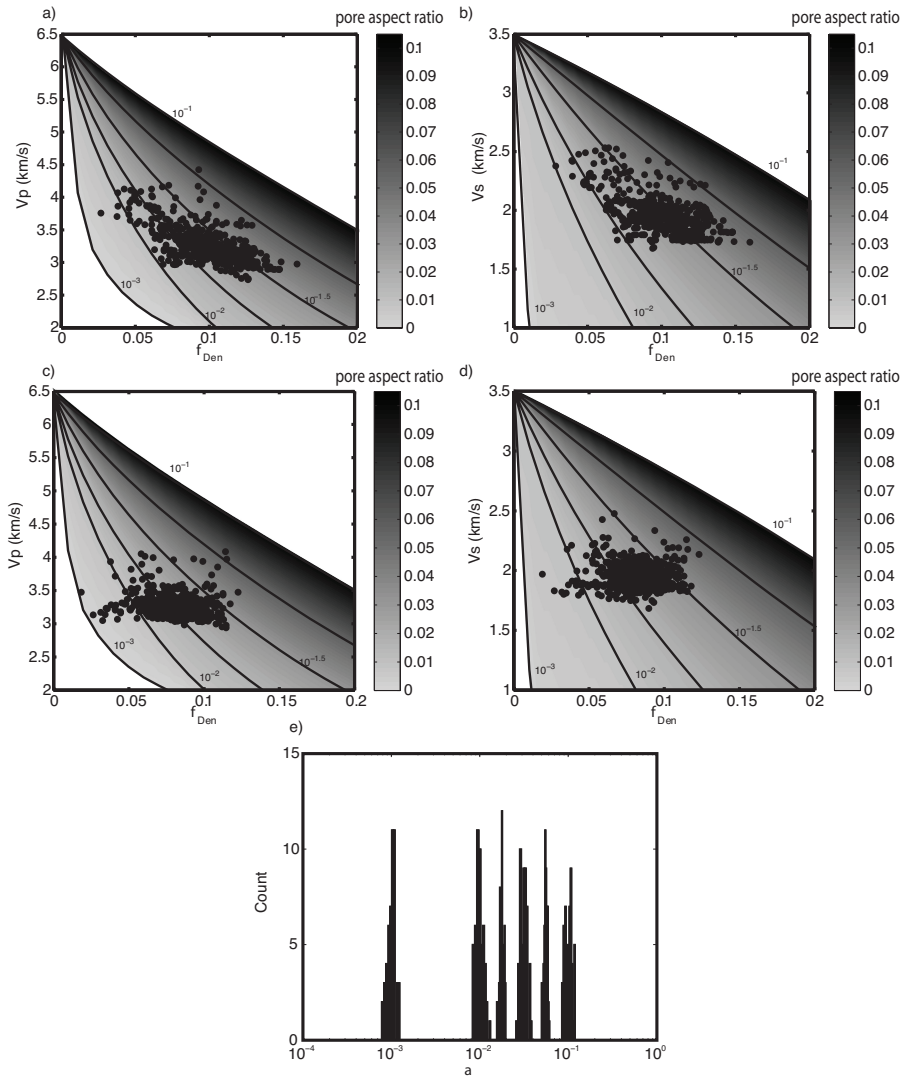
Figure 3.2: Crossplots of P- and S-wave velocity versus porosity (a and b) for Well A and (c and d) for Well B. Shading corresponds to the pore aspect ratio. Lines correspond to single composition of calcite with different aspect ratios of pores, as indicated on the plots. For each line, 50 pores were modeled, with normally distributed aspect ratios shown in (e). These six distributions were computed numerically and independently from one another. Every time they were computed, slightly different values were drawn for each, but these small variations did not alter the modeling noticeably. In (a) and (b), slightly different model lines represent the P- and S-wave velocity. These suites of models can partially explain the data in terms of pore shape, in that the range of pore shapes explains overall velocity-porosity trend. However, pore shape alone cannot explain the variability of velocity for a given value of porosity.

Figure 3.2b contains a plot of V_S as a function of ϕ_{Den}, which are slightly less correlated (at –0.62) than are V_P and ϕ_{Den}. Lines are plotted for the same distributions of α as in Figure 3.2a. In the plot of V_S, the data fall closer to models with larger aspect ratios relative to V_P, which indicates differences in aspect ratios for V_S relative to V_P. Consequently, the V_P / V_S ratio would be misrepresented, and this would occur for any composition. This difference in predictions of V_P and V_S is relatively common in effective-medium models because the modeling of the shear modulus cannot always take into account all the geometric details of shear-stress interactions between inclusions. In addition, anisotropy is an important aspect to be considered in order to model both V_P and V_S (anisotropy rock-physics modeling is done in Chapter 4). Although V_P / V_S is often used successfully as an indicator of gas saturation, the slight differences in the modeling of the V_P and V_S discouraged us from using their ratio in the analysis.

Data from Well B was analyzed in a similar way to the first, in that V_P and V_S were plotted as a function of ϕ_{Den} (Figure 3.2c and 3.2d). The crossplot (Figure 3.2c) shows little dependence of V_P on ϕ_{Den}. The same set of model lines as in Figure 3.2a with distributions of α are superimposed on the crossplot of the data. The data fall over areas of smaller aspect ratios than do the data in Figure 3.2a, for both V_P and V_S. Figure 3.2d also indicates that V_S and ϕ_{Den} are not highly correlated. Distributions of α are smaller than those seen to fit the data from Well A (Figure 3.2b). Furthermore, the distributions of aspect ratios that explain the V_P data in Figure 3.2c do not explain the V_S data. This is

similar to that observed in Figures 3.2a and 3.2b, and it is because of difficulties in modeling the shear stresses that occur among inclusions. For both wells, a combination of porosity and pore shape can explain the velocity variations, but this is for a single composition. Composition most certainly varies in both wells. However, modeling variable pore shapes for a single composition allowed us to determine a range of acceptable and useful pore aspect ratios.

3.4.2 Composition Analysis

The second set of modeling results examines the effect of variable composition. The previous results implemented a constant composition (similar to calcite) with different distributions of aspect ratios for the pores. This is now changed to analyze variable composition with a single distribution of aspect ratios for the pores. Mineral assemblages included different fractions of calcite, quartz, clay, and constant values of kerogen (3%) and pyrite (4%). Only V_P is analyzed here given the slight mismatch in the V_S modeling from Figure 3.2a. Furthermore, we are limited to dealing with a single porosity calculation, which again comes from an average of the mineral constituents.

The crossplot in Figure 3.3a is again V_P as a function of ϕ_{Den} for Well A. The color code is gamma ray, where the dark colors represent high counts and the light colors low counts. Within the Haynesville Shale, GR continuously increases with depth (Figure 2.13), which may be an indication of a lithology variation. However, a significant amount of scatter is present when the gamma ray log is used to try to discriminate the lithology. Although a clear lithology trend cannot be established, the data points with higher GR

tend to correspond to lower values of V_P between 3 and 3.5 km/s. These high GR values cut across all values of porosity. Partial explanation of the scatter present in the plot could be made from combined analysis of V_P, GR, density and depth, shown in the next three paragraphs.
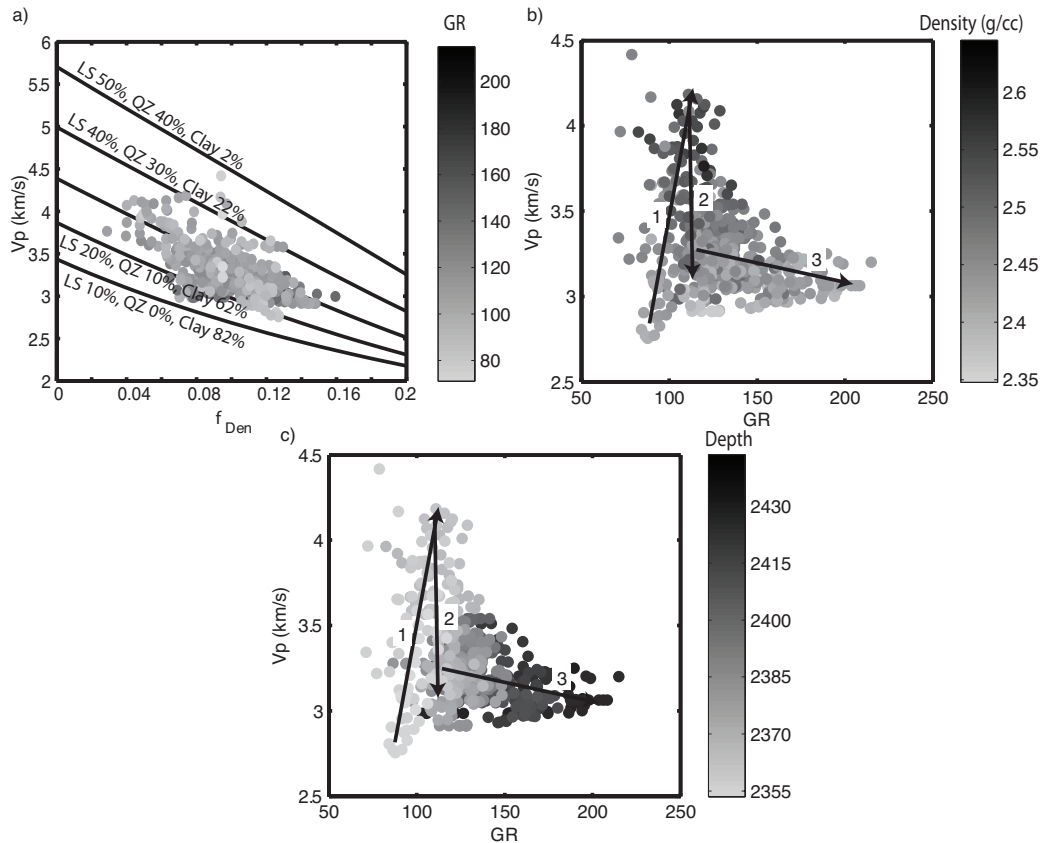
Figure 3.3: In (a) data from Well A, with P-wave velocity as a function of porosity and colored by the GR count. Five different models overlay the data, which correspond to different compositions of calcite, quartz, clay, kerogen, and pyrite. Each line also contained the same distribution of pore shapes. The GR does not provide a clear separation of the data, which suggests that composition is a factor in addition to the pore shape. In (b) crossplot of P-wave velocity as a function of GR, colored by density. This plot along with (c), where the plot is colored by depth, indicates trends observed in the well data plot in Figure 2.13. (c) Crossplot of P-wave velocity as a function of GR, colored by depth. The arrows with numbers are described in the text, indicating the variation trends of the data.

48

Also in Figure 3.3a are five model lines. They correspond to varying fractions of calcite, quartz, and clay (annotated in the figure), with constant values of kerogen (3%) and pyrite (4%). Each line was computed independently using a normal distribution of pore aspect ratios with mean of 0.095 and standard deviation of 0.01. Aspect ratios of the solids were 1 for calcite, quartz, and pyrite; 0.1 for clay; and 0.01 for kerogen. We do not know the grain shapes everywhere for every mineral. Therefore, we modeled the stiffest grains with the largest aspect ratios, and softer materials with lower aspect ratios. This set of model lines suggests that lithology could vary from calcite and quartz rich down to some combination of carbonate and high clay content. Only one realization of these models is displayed here. Slight variations in the lines can occur when a different realization of pore aspect ratios is used within the model, but these do not significantly change the values of modeled V_P. These sets of model lines follow the general trend of decreasing velocity with increasing porosity.

Additional analysis of the well data can provide at least a partial explanation of the scatter present in the plot. Figures 3.3b and 3.3c are crossplots of V_P as a function of GR colored by ρ_b and depth, respectively. The highest ρ_b values (2.6 to 2.7 g/cm^3) correspond to shallowest depths (1682 to 1697 m). From a combination of these two plots and Figure 2.13, at least two trends can be interpreted from the data. The first trend is for the shallowest part of the Haynesville where large ρ_b and V_P values occur. Density and velocity increase with depth and then decrease, as indicated by arrows 1 and 2 in the plots, but GR steadily increases. Below about 2370 m, GR continues to increase and ρ_b

shows a slight increase to 2400 m followed by a decrease from 2415 to 2446 m. The V_P, however, stays approximately constant. Arrow 3 in Figures 3.3b and 3.3c indicates this second trend. Although we are able to see these trends in the crossplots of GR versus V_P, they are not easy to interpret in Figure 3.3a.
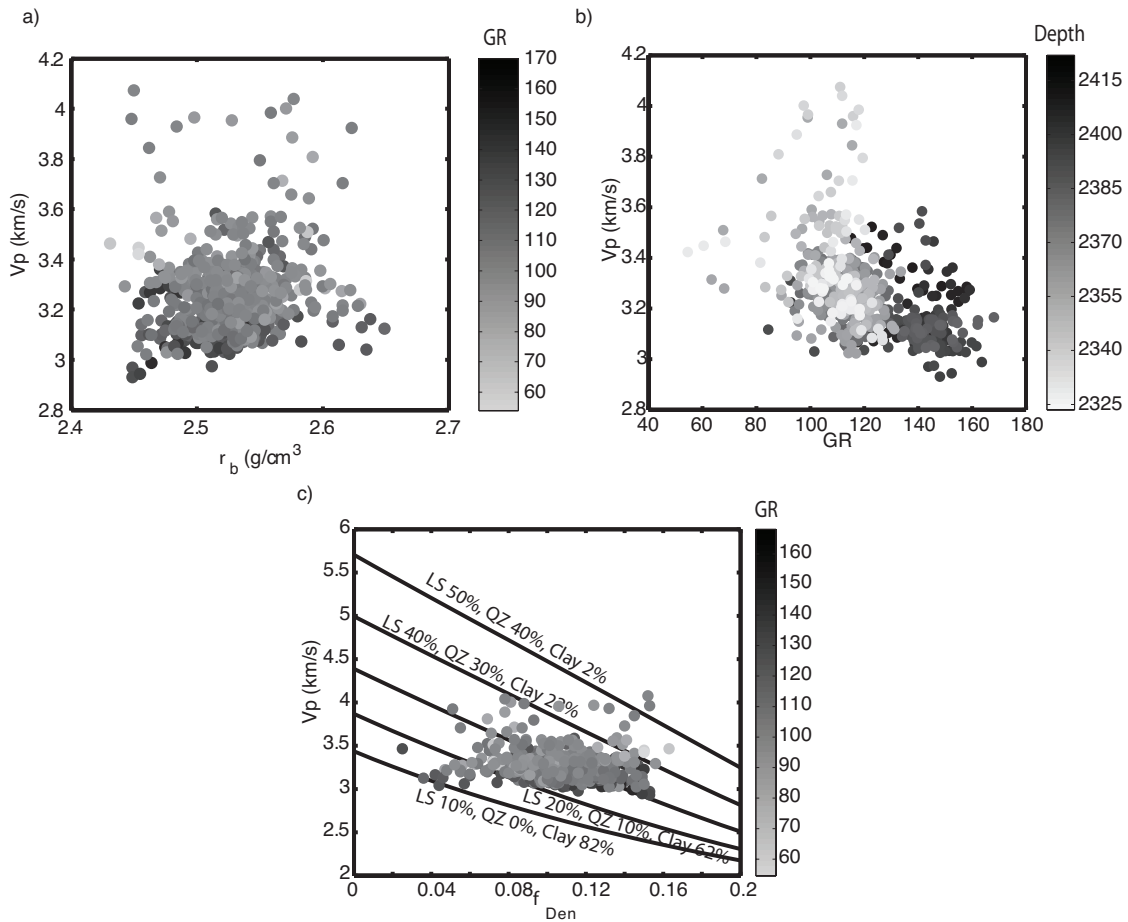
Figure 3.4: Well B. (a) Crossplot of P-wave velocity as a function of density, colored by GR. Higher GR values tend to correspond to lower velocity values. In (b), a crossplot of P-wave velocity as a function of porosity, colored by GR. Lines of constant composition cannot separate the data into different regimes. In (c) the same set of compositionally varying model lines used Figure 3.3a cannot explain the variation in the velocity as a function of porosity.

These trends reveal some depth dependence on V_P and ρ_b that may indicate compositional variation. In the shallowest part of the Haynesville, V_P and ρ_b potentially indicate a composition of carbonate and quartz. In the lower part of the Haynesville, the lower ρ_b and lower V_P indicate more clay content as part of the matrix, which is consistent with the higher GR values. These depth-dependent compositions are consistent with information from cores.

A similar investigation is performed on the data set from Well B. Figure 3.4a shows a plot of V_P as a function of ρ_b, colored by GR. Immediately noticeable is the apparent scatter in the data, where little visible correlation exists. Examination of this figure in conjunction with Figure 2.13 provides an interpretation. Within the Haynesville, ρ_b does not vary substantially, with values between 2.45 and 2.6 g/cc. The P-wave velocity gradually decreases with depth, except at the top where an increase and decrease exist. On the other hand, GR shows noticeably different behavior. A slow increase with depth occurs from about 2325 m to 2385 m. From 2385 m to the bottom of the Haynesville, the GR increases sharply and remains relatively high. This sharp increase correlates to small decreases in V_P and V_S. Accordingly, there is some correlation between V_P and GR, where the lowest V_P values correspond to the highest GR values. Figure 3.4a also illustrates this relationship, where velocity may indicate variation in the composition.

Figure 3.4b contains a plot of V_P as a function of GR colored by depth. The trends observed in Figures 3.3b and 3.3c are not present, or are less distinct than in Figures 3.4a

51

and 3.4b. Figure 3.4c is a plot V_P as a function of ϕ_{Den}, which shows nearly constant velocity for nearly all porosity values. This plot also contains the same model lines that are plotted on Figure 3.3a. However, for Figure 3.4c, the composition lines do not represent very well the decrease in GR with increasing V_P. Lines for a constant composition cut across the data that have relatively high GR values.

Comparisons of Figures 3.3, 3.4, and 3.5 suggest that both pore shape and composition play major roles in the variation of velocity. For Well A this is because of the overall trend in the porosity-velocity plane, with the ability of pore shape and composition models both to span the data. In the case of Well B, the apparent lack of correlation of velocity with porosity suggests that both composition and pore shape need to be considered jointly.

3.4.3 Joint Pore Shape and Composition Analysis

To perform this modeling, it was necessary to vary jointly distributions of pore shapes and variable composition, where both depend on the bulk density. For the pores, this involved uniform distributions of pore aspect ratios, of which 50 values comprised each distribution. Furthermore, the modeling included different bulk density values, where the bulk density changed as a function of composition.

P-wave velocity is plotted versus ρ_b and colored by GR (Figure 3.5a) for Well B. Data points are the same as for Figure 3.4a. Each subvertical, solid black line on this plot corresponds to a mineral assemblage that consists of 56% calcite, 3% kerogen, 4% pyrite, and variable quartz (35% to 10.5%) and clay content (2% to 26.5%). The set up of this

52

composition variation is an example showing the composition effect on seismic velocity. Other composition assemblages can be found in Jiang and Spikes (2011) using the self-consistent model. Porosity varies from the left to the right vertical line, and composition and pore aspect ratio vary from the bottom to top horizontal line. The solid diamonds at the end of each line corresponds to the most quartz-rich composition; triangles at the bottom refer to the most clay-rich composition. A different ρ_b corresponds to each line. Figure 3.5b, where the shading corresponds to clay content, illustrates the change in mineralogy for the different lines in 3.5a. The diamonds and triangles in 3.5b are placed identically to those in 3.5a. Although the correlation between density and V_P is not apparent, the combination of composition, pore shape, and porosity were investigated to allow us to interpret the data.

Each subvertical line in Figure 3.5a, in addition to a variable composition, also corresponds to a different set of pore shapes. Shading Figure 3.5c corresponds to the variable aspect ratios. The aspect ratios where the filled diamonds sit are all equivalent. However, the triangles are located at different values of aspect ratios. Thus, the change in V_P along any particular subvertical line in Figure 3.5a is a function of both a change in composition and a change in the pore shape. The appearances of the shaded areas in Figures 3.5b and 3.5c indicate that clay content and the pore shape are highly correlated. A clear illustration of that correlation is in Figure 3.5d, with pore aspect ratio plotted as a function of clay fraction. All the lines meet at low clay content and high aspect ratio, which corresponds to the locations of the diamonds (i.e., constant clay and constant aspect ratio).

53
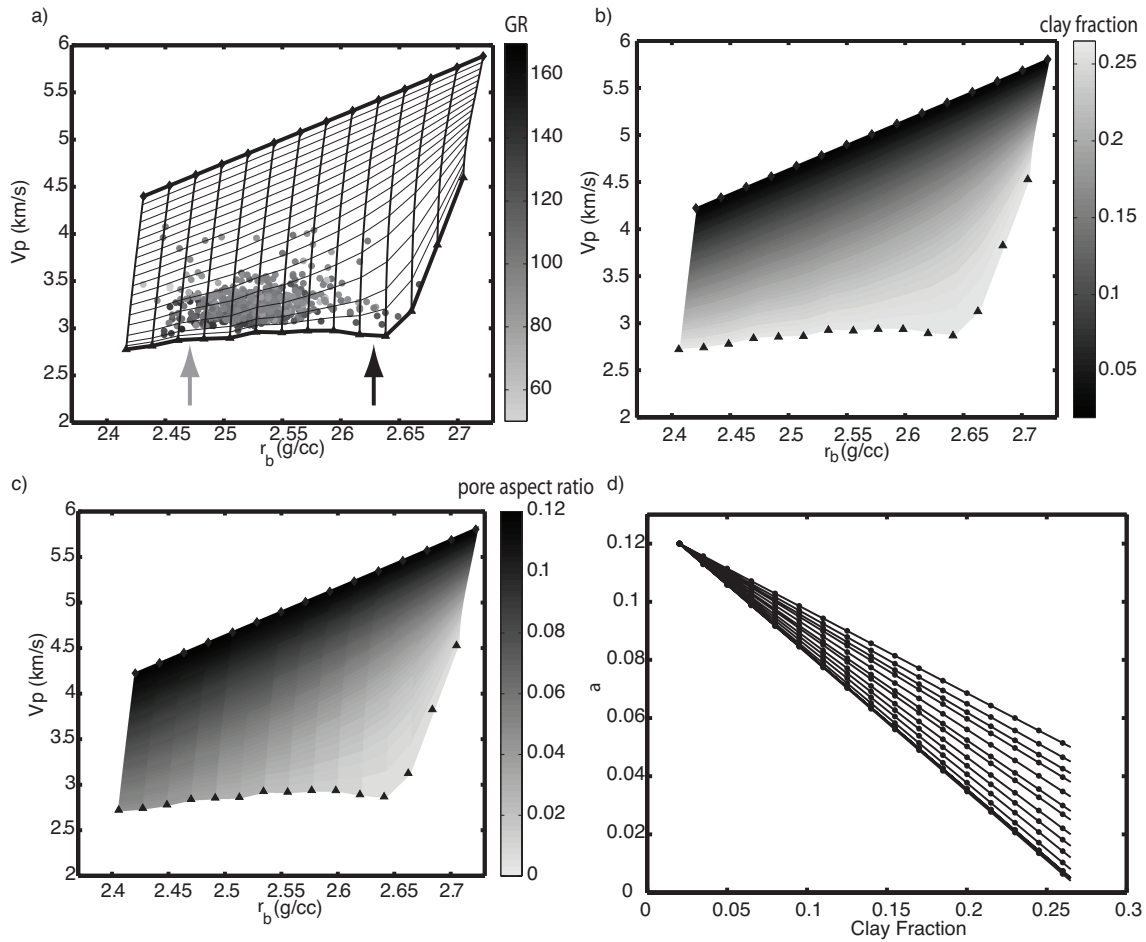
Figure 3.5: For (a) data points are the same as for Figure 3.4a. Model lines of both variable composition and variable pore shapes for a mineral assemblage of 56% calcite, 3% kerogen, 4% pyrite, and variable quartz (35% to 10.5%) and clay content (2% to 26.5%). These overlay velocity-density data, colored by GR. In (b), the range of clay content values is displayed in the shading, as is the pore aspect ratio in (c). The crossplot of aspect ratio and clay content shows the correlation between the two (d). This set of model parameters provides the ability to explain the lack of velocity variation with density, as a combination of pore shape, pore size, and composition. The black arrow indicates an area of low velocity and high density, where small pore aspect ratios are interpreted to be the dominant effect on the velocity. For low velocity and low density (gray arrow), the dominant effect on velocity is the porosity.

54

This combination of modeling parameters is able to explain the density-velocity data relatively well. More specifically, the high GR values for low velocity are represented by the clay-rich model locations, along with small pore aspect ratios. Moreover, the nearly horizontal trend between measured velocity and porosity can be explained by nearly constant composition from left to right (from Figure 3.5b), along with decreasing pore aspect ratios from left to right (from Figure 3.5c). An interpretation of pore size can then be made. For high density and low velocity, smaller pore size accompanies smaller aspect ratios (black arrow in Figure 3.5a). In this area, the dominant effect on velocity is the pore shape. On the other hand, the low-velocity and low-density area (gray arrow) can be interpreted as higher porosity that consists of larger pores with larger aspect ratios, where the dominant effect on velocity is the porosity.

Figure 3.6 is a plot for Well A, similar to Figure 3.5a. The sets of model lines are the same, and the data plotted is V_P as a function of ρ_b, colored by GR. The models extend to slightly lower density. Similar to Figure 3.5a, the low velocity data can be modeled by high clay content. The trend of increasing velocity and density can be explained by decreasing clay content. Furthermore, a secondary trend that is nearly horizontal (centered around 3 km/s) can be explained the same way that the flat velocity-density trend is interpreted in the data from Well B.

55
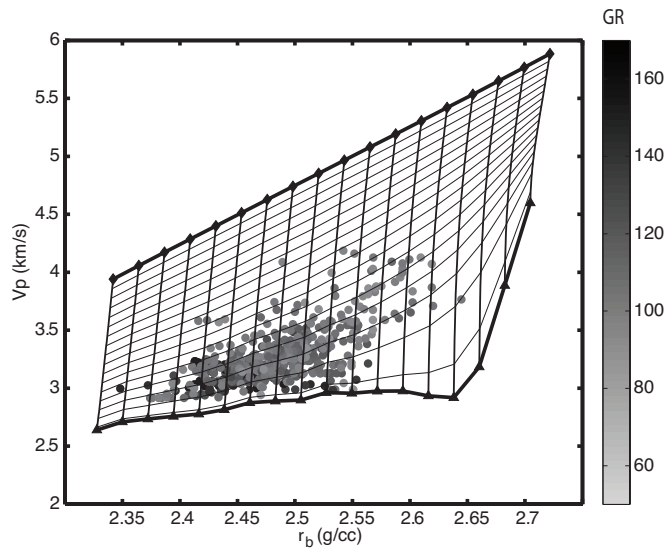
Figure 3.6: Velocity, density, and GR data from Well A, with the same set of models superimposed as for Figure 3.5. Decreasing clay content (increasing quartz) explains the trend of increasing velocity and density. Pore shape, pore size, and composition explain low velocity and high density measurements.

3.5 DISCUSSION

Various approaches to modeling the velocity data link the shale reservoir properties to velocity and density. The first approach was to analyze only the effect of the pore shapes for a constant composition. Modeling results for Well A indicated that the trend in the V_P and V_S data with ϕ_{Den} could be explained by variations in the aspect ratios of the modeled pores. These aspect ratios varied from approximately 10^{-1} to 10^{-3}. Although slightly larger aspect ratios explained the V_S data, Figure 3.2a–b provided adequate explanations of the data, but in the absence of compositional variability. The same analyses applied to the data from Well B provided similar results (Figure 3.2c–d).

Data from both wells indicated compositional variations as demonstrated by the GR logs. Velocity variations as a function of composition appear to be less

distinguishable in Well A relative to Well B. For Well A, when V_P is plotted versus ϕ_{Den} and colored by GR (Figure 3.3a), significant scatter is present, and the GR values do not successfully separate the data. For Well B, Figure 3.4a shows that the V_P increases as GR deceases although scatter is present in the crossplot. Attempting to explain this variation in velocity by changing only composition, as in Figure 3.4b, provides a partial explanation of the data. Furthermore, Figure 3.4c illustrated that composition models with constant aspect ratios misrepresented the apparent composition trend in the data. This was motivation to vary jointly pore shapes and composition. Those modeling results (Figures 3.5 and 3.6) demonstrated that different mineral assemblages, coupled with variable pore shapes, provide a way to interpret the data in terms of pore size, pore shape, porosity, and composition. More specifically, low velocity can be linked to softer composition (clay and kerogen), but with potentially a wide range of pore shapes. The larger the aspect ratio of the pore, the longer that pore will be open, because round pores are stiffer than flattened pores. Furthermore, high velocity and high density combinations could correspond to zones suitable for inducing hydraulic fracturing.

In addition to the self-consistent model, I also used the differential effective medium (DEM) model to calibrate the relationships between reservoir and elastic properties for the Haynesville Shale. The DEM modeling results were quite similar to the self-consistent modeling results. The details can be seen in Appendix B.

In this chapter, the porosity was calculated from the density log assuming a single limestone matrix. More accurately, in the rest of this dissertation, the porosity was calculated from the density log using an interpolated composition based on the core

analysis and XRD results. The updated density porosity was lower than the older one, and was closer to the average porosity observed for the Haynesville Shale (Wang and Hammes, 2010).

Using the self-consistent model, we built up two workflows to estimate porosity and pore shape separately (Jiang and Spikes, 2012, Appendix C). In the workflows, the composition was assumed to have the average percentages of different minerals from core analysis and XRD results: 37% clay, 33% quartz, 14% limestone, 8% plagioclase, 5% kerogen, 2% pyrite, 0.8% dolomite, and 0.2% feldspar. Based on P-impedance, the workflows provided good estimates of porosity given the pore shape distribution, as well as estimation of pore shape distribution given density porosities. However, the self-consistent model was not able to model P- and S-wave velocities or impedances simultaneously (Figure 3.7), although most of the data points were modeled as shown in the crossplots of P-impedance vesurs porosity (Figure C.6a) and S-impedance versus porosity (Figure C.7). This is mainly because the self-consistent model itself did not account for the anisotropy. In the following chapters, anisotropy was included to build a more complete rock-physics model for the Haynesville Shale.

3.6 CONCLUSION

This work shows how the P-wave velocities (and to a limited extent S-waves) in the Haynesville Shale can be modeled using an effective-medium model. The goal was to explain trends in the measured velocities in two wells by modeling isotropic distributions of variable composition, grain shapes, and pore shapes. Results of the modeling indicated

that the self-consistent approximation is one model that could be used for this purpose. Importantly, joint variations of composition and pore shape provided the best explanations of the elastic properties in terms of the rock properties. The procedure and results from this investigation could be applied at the seismic scale. Well data combined with core information would provide the calibration of a seismic-inversion routine or guide calculations of seismic attributes. The composition variation could be extended to quartz, calcite, clay and kerogen (Chapter 4). Then, the intent would be to identify and characterize locations of high organic matter in the Haynesville Shale (likely lower velocity) that might be more productive, as well as to identify more brittle zones (higher velocity) where fractures could be kept open for longer durations.
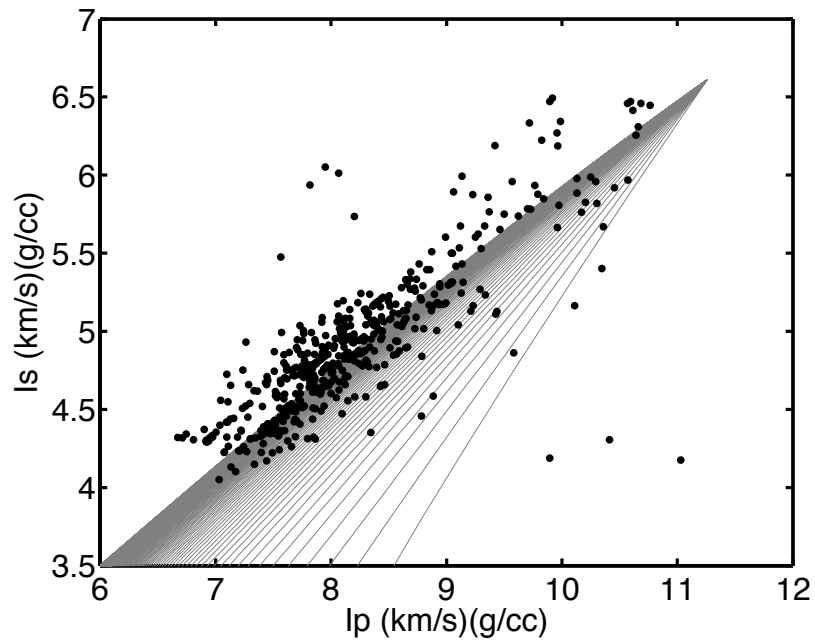
Figure 3.7: Crossplot of S-impedance versus P-impedance (Well A). A lot of the data points (black dots) were not covered by the modeling lines with different pore shapes (gray lines). This indicates that the self-consistent model was not able to model both P- and S-impedances simultaneously. For the gray lines, the pore aspect ratio increases from lower right to upper left.

Chapter 4: Estimation of reservoir properties of the Haynesville Shale by using rock-physics modeling and grid searching

4.1 ABSTRACT

This chapter presents a workflow that combines an isotropic and an anisotropic effective medium model with a grid-search method to invert for the reservoir properties (porosity, composition, and pore shape) of the Haynesville Shale. The reservoir properties inverted from this workflow closely matched the observed data, and they provide very useful information in determining locations with relatively high porosities and relatively large fractions of brittle components favorable for hydraulic fracturing. The isotropic effective medium model represents a complex medium as a single homogeneous medium by including grains and pores of different shapes and sizes. The anisotropic effective medium model introduces vertical transversely isotropic media through aligned fractures. After building the relationships between the reservoir properties and P- and S-wave velocities, we used grid searching to obtain porosity, composition and pore shape distributions conditioned by the rock-physics models. The modeled seismic velocities that satisfied criteria from objective functions provided estimated reservoir properties. The porosity and composition estimations at the well location matched the observations from log and core data quite well. The pore shape estimation suggested that the pores, cracks, and fractures within the Haynesville Shale have elongated shapes. Future

application of this workflow at the seismic scale will provide continuous spatial distributions of these reservoir properties.

4.2 INTRODUCTION

Estimation of reservoir properties, such as porosity, composition, and pore shape of gas shales and other unconventional hydrocarbon systems is important for both exploration and production. Understanding these reservoir properties contributes to identifying zones of economic production and possible optimal zones for hydraulic fracturing. Porosity estimation helps to determine gas capacity and the estimated ultimate recovery (EUR); composition contributes to understand shale brittleness, and pore aspect ratio provides additional information to determine the stiffness of the shale.

To understand reservoir properties of shales, rock-physics models are very important. Rock-physics models describe the relationships between reservoir properties and the elastic properties, calibrated by well log and core data at well locations. The specific rock-physics model to be used depends on the rock type and complexity of the rock. The complexity of gas shales results from relationships between lithology, porosity, fluid, pore shape, pressure and anisotropy. Although numerous contact-theory models (Dvorkin and Nur, 1996; Gal et al., 1998; Avseth et al., 2000), empirical rock-physics relationships (Tosaya and Nur, 1982; Castagna et al., 1985) and inclusion-based models (Kuster and Toksoz, 1974; O'Connell and Budiansky, 1974) exist, few of them are capable of modeling complex shales in terms of pore and grain shapes, composition, and anisotropy. The Haynesville Shale tends to have flattened or elongated grains and pores

(Curtis et al., 2010). These flattened or elongated grains and pores significantly reduce the propagating velocities in the shale, because pores of such shape are compliant, which reduce the rock moduli, depending on the orientation of pores relative to wave propagation and/or polarization directions. In addition, shales are typically anisotropic due to intrinsic alignment of clay platelets and/or alignment of pores, cracks or fractures. Therefore, to model and understand gas shales, we must utilize more complicated models.

Unlike conventional clastic reservoirs, for which distributions of porosity, clay content, water saturation, lithology facies and fluid types from seismic data were estimated in numerous studies (e.g., Mukerji et al., 2001; Eidsvik et al., 2004; Bachrach, 2006; Spikes et al., 2007; Grana and Della Rossa, 2010; Rimstad et al., 2012), characterizing reservoir properties of gas shales is still a young and very active area of research. Vanorio et al. (2008) used vitrinite reflectance data to generate relationships between maturity and Thomsen's (1986) anisotropic parameter ε to understand how maturation processes cause anisotropy changes. Delle Piane et al. (2011) investigated the intrinsic and crack-induced anisotropy of brine-saturated shale samples under different external stresses. They found that elastic anisotropy of these samples depended on the composition and spatial distributions of different minerals and microfractures, and the change of anisotropy depended on the applied stresses, their orientations and the degree of stress anisotropy. Nadri et al. (2012) presented an approach to estimate the anisotropy parameters of transversely isotropic shales of arbitrary geometry. They successfully applied this approach to ultrasonic P-wave velocity data from a spherical shale sample

63

and a cylindrical shale sample. In addition to experimental investigations, modeling studies of the elastic properties of shales have been presented. Dræge et al. (2006) combined the self-consistent model and a differential effective medium model with a shale compaction theory to model the effective elastic stiffness of shales as a function of depth, as well as estimating the effect of cementation on the effective elastic stiffness of shales. Their results were consistent with the vertical P- and S-wave velocities from three wells. Avseth et al. (2008) used rock physics and AVO depth trend modeling to understand the physical properties (intrinsic anisotropy, smectite-to-illite transition, AVO attributes) of mechanically compacted shales as function of burial depth, and, therefore, improved characterization of sandstone reservoirs embedded in shales. Ciz and Shapiro (2009) were able to explain the compliance tensor, anellipticity, and three anisotropic parameters under different stresses for transversely isotropic shales through a porosity-deformation approach and its anisotropic extension. Pervukhina et al. (2011) described the five stress-dependent elastic coefficients of transversely isotropic shales using a model that treated the orientation of clay platelets and compliance ratio of the platelet contacts as inputs. Their model was able to predict simultaneously the stress dependency of all five elastic compliances. Recently, Jiang and Spikes (2012) used the self-consistent model and a grid search method to estimate porosity and pore shape distributions for the Haynesville Shale. In that study, only P-impedance was included to estimate either porosity or pore shape under isotropic conditions, and anisotropy was not considered.

The objective of this chapter is to provide a comprehensive understanding of the porosity, composition, and pore shape distributions of the Haynesville Shale constrained

by both P- and S-wave velocities through a combination of rock-physics models and grid searching. We combined an isotropic effective medium model (the self-consistent model, O'Connell and Budiansky, 1974; Berryman, 1980) with an anisotropic effective medium model (Chapman, 2003). The self-consistent model provided a porous rock matrix with multiple mineral phases and pores with different aspect ratios. The anisotropic effective medium model based on Chapman (2003) provided frequency- and pore-pressure-dependent anisotropy. Relationships between reservoir properties and elastic properties were obtained by correlating input rock property distributions and combining these two models. Based on these relationships, the grid search provided distributions of porosity, composition, and pore shapes by considering all the possible modeled solutions without bias.

4.3 DATA

In this chapter, well log data from Well B (Figure 2.13) and core data from Well A (Figure 2.14) were used. The two wells show very similar features in the logs (Figure 2.12 and 2.13), and it is valid to apply the core data from Well A to Well B. The porosity was calculated from

$$\phi = \frac{\rho_m - \rho_b}{\rho_m - \rho_{fl}} \qquad (4.1)$$

as a function of measured density log (ρ_b), density of the rock matrix (ρ_m), and density of the pore fluid (ρ_{fl}), assuming the rock matrix as a combination of different minerals from core analysis and XRD results. To simplify the modeling to an extent, we included only

65

quartz, calcite, pyrite, kerogen and clay in the rock-physics models. We transferred the percentages of feldspar (potassium feldspar), plagioclase (calcium feldspar), and dolomite from the core analysis and XRD measurement to calcite. Then the average percentages of quartz, calcite, pyrite, kerogen, and clay are about 31.6%, 25.8%, 2%, 5.3%, and 35.3% for Well A, respectively. Fluid density was calculated from a brine and gas mixture with an average water saturation of approximately 25% based on the resistivity log.

4.4 METHOD

This chapter combines both forward and inverse calculations to estimate simultaneously the distributions of porosity, composition and pore shape for the Haynesville Shale. This section emphasizes the rock-physics modeling and inversion reasoning. The following section provides the parameter values used in each step of the modeling. The forward calculation is rock-physics modeling that provides relationships between the reservoir properties and elastic properties, calibrated to P- and S-wave velocity measurements. The inverse calculation of rock properties is done through grid searching, which provides probabilistic estimates of reservoir properties conditioned by the relationships between reservoir properties and elastic properties from the rock-physics modeling. The grid searching provides a range of reservoir property estimations, and help to understand the uncertainty of results due to the uncertainty of log measurements.

For vertically transversely isotropic (VTI) media, such as the Haynesville Shale (Horne et al., 2012), five independent stiffness tensor components are required in the

Voigt notation (Thomsen, 1986): C_{11}, C_{33}, C_{44}, C_{66}, and C_{13}. Velocities propagating along

and perpendicular to the axis of symmetry, and at angles in between, depend on these five

components and the bulk density. The P- and S-wave velocities (V_P and V_S) perpendicular

to the fractures (Thomsen, 1986) were calculated using

$$V_P = \sqrt{\frac{C_{33}}{\rho}}$$
$$V_S = \sqrt{\frac{C_{44}}{\rho}} . \qquad (4.2)$$

We used Chapman's (2003) model to calculate the five components based on the rock

matrix that contain multiple mineral and pore phases (equations D1–D5). The rock matrix

was built from the self-consistent model (O'Connell and Budiansky, 1974; Berryman,

1980).

Chapman's model (Chapman, 2001; Chapman et al., 2002; Chapman, 2003) was

introduced to account for squirt flow in the computation of effective moduli of either

isotropic or anisotropic rocks. Squirt flow is the fluid interaction caused by the pressure

gradient at the micro-scale during wave propagation when the wavelength is smaller than

the pore size (Dvorkin and Nur, 1993; Dvorkin et al., 1994). The localized fluid flow

usually follows directions different from the direction of wave propagation. The model

(Chapman, 2003) imposes anisotropy from one set of aligned fractures. As an extension,

Chapman (2009) developed a technique to include two fracture sets with different scale

lengths and orientations. Because the Haynesville Shale was treated as a VTI medium

with only one axis of symmetry, we implemented the model from Chapman (2003) in this

chapter. Compared to other transversely isotropic models (Hornby et al., 1994; Dræge et

al., 2006; Ciz and Shapiro, 2009; Kuila et al., 2011; Pervukhina et al., 2011; Nadri et al., 2012), this model considers frequency and pore pressure effects, and it is consistent with both Gassmann's theorem and Biot's prediction of a slow compressional wave (Chapman, 2001). In addition, most parameters in the model can be directly measured or estimated from measurements, and they all correspond to well defined rock properties and have physical interpretations.

In Chapman's model, the rock contains spherical pores, randomly aligned cracks, and aligned fractures that generate anisotropy. Cracks and fractures both have idealized ellipsoidal shapes, and they have the same aspect ratio that is defined as the ratio between the smallest axis and largest axis. Then the crack porosity (ϕ_c) and fracture porosity (ϕ_f) can be calculated based on their aspect ratios and crack density (ε_c) and fracture density (ε_f):

$$\phi_c = \frac{4\pi\alpha}{3}\varepsilon_c$$
$$\phi_f = \frac{4\pi\alpha}{3}\varepsilon_f \qquad (4.3)$$

The total porosity in Chapman's model can be expressed as the summation of round pore porosity (ϕ_{rp}), crack porosity and fracture porosity, i.e.,

$$\phi_{chap} = \phi_{rp} + \phi_c + \phi_f . \qquad (4.4)$$

Because pores in Haynesville Shale are unlikely to be spherical, the contribution from round pores ϕ_{rp} should be very small. Elongated pores will be introduced in the next part of the modeling.

The spherical pores and cracks are assumed to have the same radius as the grain size (ς). The radius of fracture (a_f) can be either larger or the same as grain size. In this chapter, we estimated the grain and fracture sizes of the Haynesville Shale from microstructure images (Curtis et al., 2010). Both grain and fracture sizes are about 1 μm on average. Therefore, the fractures in this case are similar to microcracks in terms of size, and they are aligned along the bedding direction. The sizes of spherical pores, cracks, and fractures affect the characteristic frequency of the squirt flow, attenuation and velocity dispersion. The relaxation-time terms for a crack (τ_m) and a fracture (τ_f) that define the 'microstructural' squirt-flow frequency are linearly related to the viscosity of the pore fluid, and their ratios are the same as the ratio between the grain size and fracture size

$$\frac{\tau_m}{\tau_f} = \frac{\varsigma}{a_f}.$$ (4.5)

In Chapman (2003), τ_m for water-saturated sandstone was 20 μs. Because the pore fluid in the Haynesville Shale contains a mixture of water and gas, whose viscosity is less than that of pure water, we used 2 μs for τ_m. Correspondingly, the relaxation-time term for a fracture is the same as the one for a crack, and their characteristic frequencies are also identical (Table 4.1). The five stiffness components are calculated from equation D1 to D5.

Table 4.1. Parameters used in Chapman's model

Parameter	Symbol	Value	Unit
Round Pore Porosity	ϕ_{rp}	0.001	Fraction
Fracture Density	ε_f	0.04	Fraction
Crack Density	ε	0.01	Fraction
Relaxation-Time Term for Cracks	τ_m	2.00×10^{-6}	s
Relaxation-Time Term for Fractures	τ_f	2.00×10^{-6}	s
Grain Size	ς	1.00×10^{-6}	m
Fracture Size	a_f	1.00×10^{-6}	m

Some limitations arise when applying Chapman's model to the Haynesville Shale. For example, the model assumes that the anisotropy only comes from aligned fractures, whereas aligned clay minerals likely contribute to the VTI anisotropy. Also, Chapman's model contains only one solid phase, and it assumes the pores are spherical, whereas the Haynesville Shale contains multiple minerals phases. Furthermore, its pores are primarily non-spherical based on microstructure images (Curtis et al., 2010).

To address the above limitations, we combined an additional model, the self-consistent model (O'Connell and Budiansky, 1974; Berryman, 1980), with Chapman's model to account for multiple mineral phases and non-spherical pores (Figure 4.1). The self-consistent model is not limited to specific compositions, and it is able to incorporate multiple mineralogical and pore phases, as well as their shapes and spatial distributions. The details of the self-consistent model are described in Chapter 3 (only the self-consistent model was applied in Chapter 3).
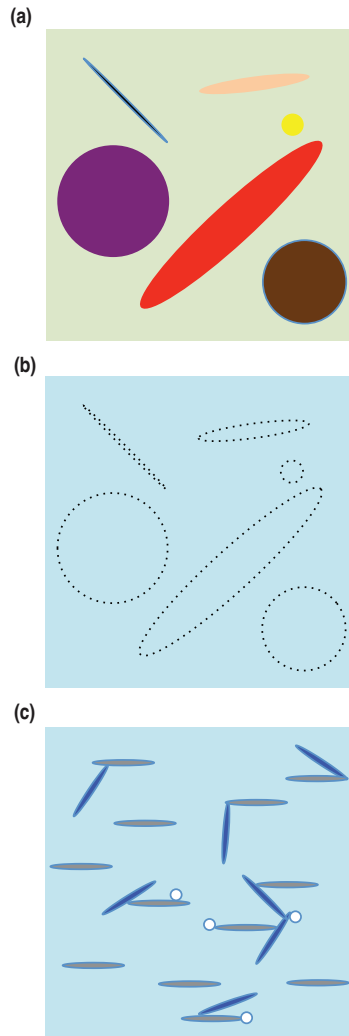
Figure 4.1: Schematics that illustrate the rock-physics models. (a) The self-consistent model. In the background matrix (green square), there are inclusions of quartz (purple), calcite (brown), pyrite (yellow), kerogen (black), clay (red) and non-spherical pore (orange). These inclusions have different fractions and shapes. The inclusion sizes in the self-consistent model are not specified, and their relative fractions and shapes affect the effective moduli of the rock. (b) The homogeneous rock matrix that is built by the self-consistent model, with different mineral and non-spherical pore inclusions. (c) Chapman's model. In the rock matrix that is built by the self-consistent model (light blue square), there are randomly distributed round pores (white), randomly distributed and oriented microcracks (dark blue), and aligned fractures (gray). Cracks and fractures have the same aspect ratio as the non-spherical pores in the self-consistent model, and cracks and fractures have the same size. Anisotropy comes from the aligned fractures.

The self-consistent model and Chapman's model have their own pore systems, and these two pore systems are not connected. In other words, this is a dual porosity representation. The self-consistent model builds an isotropic porous rock matrix that contains multiple mineral phases and non-spheric pores, and the porous rock matrix is then treated as the background rock matrix in the Chapman's model. The self-consistent model contains non-spherical pores that are isolated, while Chapman's model contains spherical pores, cracks and fractures that are connected to each other. Fractures are not connected to other fractures, and every crack and spherical pore connects to at most only one fracture (Chapman, 2003).

In the self-consistent model, the inclusion sizes are not defined because the major factor that affects the velocities are the pore shape and concentration. In Chapman's model, the spherical pores, cracks and fractures all have the same scale as grain sizes, assumed to be 1 μm. The fracture size affects the squirt flow effect, with larger fracture sizes having lower characteristic frequencies and smaller fracture sizes having higher characteristic frequencies of the squirt flow.

The combination of Chapman's model and the self-consistent model provided relationships between elastic and reservoir properties for the Haynesville Shale. After that, a grid search method (Sen and Stoffa, 1995) was used to invert the reservoir properties from the elastic properties. The reservoir properties were obtained by systematically searching the model space that is composed of elastic properties. Specifically, the model space was represented by a large number of points on a uniform

grid. The computational cost is not expensive due to the relatively simple objective functions for V_P and V_S:

$$Obj\_P = |V_{Pmodel} - V_{Pobserved}|, \qquad (4.6)$$

$$Obj\_S = |V_{Smodel} - V_{Sobserved}|. \qquad (4.7)$$

The modeled P- and S-wave velocities are expressed as V_{Pmodel} and V_{Smodel}, and the observed P- and S-wave velocities are expressed as $V_{Pobserved}$ and $V_{Sobserved}$. The modeled velocity values that provided the minima of the objective functions corresponded to the best solutions of the reservoir properties. In this chapter, three reservoir properties (pore aspect ratio, porosity, and composition) were jointly inverted from two elastic properties (V_P and V_S). Therefore, correlations among the prior distributions of these three reservoir properties were introduced when generating V_P and V_S from the rock-physics models. Those correlations are described in the next section. The most likely solutions and probability distributions at each depth point were obtained. The advantage of the grid search method is that the range of values for the model space can be specified, and all the possible solutions are equally considered without any bias. The disadvantage of the grid search method is that it can be time consuming and computationally expensive, depending on the number of points in the model space. The computational cost increases exponentially each time one more property is added (LaValle et al., 2004). In addition, the range of values for the model space should be carefully selected in order to include all physically reasonable possibilities.

4.5 WORKFLOW

Given the prior distributions of the reservoir properties (composition, porosity, and pore shape), the combination of the self-consistent model and Chapman's model provided V_P and V_S. The prior distributions of these reservoir properties were assumed to contain all possible cases within the defined range. Each group of reservoir properties corresponded to a set of modeled V_P and V_S that were calculated from a set of reservoir properties. Therefore, the sets of modeled V_P and V_S that met the criteria from the objective functions provided the sets of reservoir properties as estimations.

In the workflow, we first assumed the prior composition distribution contained 400 mineral assemblages with different percentages of quartz, calcite, pyrite, kerogen, and clay (Figure 4.2a). This number (400) is enough to maintain high accuracy but low computational cost. In each case, percentages of quartz, calcite, kerogen and clay were varied. Pyrite was fixed as 2%. From the composition assemblages 1 to 400, percentages for quartz and calcite decreased, and percentages for kerogen and clay increased, so the stiffness of the rock matrix decreased as the case number increases. Because the self-consistent model requires aspect ratios for both mineral and pore phases, we assumed the aspect ratios were 1 for stiff quartz, calcite and pyrite, 0.1 for clay, and 0.01 for kerogen. Pore aspect ratio was defined later, based on the prior composition and porosity.

The total porosity in the workflow was defined as a function of four different porosity types. Those four included the non-spherical pore porosity in the self-consistent model (SCM porosity) and spherical pores, cracks, and fractures in the Chapman's model. Prior SCM porosity (ϕ_{scm}) was uniformly distributed between 0 and 0.4, with an

74

increment of 0.01, for each of the 400 composition assemblages. This large porosity range assured that all the likely porosity values were included in the model. Because there are three properties to be inverted from two known variables (V_P and V_S), correlations among the three reservoir properties need to be assumed. We linearly correlated the prior aspect ratio (α) with the prior composition assemblage (N_{comp}) and prior SCM porosity using the relationship

$$\alpha = \frac{(N_{total} - N_{comp} + 1) \times C_f}{N_{total}} \times (\max(\phi_{scm}) - \phi_{scm}). \qquad (4.8)$$

In equation 4.8, N_{total} is 400, the total number of composition assemblages, N_{comp} is the composition number index, ϕ_{scm} is the prior SCM porosity, and C_f is a coefficient that determines the aspect ratio value for each prior composition and SCM porosity. The composition assemblage is in specific order, with increasing stiffness from high case number to low case number. The value of 0.3 was used to generate a suitable aspect ratio range. The aspect ratio was positively related to the rock matrix stiffness and negatively related to the SCM porosity (Figure 4.2b). As the clay percentage increased, the pore aspect ratio decreased; as SCM porosity increased, the pore aspect ratio decreased. The aspect ratio decreases from 0.12 for the stiffest rock matrix with smallest SCM porosity to nearly 0 for softest rock matrix with largest SCM porosity. Based on the prior distributions of composition, SCM porosity and pore aspect ratio, a porous rock matrix (Figure 4.1b) was generated from the self-consistent model.
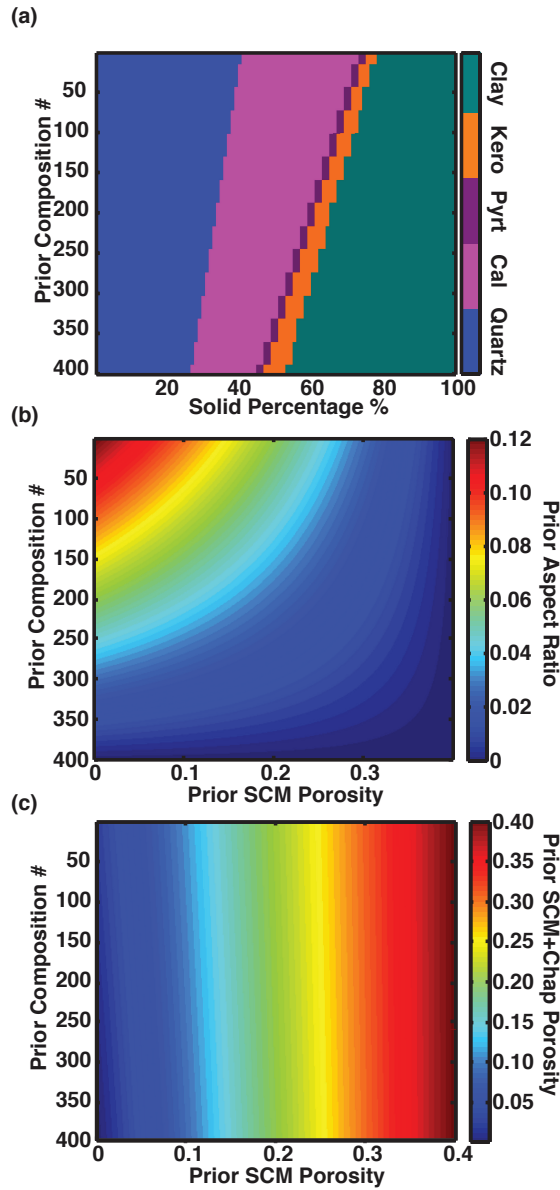
Figure 4.2: (a) The 400 prior composition assemblages used in the modeling. In each case, percentages of quartz, calcite, kerogen and clay were changed. The percentage of pyrite was fixed as 2%. (b) The prior aspect ratio distribution based on both prior composition and porosity distribution. To solve three unknowns based on two knowns, the prior aspect ratio was correlated with the prior composition and prior SCM porosity based on equation 4.8. (c) The total prior porosity distribution. It contains porosity for SCM and Chapman's model. The porosity from Chapman's model varies with aspect ratio. Therefore, the prior total porosity distribution is not a simple uniform distribution between 0 and 0.4.

The total porosity (ϕ_{total}) depended on the porosities from both the Chapman's model (equation 4.4) and the self-consistent model. It was calculated from the solid fraction in the self-consistent model ($1-\phi_{scm}$) and solid fraction in Chapman's model ($1-\phi_{chap}$) using

$$\phi_{total} = 1 - (1 - \phi_{scm}) \times (1 - \phi_{chap}). \qquad (4.9)$$

The porosity in Chapman's model ϕ_{chap} is calculated from equation 4.4. This total porosity was correlated with the prior composition and the prior SCM porosity (Figure 4.2c).

In the rock-physics modeling, squirt flow was considered to be related with the porosities in Chapman's model, and the SCM porosities do not contribute to squirt flow. We computed the velocity dispersion behaviors for a model that contains compositions similar to measured results from Well A and with total porosity of 5% that is close to the average porosity of the Haynesville Shale (Figure 4.3). The curves show that the velocities, especially P-wave velocity, show dispersive behavior at about 10 kHz. Because the relaxation-time term for cracks and fractures are the same, they have the same characteristic frequency. In the modeling, we set the frequency as 10 kHz, which is also near the frequency of the log data.

From the combination of the self-consistent model and Chapman's model, we obtained modeled V_P and V_S values for each set of composition, porosity, and aspect ratio. The modeled V_P and V_S were compared with observed V_P and V_S from the log data (equations 4.6 and 4.7). If the differences between the modeled and observed V_P and V_S were less than 0.08 km/s (~2% error for V_P and ~4% error for V_S), then the corresponding

77

set of reservoir properties (pore aspect ratio, porosity, and composition) were accepted. In this work, we not only obtained the best solutions, but also probability distributions of multiple solutions. The procedure was repeated at each depth in the log data to obtain the distributions of porosity, composition and pore aspect ratio.
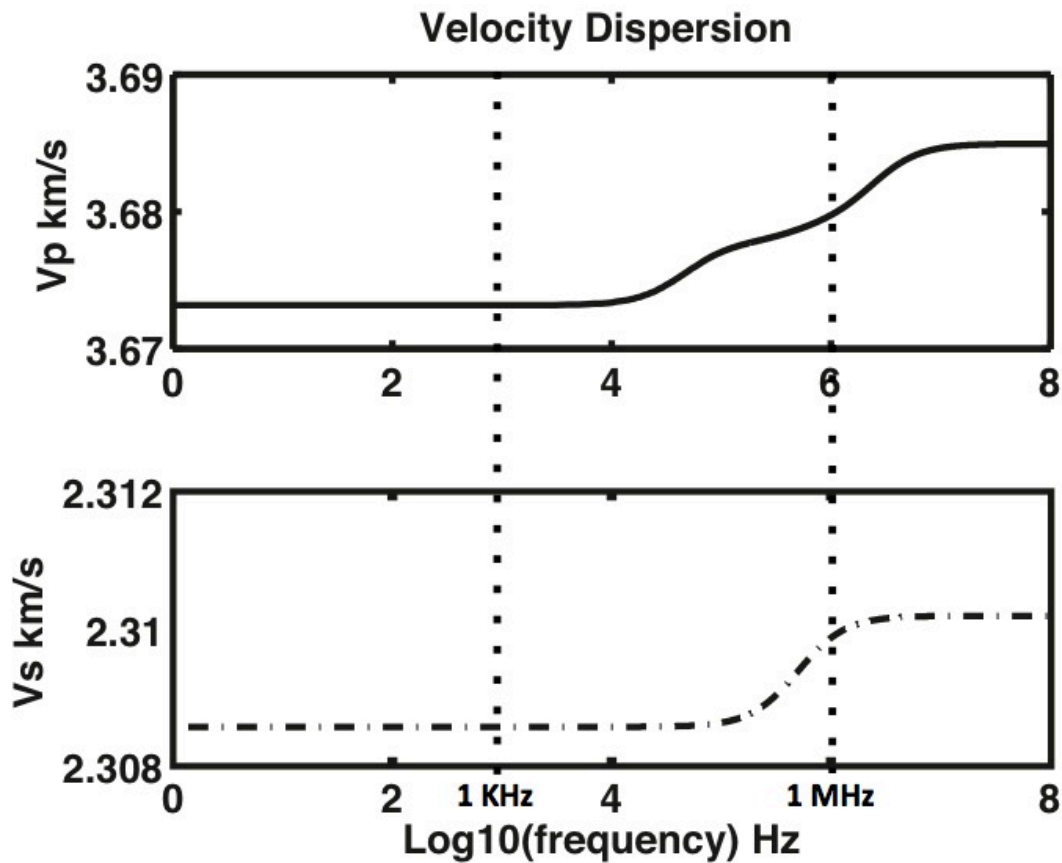
Figure 4.3: Velocity dispersion curves for V_P and V_S. Although both the self-consistent model and Chapman's model were applied, the dispersion only came from Chapman's model. In the model, the composition includes quartz, calcite, kerogen and clay with percentages similar to measured results for Well A. The total porosity was set as 5%, which is close to the average values of the Haynesville Shale. The dotted verticle lines marks the typical log frequency level (1 KHz) and typical lab frequency level (1 MHz).

4.6 ELASTIC PROPERTIES OF CLAY, KEROGEN AND FLUID

The shale model we built contained quartz, calcite, pyrite, kerogen, clay, and pores/cracks/fractures with brine and gas saturation. Elastic properties for quartz, calcite and pyrite are very well known, and they have small uncertainties. However, the properties for clay, fluid, and kerogen are ambiguous and have large uncertainties. We investigated how different clay and fluid property values affected the modeling results.

It is difficult to measure the elastic properties of clay because clay mineral grains are very small, and they tend to have chemical reactions with organic polar molecules (Theng, 1974; Wang et al., 2001; Vanorio et al., 2003; Moyano et al., 2012). Different types of clay, such as smectite, chlorite and kaolinite, have different bulk and shear moduli and densities due to different mineralogy, structure, and ability to hold clay-bound water. For example, smectite absorbs much more water in volume than illite (Whitney, 1990; Saffer and Marone, 2003), and it has much lower bulk and shear modulus than illite and other clays as a result (Wang et al., 2001). From extrapolation of empirical dependences to pure clay, Castagna et al. (1985), Tosaya and Nur (1982) and Han et al. (1986) obtained similar elastic properties with each other. Wang et al. (2001) obtained much higher bulk and shear moduli through measurements on clay epoxy artificial samples. Vanorio et al. (2003) obtained very low bulk and shear moduli of clay as functions of pressure and saturation through independent experimental methods. By using a generalized singular approximation method of effective media theory, Bayuk et al. (2007) were able to invert a stiffness tensor of clay and obtain its anisotropy parameters. Overall, the elastic properties of various clay minerals have large

uncertainties, with the bulk modulus variations from less than 10 GPa to greater than 60 GPa.

To investigate the effects of varying clay properties on the modeling, we tested the combined model using bulk modulus of clay from 10 GPa to 60 GPa. The shear modulus of clay was set as 0.47 times the bulk modulus based on Wang et al. (2001). Clay density varied from 2.4 g/cm^3 to 2.7 g/cm^3, and porosity was assumed to be 5%, which is about the average value in the Haynesville Shale. The effective V_P, V_S and V_P/V_S ratio from the combined self-consistent model and Chapman's model are shown in Figure 4.4. From the softest clay to stiffest clay, both V_P and V_S increase about 30%, and V_P/V_S ratio decreases about 2.2%, suggesting that the effect of clay on velocities is not negligible. Because clay minerals typically absorb water, which makes in situ clay composites softer than pure clay minerals (Wang et al., 2001; Vanorio et al., 2003), we used the relatively soft clay properties from classic gulf type clays (Tosaya, 1982; Han et al., 1986; Blangy, 1992), with bulk modulus of 21 GPa, shear modulus of 7 GPa, and density as 2.58 g/cm^3 (4.2).

Due to its undefined structure and mineralogy, kerogen also has large uncertainties for its moduli and density. Based on vitrinite reflectance, a measurement of the maturity of the organic material, Eastwood and Hammes (2011) obtained the kerogen density as 1.45 g/cm^3 for the Haynesville Shale. The bulk and shear moduli (2.9 GPa and 2.7 Gpa) of kerogen we used were from Carmichael (1989) and Blangy (1992) (Table 2.2).
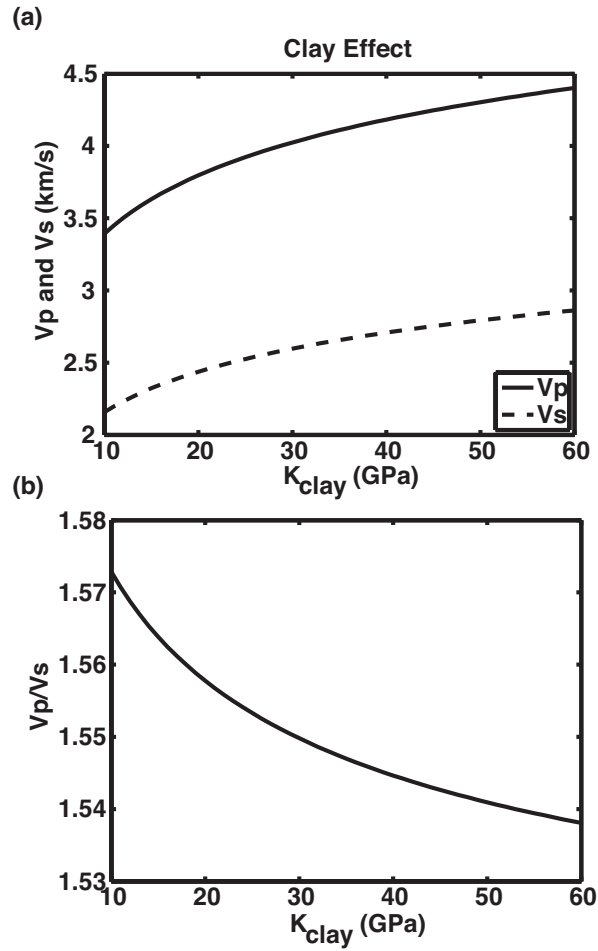
Figure 4.4: Investigation of how V_P, V_S, and V_P/V_S vary with different clay elastic moduli and densities, due to large uncertainties on elastic properties of clay. (a) V_P (solid) and V_S (dashed) increase about 30% from the softest clay to stiffest clay; (b) V_P/V_S ratio decreases about 2.2% from the softest clay to stiffest clay.

As for the fluid, we used the fluid mixing equation

$$K_{fluid} = (K_b - K_g)(1 - S_g)^e + K_g \qquad (4.10)$$

from Brie et al. (1995) to calculate the effective fluid moduli of a brine and gas mixture. In equation 4.10, the effective bulk modulus depends on the bulk moduli of brine (K_b) and gas (K_g) (Table 2.2), the gas saturation (S_g) and an empirical exponent (e). The gas saturation is from the average water saturation (~25%) in the Haynesville Shale. The empirical exponent e varies from 1 for patchy saturation to 3.4 for uniformly saturation. Here the patchy saturation provides the upper bound of effective bulk modulus of the mixed fluids, and uniform saturation provides lower bound of effective bulk modulus of the mixed fluids.

In Brie's fluid mixing equation, different exponents correspond to different fluid properties. We investigated how two specific cases of exponents in the equation affect the model results (Figure 4.5). One is uniform saturation with e=3.4 (Figure 4.5a), and another one is very close to patchy saturation with e=1.17 (Figure 4.5b). The crossplots of modeled V_S and V_P in these two cases show different shapes and color patterns, and the gray data dots fall into locations with different color ranges, indicating the two cases provide slightly different porosity estimates. For the uniform saturation case, the dark blue areas covered by most of data points suggests that porosity estimations are mostly close to 0; for the nearly patchy saturation case, the blue and cyan areas covered by most of the data points suggests that porosity estimations are mostly around 5%, which is about the average porosity value of the Haynesville Shale. Therefore, for this data, 1.17 is a suitable value to be used for the exponent e in Brie's fluid mixing equation.
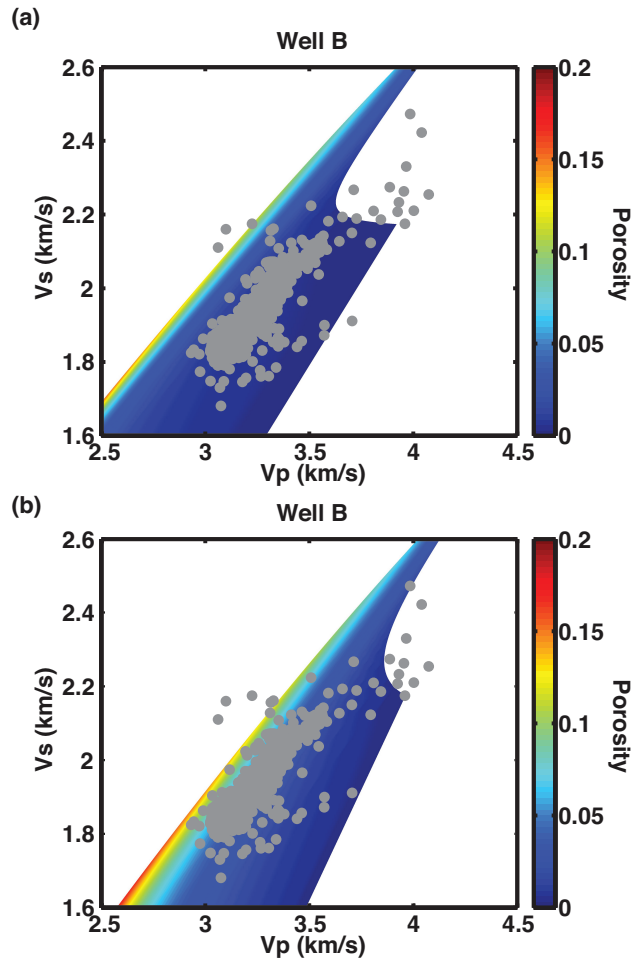
Figure 4.5: The effect of fluid mixing using different exponent values in Brie's fluid mixing equation (equation 4.10). (a) Exponent value e=3.4. In the crossplot of V_S versus V_P, gray dots are data from Well B, and background color shows the modeling result colored by prior total porosity. (b) Exponent value e=1.17. Gray dots are data from Well B, and background color shows the modeling result colored by prior porosity. In this case, the data points correspond to a more accurate porosity range than in (a) based on porosity from the well.

4.7 RESULTS

Results of the rock-physics modeling (Figure 4.6) showed that V_P and V_S were constrained both separately and simultaneously by the combination of the self-consistent model and Chapman's model. The crossplots of V_P versus porosity (Figure 4.6a) and V_S versus porosity (Figure 4.6b) colored by prior composition demonstrate how V_P and V_S vary with prior porosity and prior composition. In both plots, gray points are observed data from Well B. When the composition varies from clay- and kerogen-rich (cold colors) to quartz- and calcite-rich (hot colors), V_P and V_S increases because the bulk moduli of quartz and calcite are larger than those of clay and kerogen. To determine if the model works for both V_P and V_S simultaneously, we generated a crossplot of V_S versus V_P, with modeling results colored by both prior distributions of porosity (Figure 4.5b) and composition (Figure 4.6c). The variations of modeled V_P and V_S depend on the combined effects of porosity, composition and aspect ratio. Although it appears that V_S increases with porosity (Figure 4.5b), it is the increase of rock stiffness (Figure 4.6c) that causes the increase of V_S. Both figures (Figures 4.5b and 4.6c) show that most of the data points fall within the model, and the model followed the trends of data very well, suggesting that Chapman's model worked well for both V_P and V_S simultaneously, given the prior distributions of porosity, composition, and pore aspect ratio. Therefore, by combining the modeled V_P and V_S results, the porosity, composition, and pore aspect ratio distributions could be estimated simultaneously.
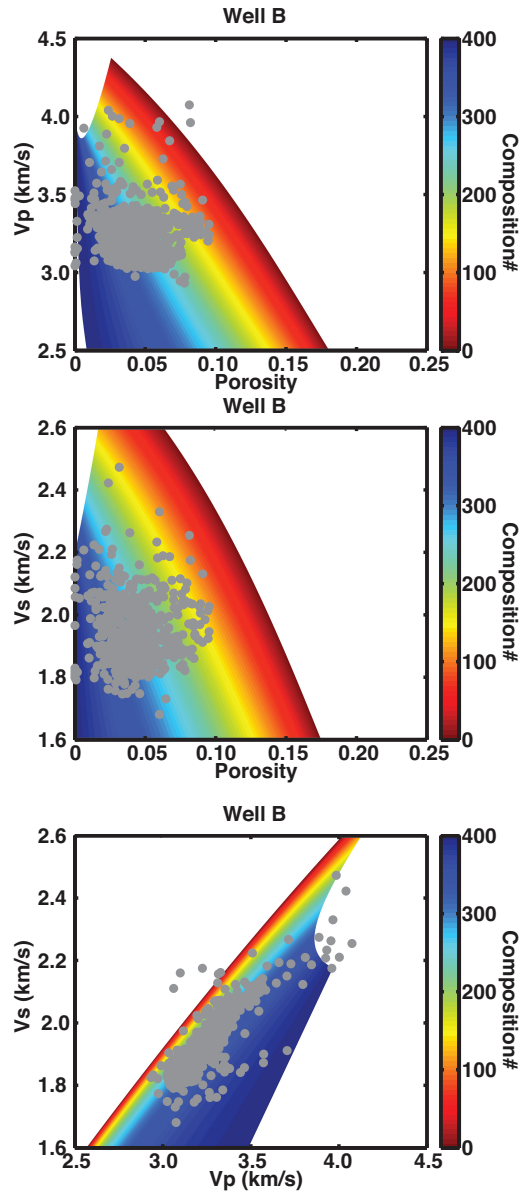
Figure 4.6: (a) Crossplot of V_P versus porosity. Gray points are data from Well B. Background color shows the modeling result with the prior composition distribution. (b) Crossplot of V_S versus porosity. Gray points are data from Well B. Background color shows the modeling result with the prior composition distribution. (c) Crossplot of V_S versus V_P, colored by prior composition distribution. Almost all the data points were covered by the modeling results, and the modeling results followed the data trend very well. The data points that were missed by the model likely correspond to dolomite-rich composition excluded from the prior composition distribution.

85

In the model (Figures 4.5b and 4.6c), the area that covers the majority of the data points has different colors, indicating there are variations in porosity, composition and aspect ratio. Meanwhile, although a few points fall in the blue area, they correspond to a small range of porosity and composition, and relatively large uncertainty of their estimations. The model missed only a few points. One possible reason is that the prior distribution of composition did not account for some extreme cases with very high dolomite percentages. Using a different parameterization of the rock-physics model based on rock-type classification might make the model work even better.

Grid searching was used to estimate distributions of porosity, composition, and pore aspect ratio after rock-physics modeling. The combination of the self-consistent model and Chapman's model provided trends of V_P and V_S that explain the variations in the log data. By comparing modeled V_P and V_S with observed V_P and V_S, we simultaneously inverted porosity, composition, and aspect ratio. The criteria was to accept modeled V_P and V_S that have differences less than 0.08 km/s (~2% error for V_P and ~4% error for V_S) comparing to the observed V_P and V_S. At each depth, multiple porosities, compositions and aspect ratios satisfy the criteria. We calculated the probability of each accepted value based on the number of accepted values and number of total values. In this way, we obtained not only just the best-fit reservoir properties, but also multiple fitted sets of reservoir properties with different probabilities.

The porosity estimation closely matched the porosity within the Haynesville Shale (Figure 4.7). At each depth, we obtained porosity estimates with different probabilities (Figure 4.7a), showing by the background colors, with the hot colors representing higher

probability and cold colors representing lower probability. The porosity estimation fits the density porosity in terms of both value and the overall depth trend even though the inversion was performed independently at each depth location. The average estimated porosity is 4.6%, and density porosity is about 4.2%. They both have standard deviation of about 0.02. The estimated porosity shows a small systematic bias toward the high value side, mainly due to the fluid property uncertainty in the rock physics models. The histograms of density porosity (Figure 4.7b, top) and the best fit porosity (Figure 4.7b, bottom) are very similar.

The best-fit composition assemblage was estimated at each depth in the Haynesville Shale formation (Figure 4.8a). The average percentages for quartz, calcite, pyrite, kerogen, and clay are very close to the ones from core analsyis and XRD results in Well A (Table 4.2). They are not exactly the same because lithology from Well A and Well B may be slightly different. Certain depths, such as 2360 m, 2406 m and 2413 m, display much higher percentages of quartz (~39%) and calcite (~31%), and much lower percentage of clay (~24%) than average within the Haynesville Shale. These features are consistent with the peaks in V_P and V_S logs (Figure 4.8b), and they likely correspond to more brittle zones.

Table 4.2. Comparison of compositions in percentage from modeling and measurement

	Qtz (%)	Calcite (%)	Pyrite (%)	Kerogen (%)	Clay (%)
Model (Well B)	31.3	23.3	2	4.7	38.7
Measurement (Well A)	31.6	25.8	2	5.3	35.3

[1] Blangy (1992); [2] Carmichael (1989); [3] Eastwood and Hammes (2011); [4] Han et al. (1986); [5] Tosaya (1982)
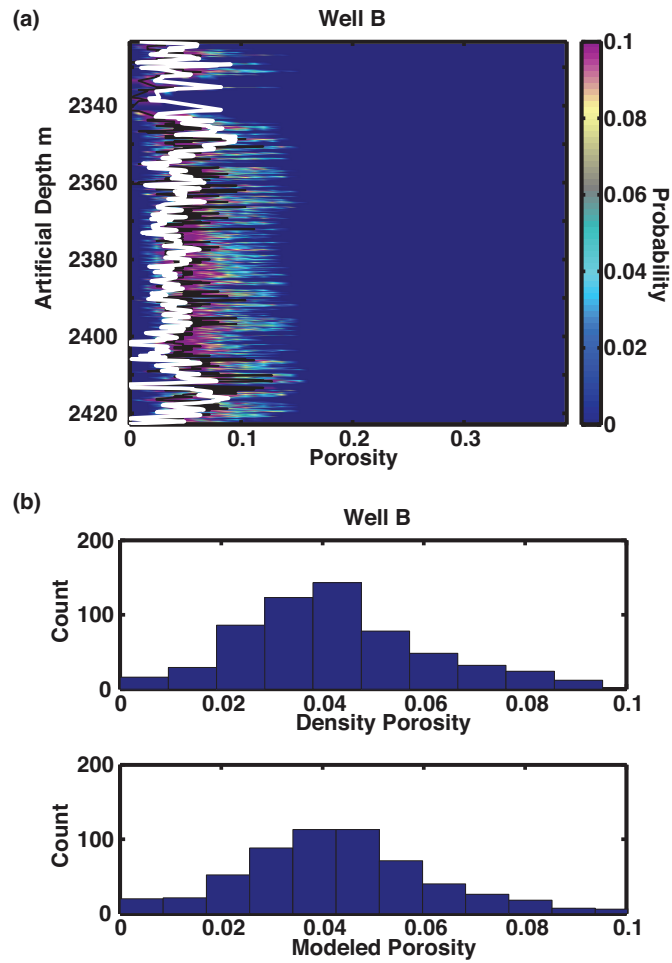
Figure 4.7: (a) Porosity estimation. Background color represents probability, with the hot colors representing estimations with higher probability, and cold colors representing estimations with lower probability. The black curve marks the estimation with the highest probability, and the white curve shows the density porosity from log data. (b) Histograms of observed and modeled porosity. Average estimated porosity is 4.6%, average density porosity is 4.2%, and both have standard deviation of about 0.02.
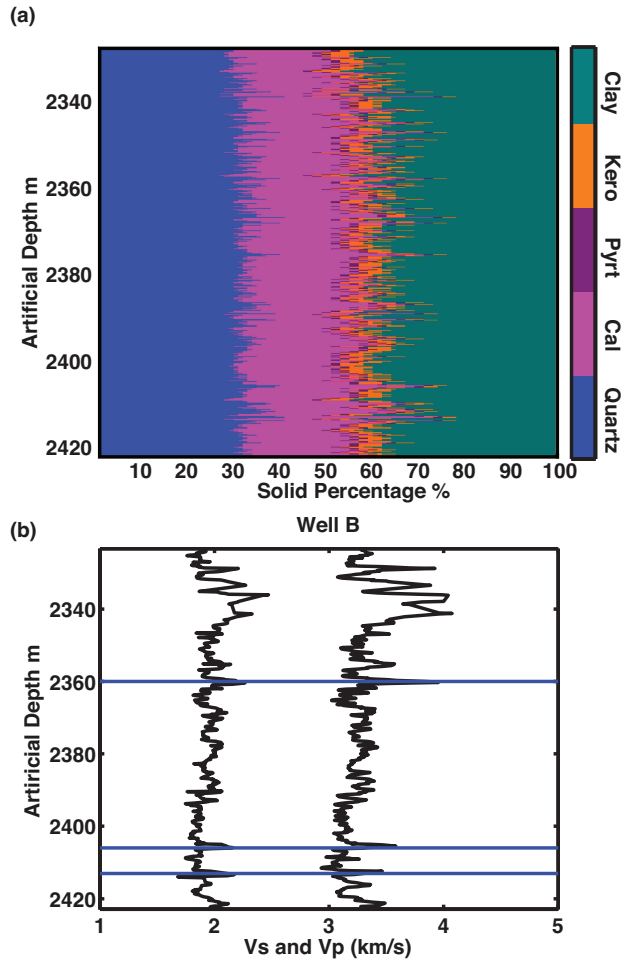
Figure 4.8: (a) Composition assemblages along artificial depth. Each depth contains different percentages of quartz, calcite, pyrite, kerogen and clay. (b) P- and S-wave velocities within the Haynesville Shale. A few peaks (marked by the blue line) of V_P and V_S at certain depths (~2360 m, ~2406 m, and ~2413 m) correspond to more brittle zones with high quartz percentage (about 39%), high calcite percentage (about 31%) and low clay percentage (about 24%).

The pore aspect ratio estimation with different probabilities was obtained at each depth (Figure 4.9a), and the histogram of the best aspect ratio estimation (Figure 4.9b) within the Haynesville Shale indicates that the estimation generally follows a normal distribution. The average value of the best estimated pore aspect ratio is about 0.04, with

89

standard deviation of about 0.016. It is difficult to verify the pore aspect ratio estimation because there was no direct maesurement available. However, by looking at microstructure images of core samples, we can obtain some idea of the pore/crack/fracture shapes and partially verify the aspect ratio estimation.
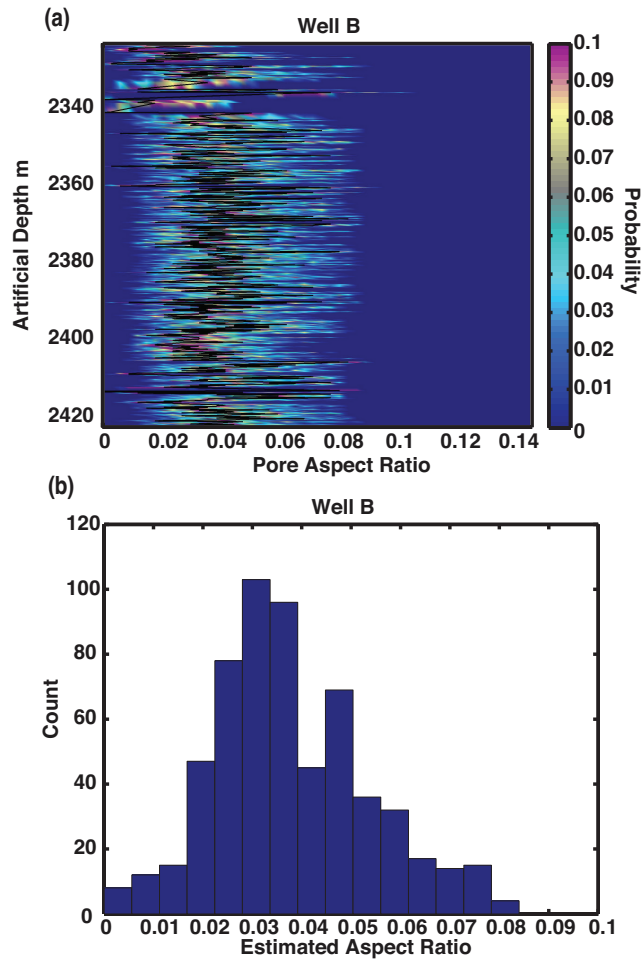
Figure 4.9: (a) Pore aspect ratio estimation. Hot colors represent estimates with higher probability, and cold colors are for lower probability. The black curve marks the estimation with the highest probability. (b) Histogram of the estimated aspect ratio. It generally follows a normal distribution, with a mean of about 0.04 and standard deviation of about 0.016.

The porosity and aspect ratio estimations are from a dual pore system based on the self-consistent model and Chapman's model. The self-consistent model has randomly oriented non-spherical pores that are isolated, and Chapman's model contains spherical pores, cracks and fractures that are connected. Most of the inverted porosity and aspect ratio distributions are dominated by the randomly oriented non-spherical pores from the self-consistent model. The fractures in Chapman's model do not contribute significantly to the total porosity, but they do affect the directional velocities.

From the correlations among the estimated porosity, composition and aspect ratio (Figure 4.10), the estimated aspect ratio decreases as the clay percentage in estimated composition increases (composition # increases) and estimated porosity decreases (hot color to cold color). The estimated aspect ratio increases as clay percentage decreases (composition # decreases) and estimated porosity increases. These correlations are consistent with the fact that it is easier to compress soft clay than other stiffer minerals and therefore generate more flatten pores. Also, the points with higher estimated clay percentages, lower estimated porosities and lower estimated aspect ratios are not as scattered as the ones with lower estimated clay percentages, higher estimated porosities and larger estimated aspect ratios. The pattern of these scattered points indicates that uncertainties are relatively small for the locations with higher clay percentage, lower porosities and smaller aspect ratios.
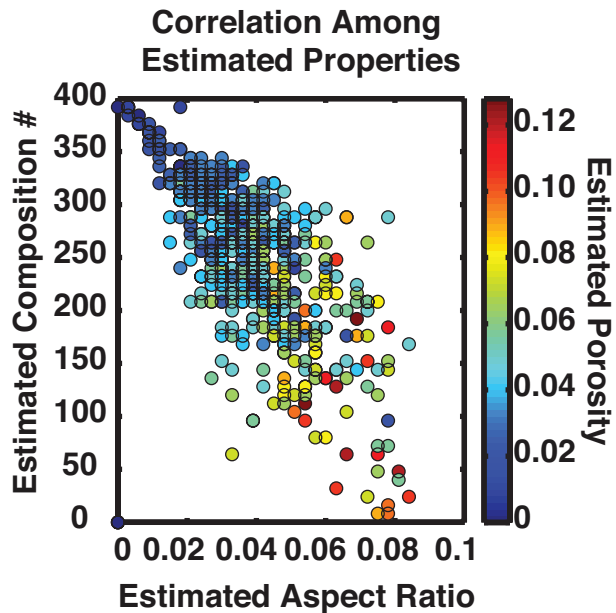
Figure 4.10: Correlations among estimated porosity, composition and aspect ratio. These correlations are preserved from correlations among their prior distributions. As estimated clay percentage increases and estimated porosity decreases, the estimated aspect ratio decreases. The pattern of the scattered points indicates estimation uncertainties. The more scattered points correspond to lower estimated clay percentages, higher estimated porosities, and larger estimated aspect ratios. The more condensed points correspond to higher estimated clay percentages, lower estimated porosities, and smaller estimated aspect ratios.

4.8 DISCUSSION

In this chapter, the fluid was directly put into the void spaces. We did not use Gassmann's fluid substitution to calculate bulk and shear moduli of the fluid-saturated rock from the dry rock frame in the self-consistent model. Gassmann's fluid substitution equations are based on several assumptions (Gassmann, 1951; Smith et al., 2003), including a homogeneous and isotropic rock matrix and low frequency so that the pore pressures are equilibrated throughout the pore space. The Haynesville Shale has extremely low permeability, and, therefore, the fluid mobility is very low, which suggests

that the Haynesville Shale falls in the high-frequency regime, and the low-frequency assumption of Gassmann's equation fails (Batzle et al., 2006). In addition, in the self-consistent model, the pores are isolated with respect to fluid flow and pore pressures are not equilibrated. Therefore, we believe it is correct to model the elastic components with the fluid placed in the void space as opposed to modeling dry rock and then applying fluid substitution. The frequency used in Chapman's model (10 kHz) is right at the edge of where dispersion begins, and the amount of dispersion is very small. Even though the dual porosity system is not exactly consistent with Gassmann, we consider the velocity dispersion to be negligible.

Reservoir properties (composition, porosity and pore shape) were estimated for the Haynesville Shale, along with the associated uncertainty. Sources of uncertainty that might affect these results, in addition to elastic properties of clay, kerogen, and fluid, are the log measurements and calculations made from those measurements. Porosity is not directly measured at the log scale, and is calculated from either the density log or neutron log. In this chapter, the porosity log was calculated from the density log. This calculation relied on the accuracy of density log measurement, which is very sensitive to the borehole environment. The calculation also relied on the assumptions of fluid density and rock matrix density at each depth, which is sensitive to the composition assemblage and water saturation at each depth. In this chapter, composition is partially constrained by core measurements of Well A.

This chapter focused on reservoir characterization at a single well location. The process can be expanded to the larger seismic scale by combining the modeling with 3D

93

surface seismic data. Seismic inversion, calibrated properly, provides V_P and V_S for a 3D volume. Once those elastic properties at the large scale are input to our algorithm, we will be able to estimate the 3D distributions of the reservoir properties. On the one hand, measurement scale is an issue when comparing seismic velocities from rock-physics models and from seismic inversion. Log data are measured at sub-meter resolution and at frequency of tens of kHz, whereas seismic data is a time measurement with frequencies of tens of Hz. Upscaling is required from the log scale to seismic scale. The Backus (1962) average, a long wavelength effective medium approximation, can be used to help solve this issue. On the other hand, non-uniqueness also is present in both seismic inversion and rock-physics modeling. In seismic inversion, different inverted impedances may provide equally well fitted seismic traces, and it is impossible to obtain unique solutions of the P- and S-impedances. In this case, constraints at well locations are very important. In the rock-physics modeling, different combinations of prior reservoir properties may result in the same elastic properties, adding more non-uniqueness in estimating the reservoir property distributions. Therefore, assessment of uncertainties and ambiguity is important when characterizing the reservoir properties at each scale and across scales.

The continuous distributions of the reservoir properties will contribute to understand the spatial variations of seismic attributes within this study area of the Haynesville Shale. The procedures in this chapter could also be applied to other gas shales other than the Haynesville Shale in order to characterize their reservoir properties. Applications to other shales, however, must begin with determining the site-specific

reservoir properties that most significantly affect the seismic properties as well as the associated uncertainty.

4.9 CONCLUSION

In this chapter, we developed a workflow to characterize the reservoir properties of the Haynesville Shale. We modeled both V_P and V_S simultaneously using a combination of the self-consistent model and Chapman's model, and inverted porosity, composition and pore aspect ratio distributions from grid searching. The self-consistent model provided a porous rock matrix that contained different mineral phases and non-spherical pores as inputs in the Chapman's model. Chapman's model outputs anisotropic stiffnesses as function of frequency, porosity, fracture density, and lithology. The modeling was successful for Well B and provides relationships between the reservoir properties (porosity, composition, and pore aspect ratio) and elastic properties (V_P and V_S). The integration of the rock-physics model with grid searching provided simultaneous estimates of porosity, composition and pore aspect ratio distributions for the Haynesville Shale. Estimation of porosity helps to determine gas capacity and the estimated ultimate recovery (EUR). Estimations of composition and pore aspect ratio help to understand the stiffness and brittleness of rock formations, which might contribute to locating sweet spots and identifying zones of economic production in unconventional reservoirs. Here, sweet spots are preferable locations at which to place hydraulic fractures in rock formations that contain more brittle compositions and with relatively high porosities and large pore aspect ratios.

95

Chapter 5: Application of rock-physics modeling, grid searching, and prestack seismic inversion in seismic reservoir characterization of the Haynesville Shale

5.1 ABSTRACT

Seismic reservoir characterization of unconventional gas shales is challenging due to their heterogeneous and anisotropic complexity. Rock properties of unconventional gas shales such as porosity, pore-shape distribution, and lithology are important for interpreting seismic data amplitude variations for shales. This chapter estimates these rock properties at the seismic scale by applying rock-physics modeling, grid searching, and prestack seismic inversion, using the Haynesville Shale as a case study. This seismic reservoir characterization procedure accounted for the complex composition, pore-shape distribution, and anisotropy. All of the above rock properties affected the seismic velocities, and the combined effects of these rock properties on the seismic amplitude were investigated simultaneously. The P- and S-impedances correlated negatively with porosity. The V_P/V_S correlated positively with clay fraction and negatively with the pore-shape distribution and quartz fraction. These estimated rock properties at the seismic scale were validated further through the comparisons between the elastic properties derived from the estimated rock properties and the ones inverted from the prestack seismic data. The differences between the two sets of elastic properties were less than a few percent. These correlations between the seismic amplitude variations and the rock properties contribute to the seismic reservoir characterization of the Haynesville Shale.

96

5.2 INTRODUCTION

Seismic data provides images of structures and stratigraphy in the subsurface for reservoirs of interest. In exploration and production, seismic amplitude data can be used to predict reservoir properties for areas away from wells. The seismic responses depend on impedance contrasts, and the responses often vary spatially in the reservoirs, particularly for unconventional gas shales, due to their complexity and heterogeneity. In seismic reservoir characterization, understanding which rock properties or combination of properties cause these spatial variations is important. For complex unconventional gas shales, rock properties, including porosity, pore-shape distribution, and lithology are important to identify optimal drilling locations. Porosity helps to determine gas capacity and estimated ultimate recovery (EUR), and, therefore, zones of economic production. Pore-shape distribution and lithology are related to the brittle/ductile strength of shales and, therefore, contribute to identify zones suitable for hydraulic fracturing.

Shales are heterogeneous, with low porosity, low permeability, and commonly they contain natural fractures. There are large petrophysical and elastic variations for shales in terms of depth, thickness, porosity, permeability, pressure, temperature, and TOC (Roth, 2011). On the production side, gas shales present large variations in thermal maturity, adsorbed- or absorbed-gas fractions, reservoir thickness, total organic carbon (TOC), and volume of gas in place (Curtis, 2002). Because of the heterogeneity and anisotropy, seismic reservoir characterization for shales is challenging. Chopra et al. (2013) reviewed current workflows for shale gas reservoir characterization, including calculating TOC content, estimating brittleness of rock formation from Poisson's ratio

97

and Young's modulus, and detecting natural fractures in shale formations from azimuthal variations of velocity and/or impedance fields. Zhu et al. (2011) used rock-physics relationships and seismic modeling to understand the geophysical responses of shale-gas plays at both well log and seismic scales. They found that the mineral composition and interaction among minerals affected geophysical responses and/or rock strength and fracability of the rock. Koesoemadinata et al. (2011) introduced a workflow that involved seismic acquisition, processing, and prestack inversion to characterize the Marcellus Shale and classify the lithofacies. They identified four major lithofacies (silts and sand, shale, limestone, and dolomite) and found that the Marcellus formation in their study area was highly heterogeneous elastically. Sena et al. (2011) developed a workflow that integrated prestack azimuthal seismic data analysis and well-log information to estimate geomechanical properties of shales and to identify sweet spots. They estimated differential horizontal stress ratio, fracture-initiation pressure, and closure pressure, which are critical parameters for the fracture simulation process. Guo et al. (2013) constructed a rock-physics workflow in which the clay and kerogen particle orientations were defined, and applied this workflow to the Barnett Shale and evaluated porosity, lithology and brittleness index. They found that Poisson's ratio and Young's modulus along the well path decrease as clay content increases, and Poisson's ratio is a more reliable indicator than Young's modulus to discriminate clay content and shale texture (orientation of clay particles) at high porosities. Loseth et al. (2011) built a relationship between TOC and acoustic impedance and used this relationship to predict TOC volumes from inverted acoustic impedance volumes. They showed a significant nonlinear

reduction in acoustic impedance with increasing kerogen content, and they mapped the source rock presence, thickness, and basin-wide variations in TOC.

The anisotropy of shales is always an important aspect to be considered when performing seismic reservoir characterization. Sayers (2013) examined the effect of anisotropy (partial orientation of clay particles, the presence of silt particles, kerogen inclusions, microcracks and low-aspect ratio pores) on the directionally dependent Young's moduli and Poisson's ratios for transversely isotropic shales. He pointed out that the degree of alignment of clay particles and presence of low-aspect ratio pores in shales affects the Poisson's ratios and Young's moduli along different directions. The presence of silt inclusions increases the Young's moduli and decreases the Poisson's ratios, and the presence of kerogen inclusions decreases the Young's moduli and Poisson's ratios. Bachrach et al. (2013) applied both deterministic and stochastic rock-physics modeling to predict anisotropy and constrain the ranges of anisotropic parameters of shales and sandy shales. Their anisotropy predictions were consistent with effective medium theory, and they were able to use the rock model to fit an anisotropy profile derived from checkshot data.

Jiang and Spikes (2011) investigated the pore shape and composition effects on the P-wave velocity for the Haynesville Shale at the well log scale and showed that shales with stiffer composition and more rounded pores have higher velocities than the ones that have softer composition and flattened pores. A workflow that accounted for heterogeneity and anisotropy of shales was introduced to characterize the above rock properties of the Haynesville Shale (Jiang and Spikes, 2013a). The estimated compositions at the well log

scale were similar to the log data/core measurements. A preliminary study on applying that workflow at the seismic scale was done (Jiang and Spikes, 2013b). However, only a small number of seismic traces were analyzed, and the relationship between the rock properties and seismic attributes were investigated at a few individual locations instead of continuous slices or volume.

This chapter combined rock-physics modeling, seismic inversion, and grid searching to provide rock-property estimations at the seismic scale for the Haynesville Shale. The estimated rock properties were also validated. Although the seismic-inversion algorithm was isotropic, the anisotropic rock-physics modeling was able to account for anisotropy of shales. The estimated rock properties from the workflow generated similar P- and S-impedances to the ones obtained from prestack seismic inversion. The variations of these rock properties were correlated with the seismic amplitude data variations. The P- and S-impedances correlated negatively with porosity, and the V_P/V_S correlated positively with clay fraction and negatively with the pore-shape distribution and quartz fraction. These correlations contribute to the seismic reservoir characterization of the Haynesville Shale.

5.3 STUDY AREA

5.3.1 Seismic Data Observation

The bottom of the Haynesville Shale can be clearly seen in the poststack P-wave seismic data (Figure 2.6). The strong positive reflection event at about 740 ms is due to the transition from the Haynesville Shale to Smackover Limestone. The top of the

Haynesville Shale (~700 ms) is not as evident as the bottom. There is a strong negative reflection (Figure 2.6) at the lower part of the Haynesville Shale between 720 ms and 740 ms. The color intensity changes from trace to trace, indicating the amplitude of this negative reflection varies spatially. Figure 2.5 shows a map view of the negative reflection near the base of the Haynesville Shale. The spatial variation of the P-wave seismic amplitudes can be clearly seen from the different colors. Understanding which rock properties cause the spatial variations in the seismic amplitude data is quite important for the exploration and production of the Haynesville Shale.

5.3.2 Petrophysical and Rock Property Observations

The well log data (Figure 5.1a) shows porosity, P-wave velocity (V_P), S-wave velocity (V_S) and density within the Haynesville Shale. Porosity is calculated from the density log maintaining the assumption that the rock matrix contains similar compositions to the interpolated core measurements (Figure 5.1b). At about 2418 m, there is a decrease in the V_P, V_S and density logs. On average, V_P decreases from 3.33 km/s to 3.16 km/s, V_S decreases from 2.00 km/s to 1.86 km/s, and density decreases from 2.50 g/cc to 2.47 g/cc. These variations correspond to the negative reflection at the base of the Haynesville Shale in the seismic data (Figure 2.6). Accordingly, there is an increase in the porosity log, which makes porosity a potential rock property that contributes to the spatial variations in the seismic amplitude.
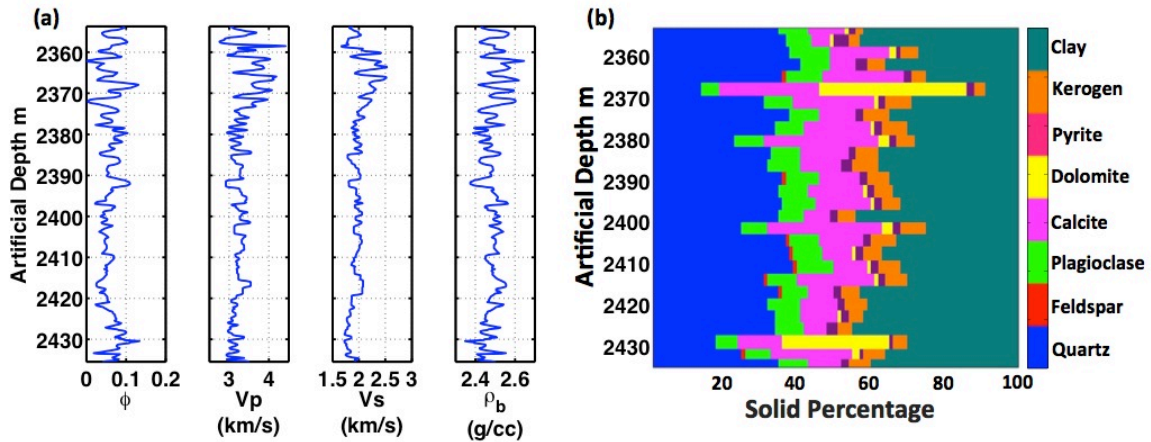
Figure 5.1: (a) Well log data within the Haynesville Shale from Well A. From left to right, density porosity, V_P, V_S, and density logs are plotted. At an artificial depth of about 2418 m, the velocity logs and the density log values decrease while the porosity values increase. (b) Composition percentages at different depths within the Haynesville Shale. Clay percentage increases and quartz and calcite percentages decrease at the bottom of the Haynesville Shale. The percentages of kerogen and other minerals do not show clear variations at about 2418 m.

Based on the core analysis and XRD measurements, the Haynesville Shale contains quartz, feldspar (potassium feldspar), plagioclase (calcium feldspar), calcite, dolomite, pyrite, kerogen and clay (Figure 5.1b). The dominant composition includes quartz, calcite and clay. The percentages of other minerals are relatively small. However, at certain depths, such as about 2368 m and 2429 m, there is a relatively large amount of dolomite. The organic matter, kerogen, varies from about 1.7% to 7.1%, with an average of about 5.3% within the Haynesville Shale. In the rock-physics models, to simplify the computation, the percentages of feldspar, plagioclase, and dolomite were transferred to calcite. Therefore, the average percentages of quartz, calcite, pyrite, kerogen, and clay from core are about 31.6%, 25.8%, 2%, 5.3%, and 35.3%, respectively. At about 2418 m, there is an increase of clay percentage and decrease of quartz and calcite percentages.

102

This composition variation is consistent with the velocity and density drops at the same depth because clay has lower density and bulk and shear moduli than quartz and calcite. Therefore, composition is another potential rock property that causes the spatial variations in the seismic amplitude.

Another rock property, the pore shape, was considered in this chapter. Pore shape is one of the rock properties that affects the elastic properties of rocks, and it is an important aspect to be considered for the reservoir characterization. Sayers and den Boer (2011) applied the self-consistent scheme on deepwater subsalt Gulf of Mexico shales and showed that different pore aspect ratios corresponded to different effective moduli. Bai et al. (2013) accounted for variable pore aspect ratios in the Xu-White model (Xu and White, 1995, 1996) and predicted more accurate shear-wave velocity than the conventional Xu-White model. The Haynesville Shale tends to have flattened or elongated grains and pores at the micro- and nano-scales scale (Curtis et al., 2010). Previous studies (Jiang and Spikes, 2011, 2012) showed that pore shape has a strong effect on the velocity for the Haynesville Shale. Generally, with the same composition and porosity, rocks that contain more rounded pores have higher velocities than the ones that have more flattened pores (Jiang and Spikes, 2011; Sayers and den Boer, 2011).

5.4 METHOD

Distributions of porosity, pore shape, and composition at the seismic scale were jointly inverted from P- and S-impedances for the Haynesville Shale. The seismic reservoir characterization workflow (Figure 5.2) included three major parts: rock-physics

modeling, grid searching, and prestack seismic inversion. In the seismic inversion step, bandpass filtering and partial stacking were applied to increase the S/N. The processed angle stacks were inverted for P- and S-impedances. The inverted P- and S-impedances were then input into the rock-physics modeling and grid searching process to estimate rock properties at the seismic scale. The elastic properties derived from the estimated rock properties and the ones inverted from the prestack seismic data were compared to validate the estimated rock properties. Both sets of impedances were at the seismic scale, because the estimated rock properties were at the seismic scale.
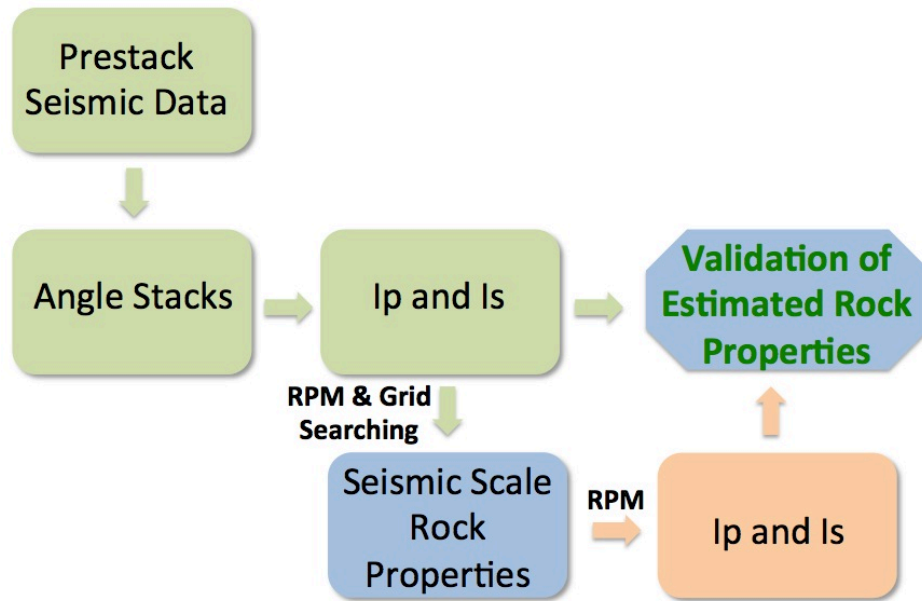
Figure 5.2: Workflow for the seismic reservoir characterization. Bandpass filtering and partial stacking was applied to the prestack angle gathers. The angle stacks were inverted for P- and S-impedances, which were then input into the rock-physics modeling and grid searching process to estimate rock properties at the seismic scale. To validate further the estimated rock properties, the elastic properties derived from the estimated rock properties were compared to the ones inverted from the prestack seismic data. Both sets of impedances are at the seismic scale.

5.4.1 Rock-Physics Modeling

The rock-physics modeling established quantitative relationships between the rock properties (porosity, pore-shape distribution and lithology) and the elastic properties (P- and S-wave velocities or P- and S-impedances. The rock-physics modeling included the self-consistent model (O'Connell and Budiansky, 1974; Berryman, 1980) and Chapman's model (Chapman, 2003). The details of the rock-physics modeling are described in Chapter 4. The self-consistent model initiates the numerical simulation by including grains and pores of different shapes and sizes, and Chapman's model treats the shale as a vertical transversely isotropic (VTI) medium by introducing aligned fractures. In the rock-physics modeling, the effective shale was built based on different mineral and pore phases. The mineral phases included quartz, calcite, clay, kerogen and pyrite. The pore phases included non-spherical/spherical pores, non-spherical cracks and aligned fractures. Calibration of the rock-physics model is described in detail in chapter 4.

In the rock-physics modeling, prior distributions of porosity, composition and pore shape were included. The prior composition included quartz, calcite, pyrite, kerogen and clay. Because pyrite comprised only a small portion of the composition, it was fixed at 2% in the rock-physics modeling. The percentages of the other compositions varied for 400 scenarios. The quartz and calcite contents were negatively related to the kerogen and clay contents. The prior porosity was from 0 to slightly more than 0.4, and the prior aspect ratio was from almost 0 to 0.12. The ranges of these prior distributions were large enough to contain most combinations expected in this interval. At the well log scale, the

porosity and composition estimations matched the observations quite well, with error less than a few percent (Jiang and Spikes, 2013a).

5.4.2 Grid Searching

After the rock-physics models were built, a grid searching method was used to estimate the rock properties and the associated uncertainties. In the grid searching, P- and S-impedances from the rock-physics models were compared with the ones inverted from the seismic data. The modeled impedances that satisfied specific criteria provided the estimated rock properties (equation 5.1).

$$Obj\_P = \mid IP_{model} - IP_{inverted} \mid \leq 0.2$$

$$Obj\_S = \mid IS_{model} - IS_{inverted} \mid \leq 0.1$$

$$(5.1)$$

For each trace at each time, grid searching provides a large number of estimated rock properties based on the objective function (equation 5.1). The mean value and standard deviation were calculated for each rock property at each point. The standard deviation shows the uncertainty of the estimations spatially and vertically.

5.4.3 Prestack Seismic Inversion

Simultaneous inversion (Hampson et al., 2005) of prestack seismic data was applied to obtain P-impedance, S-impedance and density. This algorithm was based on three assumptions (Hampson et al., 2005): a linearized approximation for reflectivity, the reflectivity as a function of angle can be calculated by Aki-Richards equations (Aki and

Richards, 2002), and the logarithm of P-impedance, S-impedance and density are linearly related.

The angle gathers at the well location (Figure 5.3a) were calculated from migrated offset gathers using the RMS and interval velocities. Incidence angles range from about 4° to 50°. Overall, these angle gathers have a relatively low S/N. In particular, the traces at large incidence angles (between about 30° to 50°) are noisier than the traces at smaller angles. A seismic-well-tie was done based on poststack seismic data that has much higher S/N than the prestack seismic data, with a correlation coefficient of 0.79. To enhance the S/N in the prestack data, super gather analysis and partial stacking were applied. Super gather process collects adjacent CDPs and adds them together to enhance the S/N. The number of CDPs to be added can be 3 by 3, 5 by 5, 7 by 7, and so on. The effect of CDP number was tested, and the grid of 5 by 5 was chosen to increase the S/N (particularly for the large angle gathers between about 30° to 50°), while preserving the main features shown in the original angle gathers (Figure 5.3b). Partial stacking further enhanced the S/N (Figure 5.3c). Three angle ranges were selected: 5°–15°, 15°–25°, and 25°–35°. Angles from 35°–50° were excluded due to relatively low S/N and nonexistence below about 700 ms. For each of the three angle ranges, the middle angle value was assigned to the angle stack, e.g., the angle stack from angle range 5°–15° had an angle value of 10°. In the simultaneous inversion, these three angle stacks (10°, 20°, and 30°) were treated as prestack angle gathers.
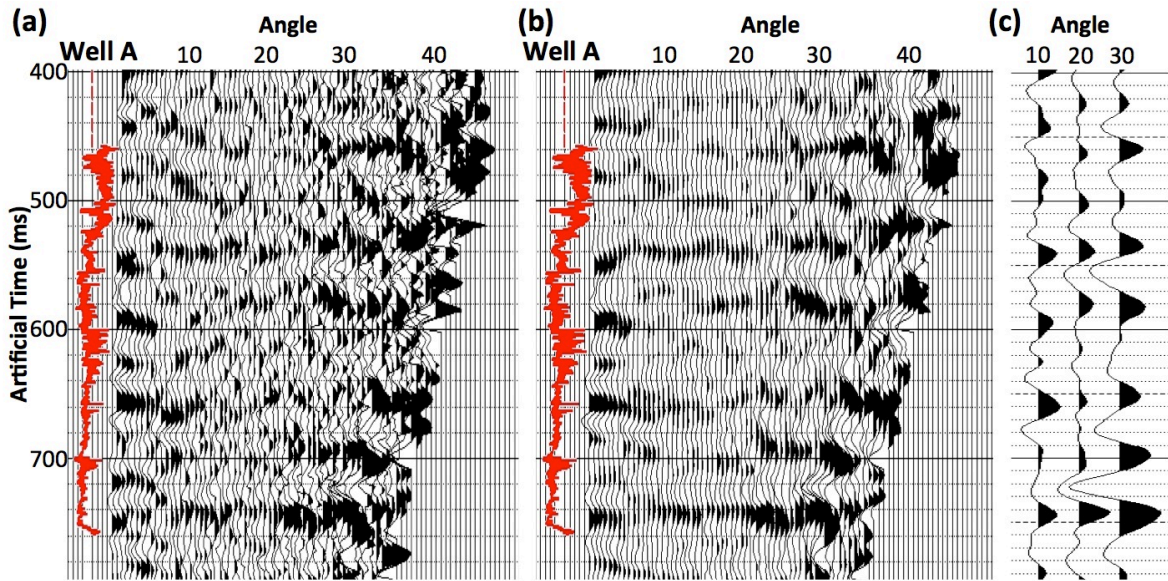
Figure 5.3: Prestack seismic data. a) The original CDP angle gathers at the well location (Well A), ranging from about 4° to 50°. The red curve shows P-impedance from Well A. From small to large angle ranges, the S/N decreases, and the traces at the largest angles (30°–50°) appear very noisy. b) The angle gathers after applying super gather process. The S/N increased, particularly at the very large angles (between about 30° to 50°). c) The angle stacks at the well location. Angle stacks were generated from angle ranges 5°–15°, 15°–25°, and 25°–35°. The middle values for each of the angle ranges (10°, 20°, 30°) were assigned to the angle stacks, respectively. Partial stacking significantly increased the S/N. The large amplitudes at large angle range correspond to data with low S/N and approaching criticle angle.

Analysis of the prestack inversion results at the well location is shown in Figure 5.4. The well log P- and S-impedances, density, and V_P/V_S are plotted in blue, the initial model is indicated by the black curves, and the inverted results are plotted in red in the first four panels. The initial P-impedance comes from the poststack inverted result, and initial density and V_P/V_S are from the log-derived low frequency model. The reason to use the poststack inverted P-impedance as the initial model is to get more constrain through the poststack seismic data that has higher S/N. The Haynesville Shale is marked by the

108

black box. In general, the inverted P- and S-impedance fit the measured impedances. Density matching between inversion and well log data is not as good as impedances because the density log itself fluctuates due to the rugose borehole environment. The inverted V_P/V_S has some obvious misfit with the borehole measurements, but fits the log measurements fairly closely within the Haynesville Shale. Synthetic seismic traces were created by convolving the inverted P-impedance with the wavelets extracted from the angle stacks. The synthetic angle stacks (red seismograms) are similar to the seismic data (black seismograms). The correlation coefficient is about 0.90, with relatively small error (red seismograms on right). The similarity between the synthetic seismic traces and observed seismic data indicates that the inversion results are generally acceptable. The crossplots between the inverted and well log P-impedances (Figure 5.5a) and S-impedances (Figure 5.5b) show nearly one-to-one relationships, indicating that the inverted P- and S-impedance are similar to the well log data.

5.4.4 Validation of the Inverted Rock Properties

The spatially continuous rock properties were estimated simultaneously by inputting the prestack seismic inverted elastic properties from the Haynesville interval into the rock-physics modeling and grid searching. For each of the rock properties, both the estimation and uncertainty (standard deviation) were calculated. These rock properties were validated further through the comparisons between the elastic properties derived from them and the ones inverted from the prestack seismic data. Based on the estimated rock properties at the seismic scale, the calibrated rock-physics model

generated a set of elastic properties. Those elastic properties should be close to the ones

from the prestack seismic inversion if the estimated rock properties are valid.
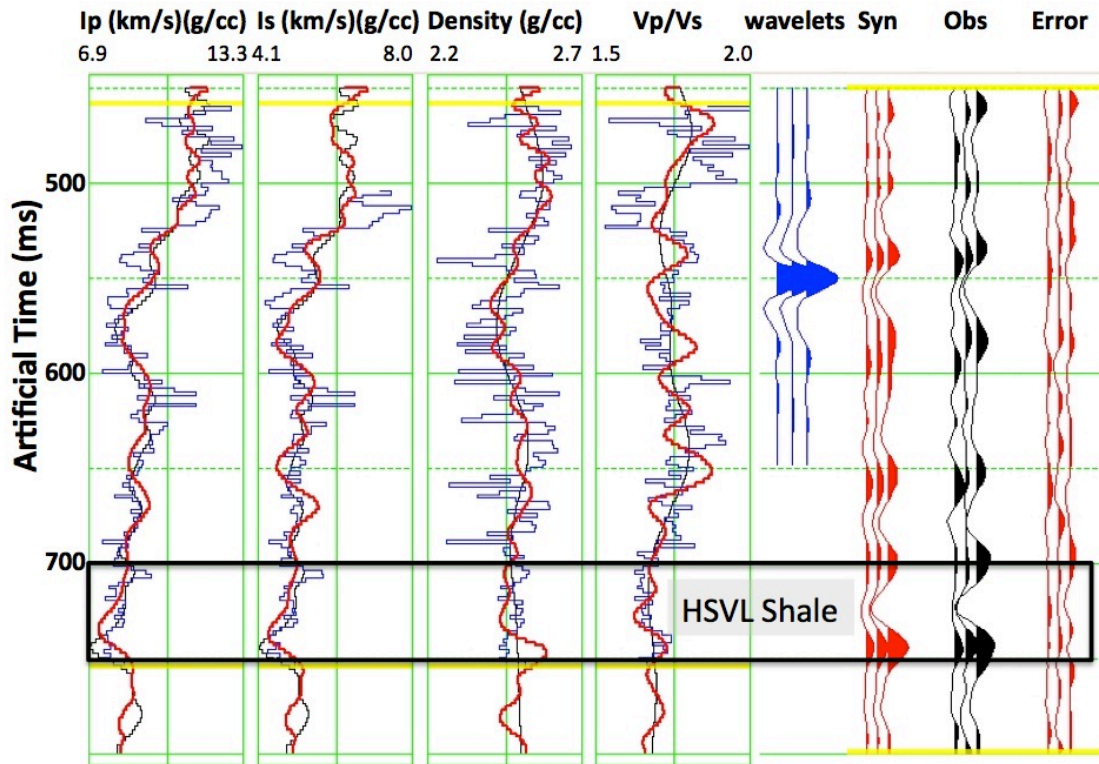
Figure 5.4: Prestack seismic inversion analysis at Well A location. The first four panels
show P-impedance, S-impedance, density, and V_P/V_S. The blue curves indicate
blocked well logs, black curves indicate initial model, and red curves indicate
seismic inverted results. The fifth panel shows wavelets extracted from the partial
stacked angle gathers at small, middle, and large angle ranges. The right three
panels show the synthetic seismic traces, partial stacked angle gathers from data,
and the difference between the two. The synthetic seismic traces are very similar
to the observed angle gathers, with a correlation coefficient of about 0.90. The
black box indicates the Haynesville Shale, to which the rock-physics modeling
and grid searching was applied.
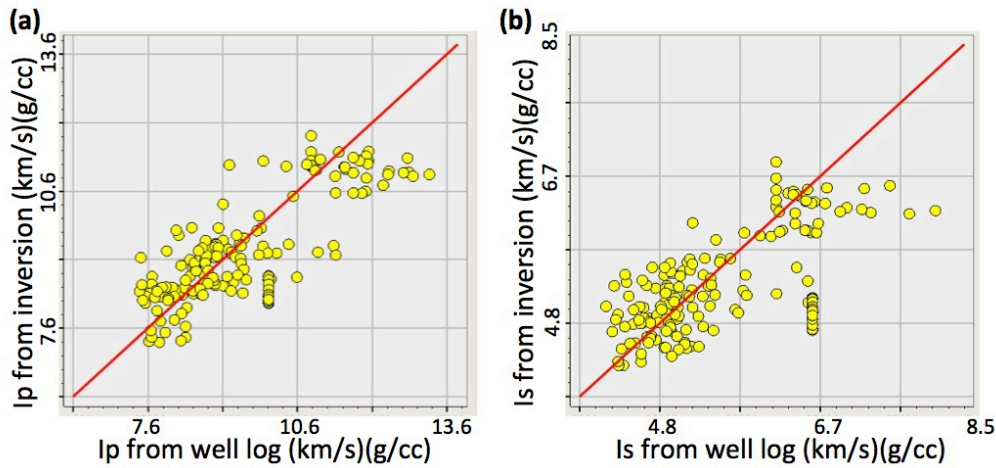
Figure 5.5: a) Crossplot of P-impedance from inversion versus the one from well log (from about 450 ms to 750 ms). b) Crossplot of S-impedance from inversion versus the one from well log (from about 450 ms to 750 ms). The red curve in each panel is the one-to-one line. Both crossplots indicate similarity between the well and inverted impedances.

5.5 RESULTS

5.5.1 Rock-physics Modeling Results and Calibration at the Well Location

The rock-physics models in Chapter 4 modeled the P- and S-wave velocities from the well log data simultaneously. In this chapter, the same rock physics models were applied to the seismic inverted P- and S-impedances. The modeling result at the seismic scale (Figure 5.6) shows that the rock-physics models also modeled the seismic inverted P- and S-impedances simultaneously. In Figure 5.6, the crossplot of S-impedance versus P-impedance were colored by the prior porosity (Figure 5.6a) and prior composition (Figure 5.6b). The black points are from the well logs, gray points are from the smoothed well logs, and magenta points are from the seismic inversion for Well A. The three sets of P- and S-impedances show similar trend. All the magenta points were covered by the

111

modeled results, and the modeling trend followed the magenta point trend very well, indicating that the rock-physics models explained the inverted P- and S-impedances. Therefore, the porosity, composition and pore shape distribution at the seismic scale were obtained.
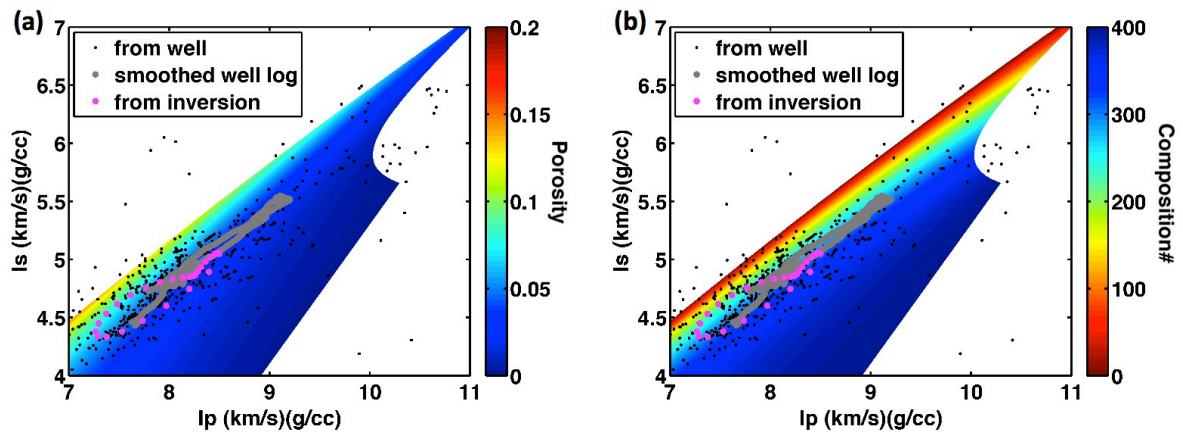
Figure 5.6: The rock-physics modeling result. Crossplot of S-impedance versus P-impedance, colored by prior porosity (a) and prior composition (b). Black points show the P- and S-impedances from the well log, gray points show the P- and S-impedances from the smoothed well log, and magenta points show the P- and S-impedance from the seismic inversion at the Well A. The three sets of P- and S-impedances show similar trend. All the magenta points were covered by the modeling results, indicating that the rock-physics models explain the seismic inverted P- and S-impedance simultaneously.

The rock property estimations at the well log scale are shown in Figure 5.7. At each time, we calculated multiple estimated pore aspect ratio, porosity and composition assemblage based on the objective function in the grid searching, and then randomly selected 100 estimates from the calculations. Therefore, we obtained the probability of estimations (background color in Figure 5.7a and 5.7b), the mean value of the estimations

(blue curve in Figure 5.7a and 5.7b), and estimations with the highest probability (magenta curve in Figure 5.7a and 5.7b) for the rock properties at each time. The mean value and the value with the highest probability of the estimations are similar, while the mean value curve is smoother along the time (or depth). There is an increase of both porosity and pore aspect ratio below 720 and 740 ms. The estimated porosity is similar to the density porosity (red curve, Figure 5.7b), particularly to the smoothed version (black curve, Figure 5.7b). The average value of the estimated porosity indicated by the blue curve is 5.4% within the Haynesville Shale, and the average density porosity is 6.1%. The composition assemblage (Figure 5.7c) is from the mean value of the estimated composition at each time. Different percentages of quartz, calcite, pyrite, kerogen and clay at different depths are present at each time. The estimated average percentages for quartz, calcite, pyrite, kerogen and clay are 30.8%, 22.8%, 2%, 4.8% and 39.6%, respectively. These numbers are close to the ones from core measurements, which are 31.6%, 25.8%, 2%, 5.3%, and 35.3%, respectively.

Further steps were applied to check the validation of the estimated rock properties. Based on the estimated rock properties, the calibrated rock-physics model generated a set of elastic properties (P- and S-impedances). Those derived elastic properties were then compared with the ones from the prestack seismic inversion. The black set of impedances (Figure 5.8) indicates the ones from seismic inversion, and the blue set of impedances (Figure 5.8) indicates the ones derived from the estimated rock properties. These two sets of P- and S-impedances are very similar, indicating that the estimated rock properties are valid.

113
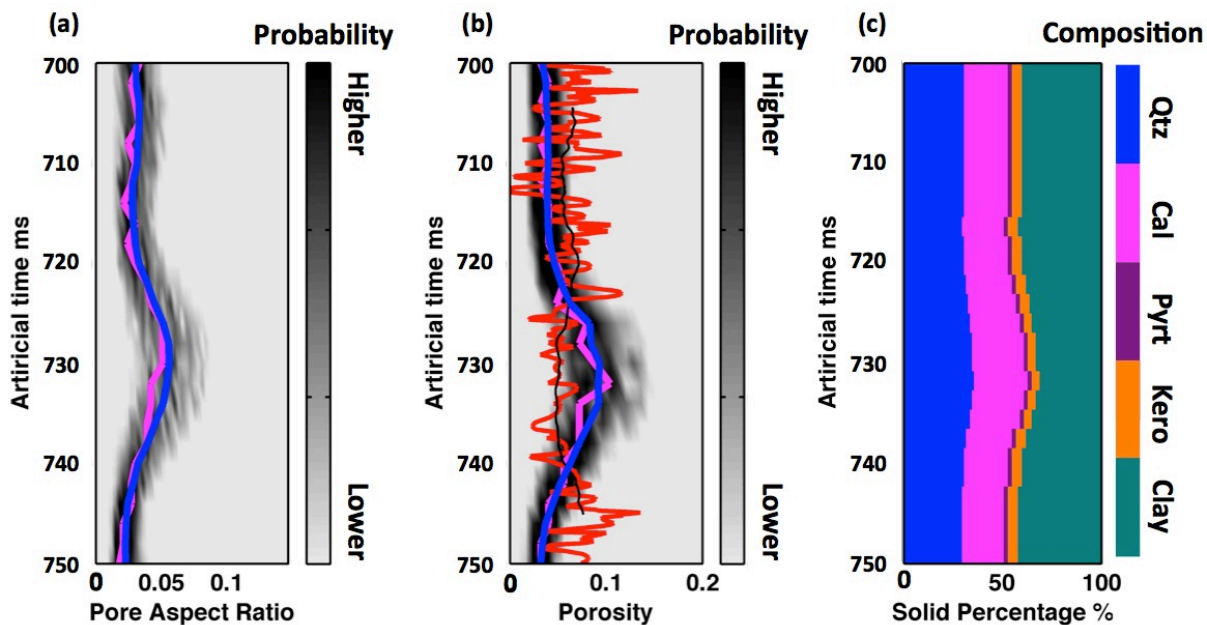
Figure 5.7: The rock property estimations at the seismic scale. At each time, 100 estimations of pore shape, porosity and composition were calculated. For the pore shape estimation (a) and porosity estimation (b), the background color represents probability, with darker color representing estimations with higher probability, and lighter color representing estimations with lower probability. The magenta curve marks the estimation with the highest probability, and blue curve marks the mean value of the estimations. In the porosity estimation plot (b), red curve shows the density porosity from well log data, and black curve is a smoothed version of the red curve. (c) The composition estimation. Each time contains different percentages of quartz, calcite, pyrite, kerogen and clay.
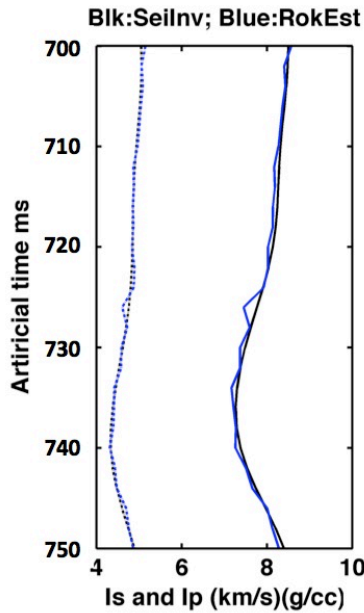
Figure 5.8: Validation of the estimated rock properties. Black solid and dashed curves are the P- and S-impedances from seismic inversion, and blue solid and dashed curves are the P- and S-impedances derived from the mean values of the estimated rock properties (Figure 5.7).

5.5.2 A 2D Slice Example

Figure 5.9 shows a 2D section of the inverted P-impedance (Figure 5.9a), S-impedance (Figure 5.9b) and *Vp/Vs* (Figure 5.9c) in the Haynesville Shale. The seismic profile is marked by the black line in Figure 2.5, with Well A (inline 1166) in the middle of the seismic profile. The hot colors indicate large values, and cold colors indicate small values. Spatial variability is clearly present in each section. Vertically, each inverted parameter shows a decrease at the base of the Haynesville Shale between about 720 ms and 740 ms. The color intensity changes among different inlines. These variations should be related to rock properties, such as porosity, pore-shape distribution and composition.
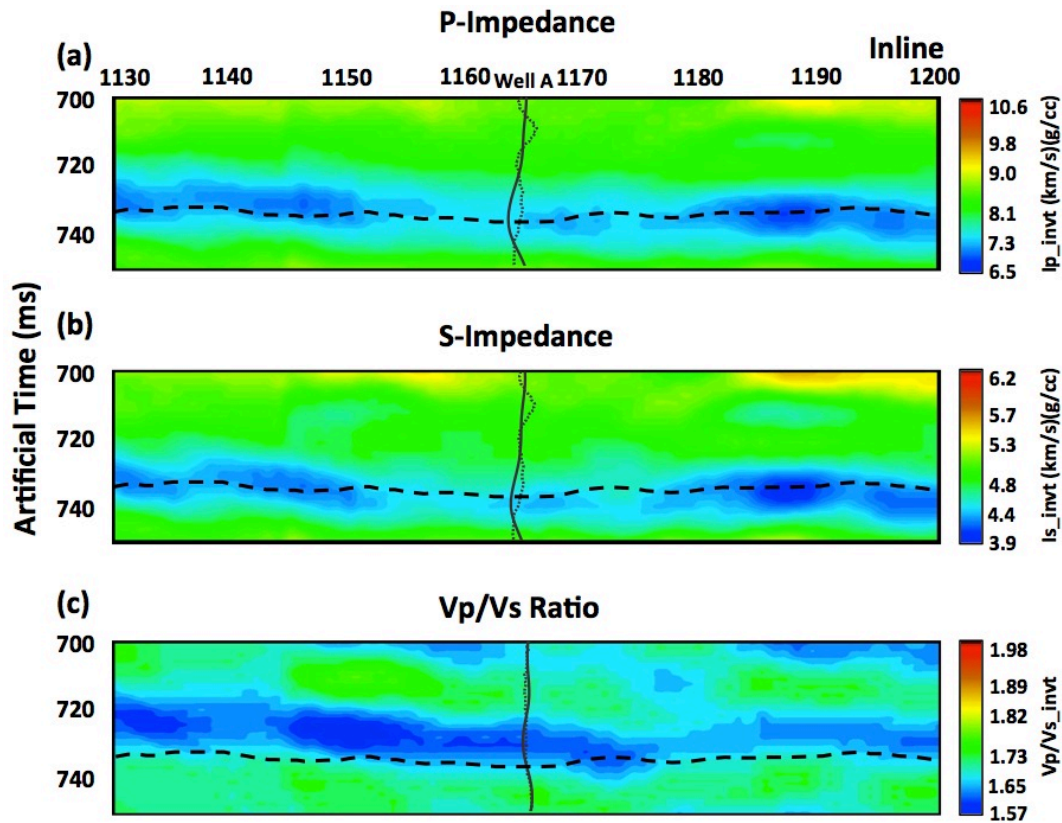
Figure 5.9: The prestack seismic inverted P-impedance (a), S-impedance (b), and V_P/V_S (c) within the Haynesville Shale, based on the bandpass filtered and angle stacks. The insert solid curve shows the inverted results at Well A, and dotted curve shows the corresponding smoothed log at Well A. The cold colors indicate lower values and hot colors indicate higher values. Each of the inverted elastic properties varies both vertically and laterally. They all show a decrease at the bottom of the Haynesville Shale between about 720 ms and 740 ms. The horizontal dashed curve shows the horizon for the map views in Figures 5.16–5.19. The horizon is an approximate 90 degrees shift up from the original horizon picked from the post-stack amplitude data (Figure 2.6).

The estimated porosity (Figure 5.10a) varies vertically and laterally. Within the Haynesville Shale, the porosity varies from about 2.3% to 11.1%, with an average of about 5.5%. Vertically, the porosity is larger between about 720 ms and 740 ms than the other time ranges. This relatively larger porosity is consistent with the low P- and S-

impedances observed from the inversion result at the same time range. The porosity is smaller on the top and very bottom of the Haynesville Shale, which is consistent with the large inverted P-impedance values at the top and very bottom of the Haynesville Shale. Laterally, the color intensity of the porosity estimation varies at different locations. For example, between about 720 ms and 740 ms, the porosity has large values between inline 1130 and 1140, at inline 1150, 1170, and 1200, and small values at 1140 and 1180. In fact, the porosity affects both P- and S-impedances. Generally, large porosity corresponds to low P- and S-impedances and vice versa. The relative standard deviation (Figure 5.10b) is about 20% to 25%.
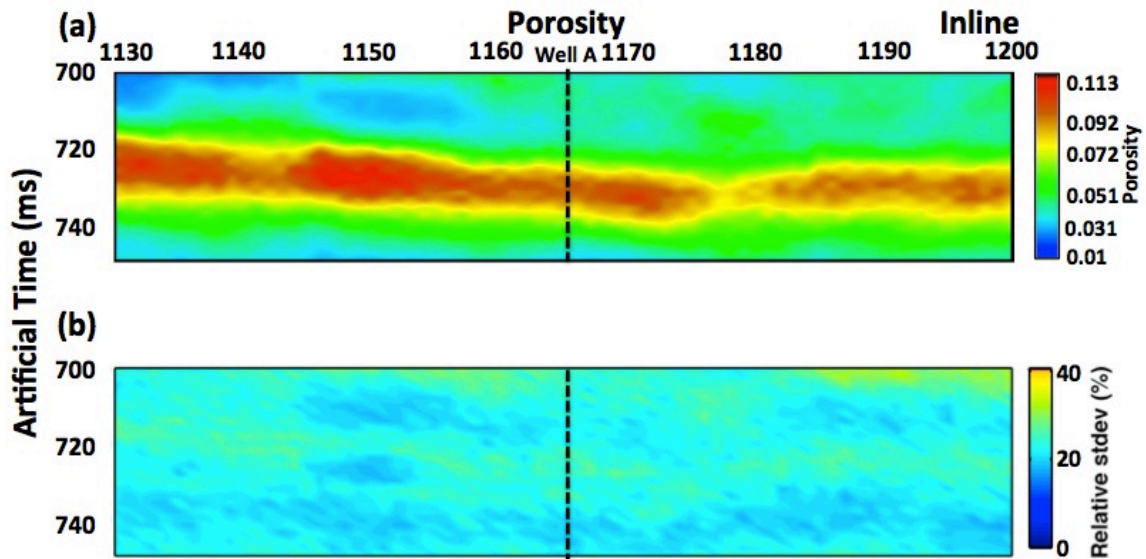
Figure 5.10: a) Porosity estimation. The hot colors indicate large values, and cold colors indicate smaller values. The porosity estimation is negatively correlated with P-impedance and S-impedance. b) Relative standard deviation of the porosity estimation, showing the estimation uncertainty. The black dashed line indicates Well A.

The pore-shape distribution represents the range of pore aspect ratios. Similar to porosity, the pore-shape distribution also varies vertically and laterally (Figure 5.11). The pore aspect ratio varies from about 0.02 to 0.07, with an average of about 0.04 in the seismic profile. These variations correlated negatively with the V_P/V_S (Figure 5.9c): higher aspect ratios correspond to lower V_P/V_S, and vice versa. In particular, between about 720 ms and 740 ms, the hot spots in the pore-shape distribution between inline 1130 and 1140, at inline 1150, 1170, and 1200 correspond to the cold spots in the V_P/V_S (Figure 5.9c), respectively. Similar to porosity estimation, the relative standard deviations (Figure 5.11b) of the pore-shape distribution is about 20%.

The estimations of composition include fractions of clay, quartz, calcite, and kerogen. Clay fraction estimation (Figure 5.12) and quartz fraction estimation (Figure 5.13) are shown as examples. The clay varies from 29% to 44% with an average of about 39%, and quartz varies from 28% to 37% with an average of about 31%. Similar to the pore-shape distribution, the clay and quartz fraction distributions appear to be correlated with V_P/V_S. More clay corresponds to larger V_P/V_S, and less clay corresponds to smaller V_P/V_S. More quartz corresponds to smaller V_P/V_S, and less quartz corresponds to larger V_P/V_S. The relationship between clay and V_P/V_S is consistent with the fact that clay has higher V_P/V_S than the other minerals in the Haynesville Shale. Similarly, the relationship between quartz and V_P/V_S is consistent with the fact that quartz has lower V_P/V_S than the other minerals in the Haynesville Shale. The relative standard deviations for the composition estimation are very small (Figure 5.12b and Figure 5.13b).

118
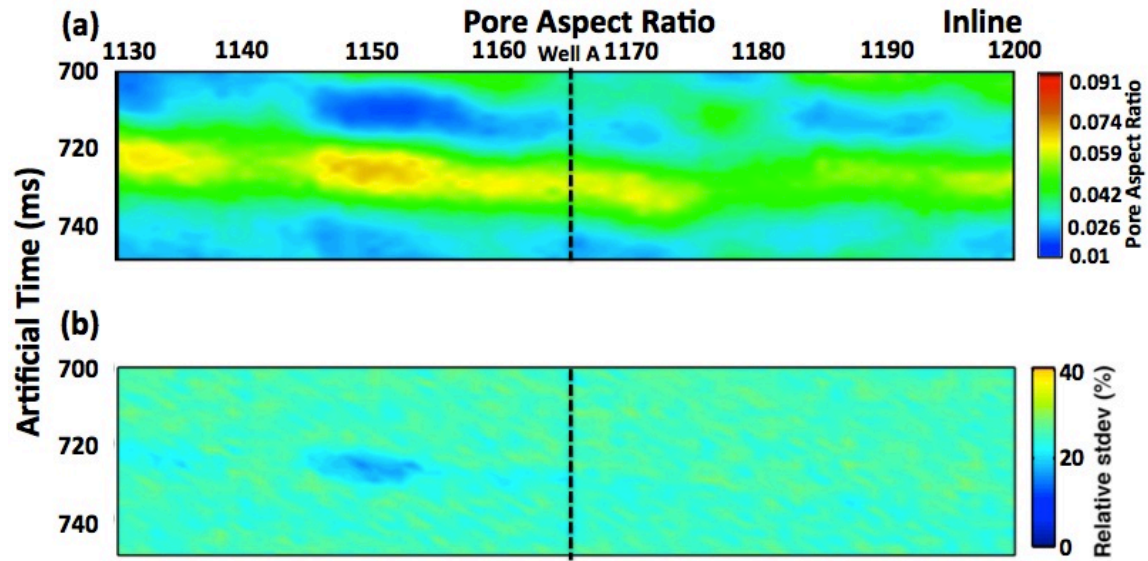
Figure 5.11: a) Pore-shape distribution estimation. The hot colors indicate large values, and cold colors indicate smaller values. The pore-shape distribution is negatively correlated with V_P/V_S. b) Relative standard deviation of the pore shape estimation, showing the estimation uncertainty. The black dashed line indicates Well A.
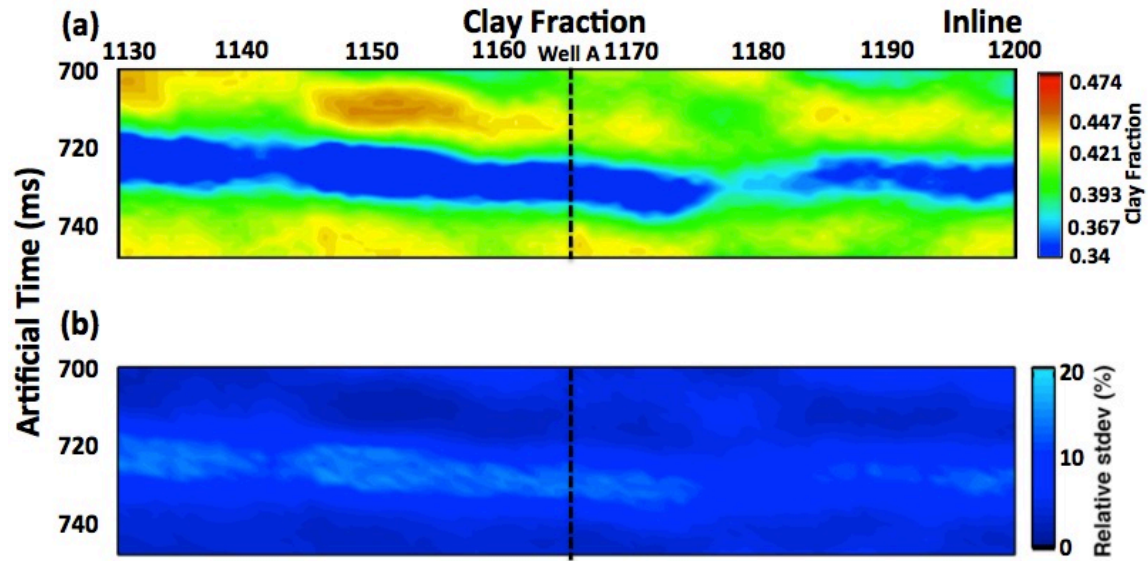
Figure 5.12: a) Clay fraction estimation. The hot colors indicate large values, and cold colors indicate smaller values. The clay fraction is correlated with V_P/V_S. b) Relative standard deviation of the clay fraction estimation, showing the estimation uncertainty. The black dashed line indicates Well A.
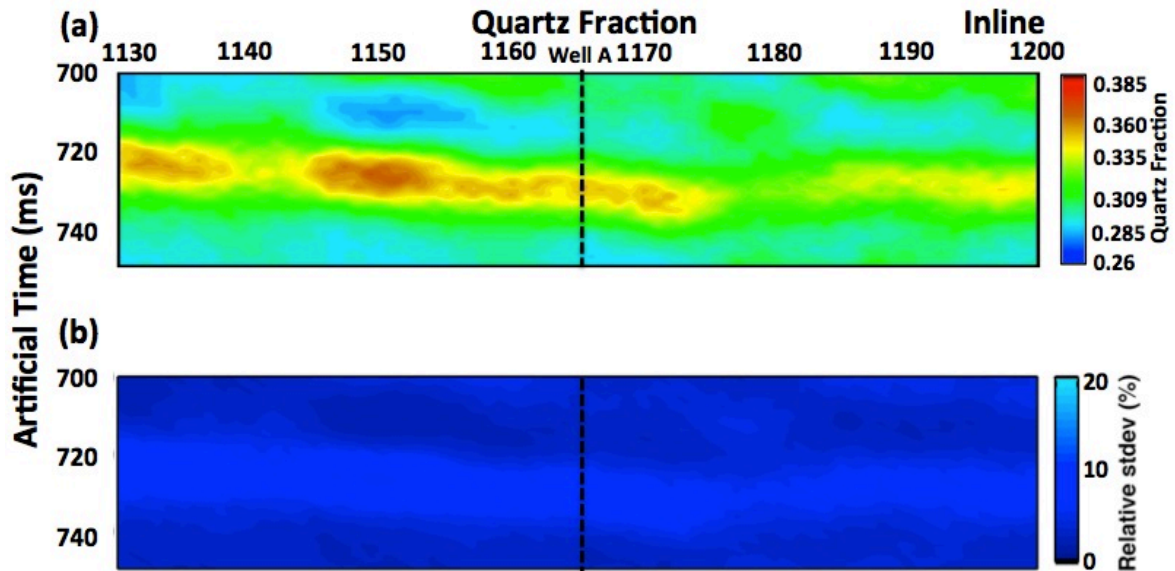
Figure 5.13: a) Quartz fraction estimation. The hot colors indicate large values, and cold colors indicate smaller values. The quartz fraction is correlated with V_P/V_S. b) Relative standard deviation of the quartz fraction estimation, showing the estimation uncertainty. The black dashed line indicates Well A.

After estimating the continuous rock properties at the seismic scale, further analysis validated the results. Figure 5.14 shows the comparison of P-impedance. The rock-property derived P-impedances are very similar to the inverted P-impedances, with average differences less than 4%. Figure 5.15 shows the comparison of S-impedances, with average difference between rock property derived one and inverted one less than 3%. These similarities indicate that the estimated rock properties are valid.
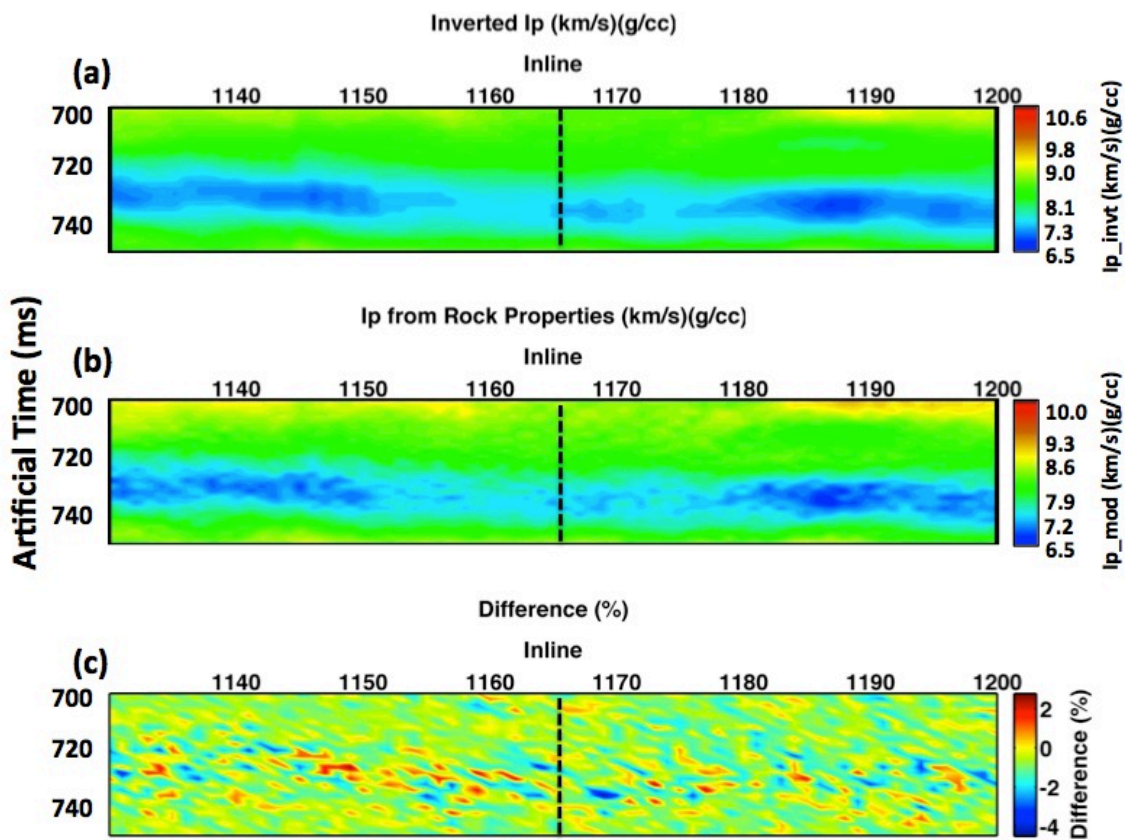
Figure 5.14: Validation of the estimated rock properties. a) The P-impedance from seismic inversion. b) The P-impedance derived from estimated rock properties. c) The difference between the two P-impedances, which is mostly less than 4%. The black dashed line indicates Well A.
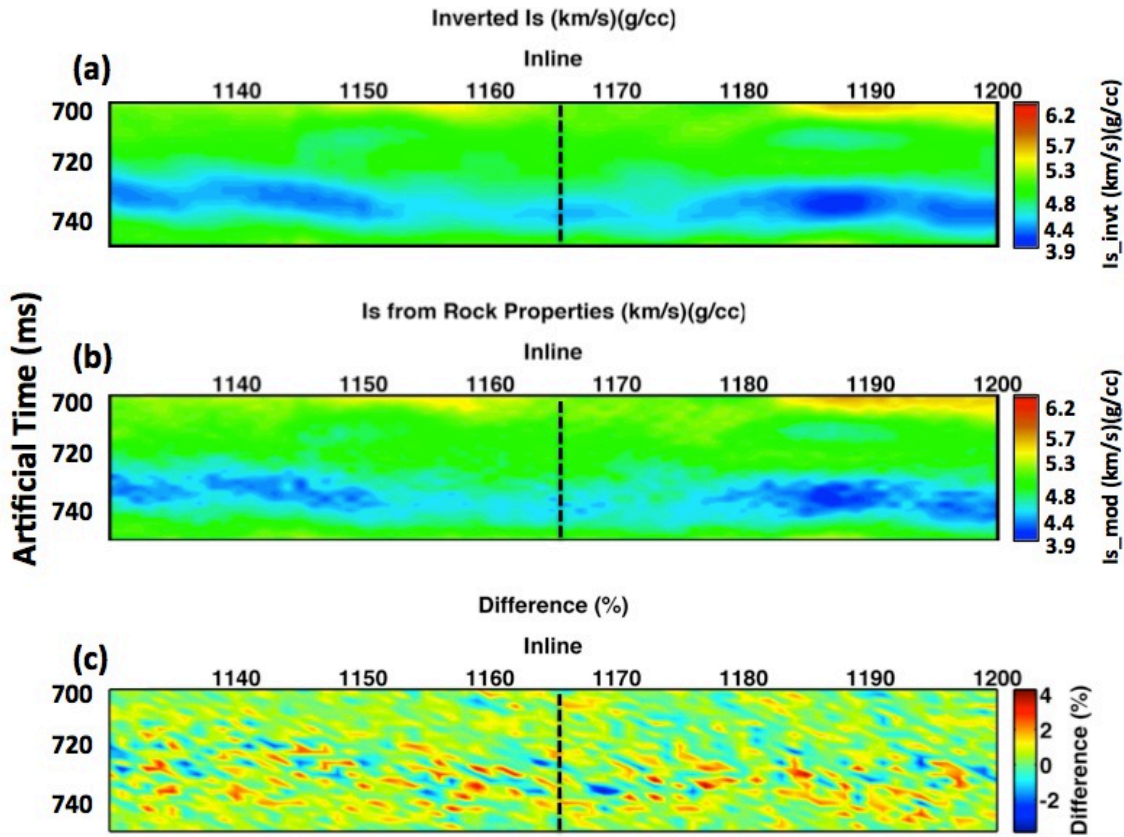
Figure 5.15: Validation of the estimated rock properties. a) The S-impedance from seismic inversion. b) The S-impedance derived from estimated rock properties. c) The difference between the two S-impedances, which is mostly less than 3%. The black dashed line indicates Well A.

5.5.3 Application on 3D Volume

The same procedure of rock-physics modeling, prestack seismic inversion and grid searching was applied to the 3D volume. The seismic scale rock properties were obtained for the 3D volume and were correlated with the elastic properties. Figure 5.16 shows the prestack seismic inverted P-impedance (Figure 5.16a), S-impedance (Figure 5.16b) and V_P/V_S (Figure 5.16c) for the horizon at the base of the Haynesville Shale (black dashed curve in Figure 5.9). Well A is in the middle of the map view (inline 1166,

crossline 2184). In each panel, the hot colors represent large amplitudes, and cold colors represent small amplitudes. P- and S-impedances show similar spatial variation pattern. In the north area, P- and S-impedances are relatively small, and in the southeast area, P- and S-impedances are relatively large. The V_P/V_S also show spatial variation, whereas the variation pattern is different from P- and S-impedances.

The estimated porosities, pore shape distribution, quartz fractions and clay fractions from the same horizon are shown in Figure 5.17. In each panel, the hot colors represent higher values and cold colors represent smaller values. These rock properties are all correlated with the P- and S-impedances and V_P/V_S. The porosity estimation (Figure 5.17a) is relatively high at the north area and low at the southeast areas. These spatially variation patterns in porosity are negatively correlated with the ones in P- and S-impedances. Similarly, the pore shape distribution and quartz fraction is negatively correlated with V_P/V_S, and the clay fraction is positively correlated with the V_P/V_S.

The elastic properties derived from the estimated rock properties from the horizon are shown in Figure 5.18. Those elastic properties are very similar to the inverted elastic properties in Figure 5.16. Furthermore, the residuals between the rock-property derived elastic properties and the seismic-inverted elastic properties are all close to zero (Figure 5.19). The similarities between the two sets of elastic properties indicate that the estimated rock properties are valid.
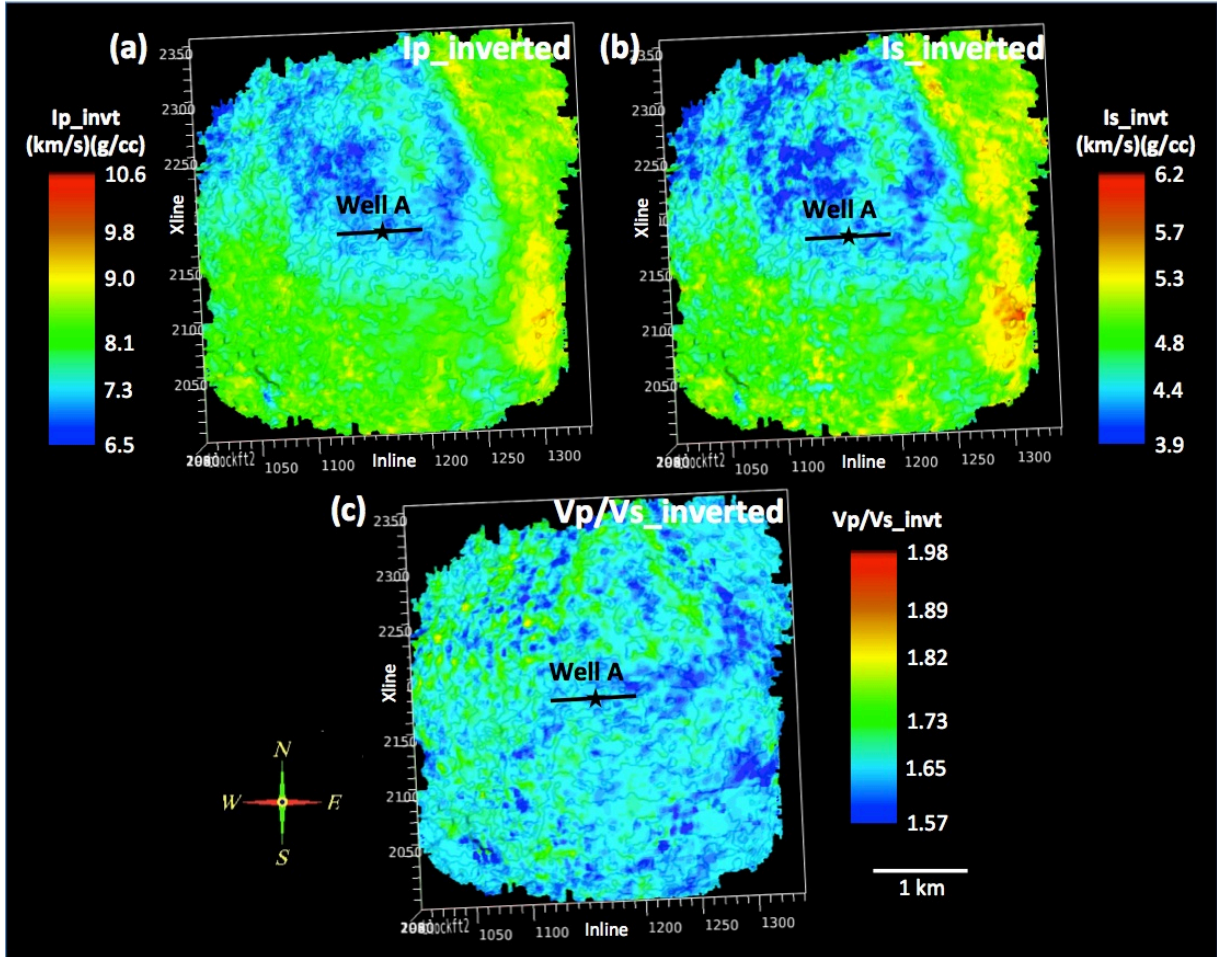
Figure 5.16: A map view showing the prestack inverted P-impedance (a), S-impedance (b) and V_P/V_S (c) for the horizon at the base of the Haynesville Shale (black dashed curve in Figure 5.9). In each panel, the hot colors represent large amplitudes, and cold colors represent small amplitudes. Both the inverted P- and S-impedances show low amplitudes in the north area and large amplitudes in the southeast area. The V_P/V_S shows spatial variation, but the patterns are not necessarily the same as shown from P- or S-impedance map. The black line marks the 2D profile shown in Figures 5.9–5.15.
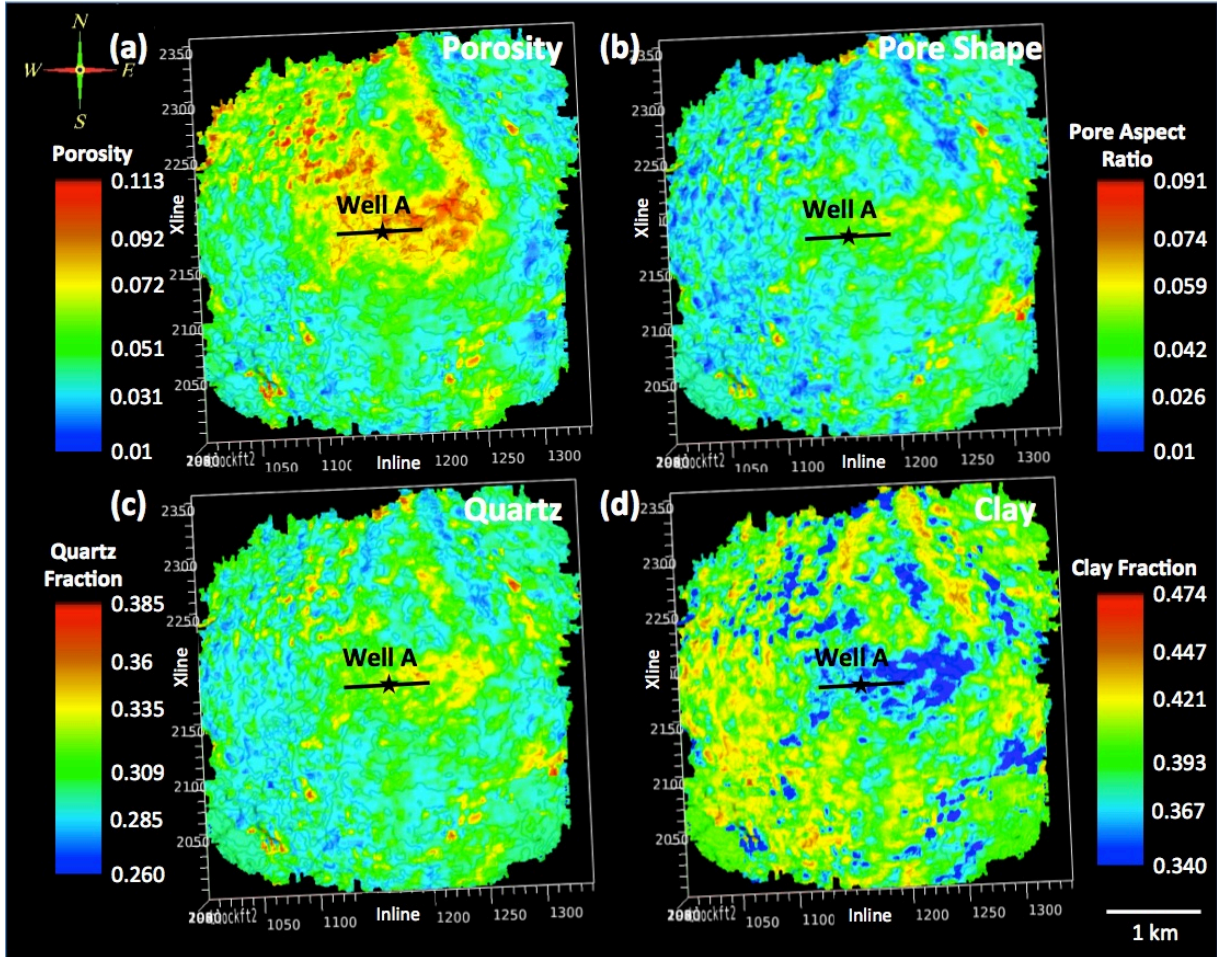
Figure 5.17: The estimated rock properties. In each panel, the hot colors indicate large values, and cold colors indicate smaller values. Those rock properties are all correlated to the elastic properties shown in Figure 5.16. (a) Porosity estimation, which is generally negatively correlated with P-impedance and S-impedance. (b) Pore-shape distribution estimation, which is negatively correlated with V_P/V_S. (c) Quartz fraction estimation, which is negatively correlated with V_P/V_S. (d) Clay fraction estimation, which is positively correlated with V_P/V_S. The black line marks the 2D profile shown in Figures 5.9–5.15.
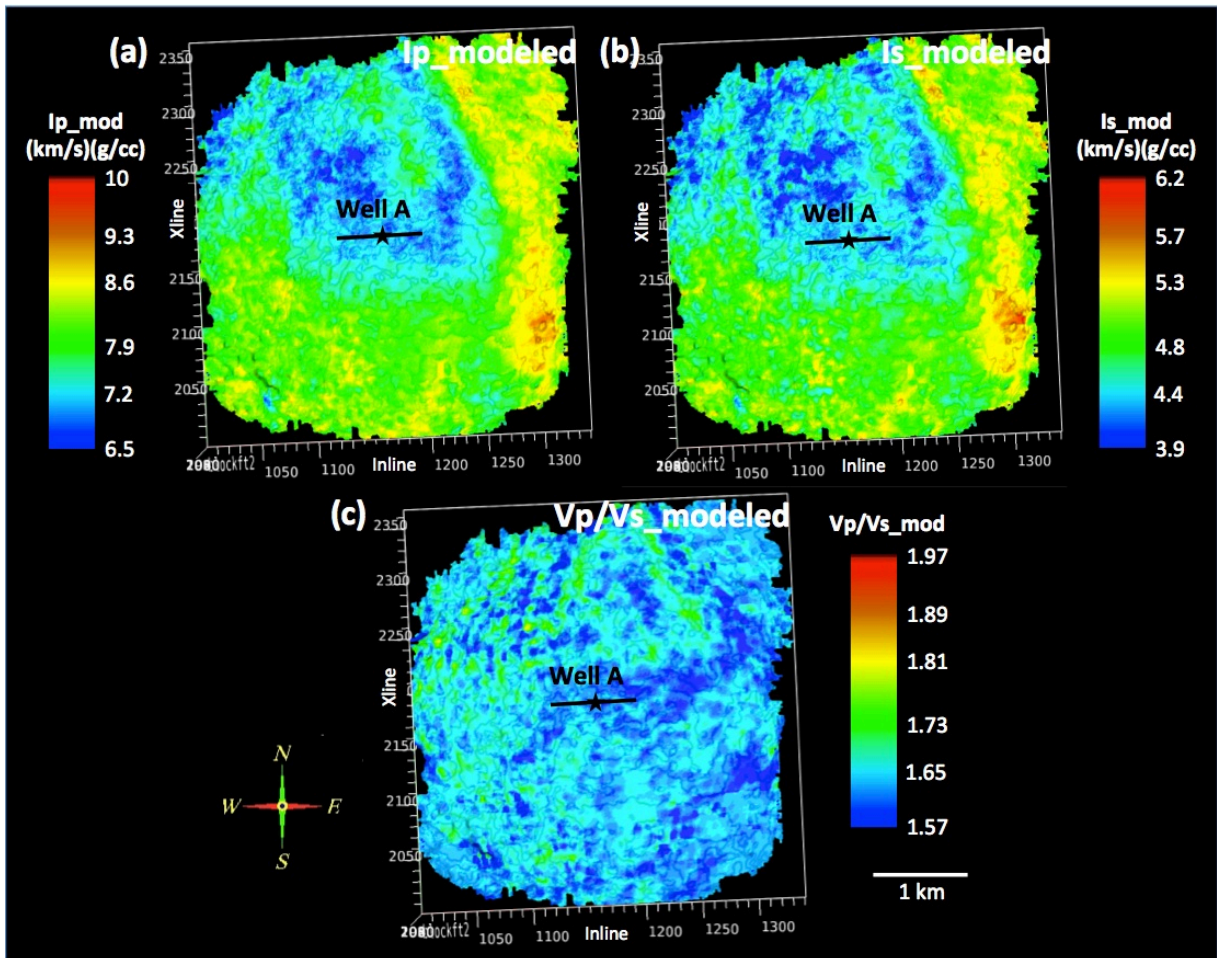
Figure 5.18: A map view showing the P-impedance (a), S-impedance (b) and V_P/V_S (c) derived from the estimated rock properties from Figure 5.17 for the horizon at the base of the Haynesville Shale (black dashed curve in Figure 5.9). In each panel, the hot colors represent large amplitudes and cold colors represent small amplitudes. These elastic properties are very similar to the ones inverted from seismic data (Figure 5.16). The colorbar scale is slightly different from Figure 5.16 due to the software (Landmark) performance. The black line marks the 2D profile shown in Figures 5.9–5.15.
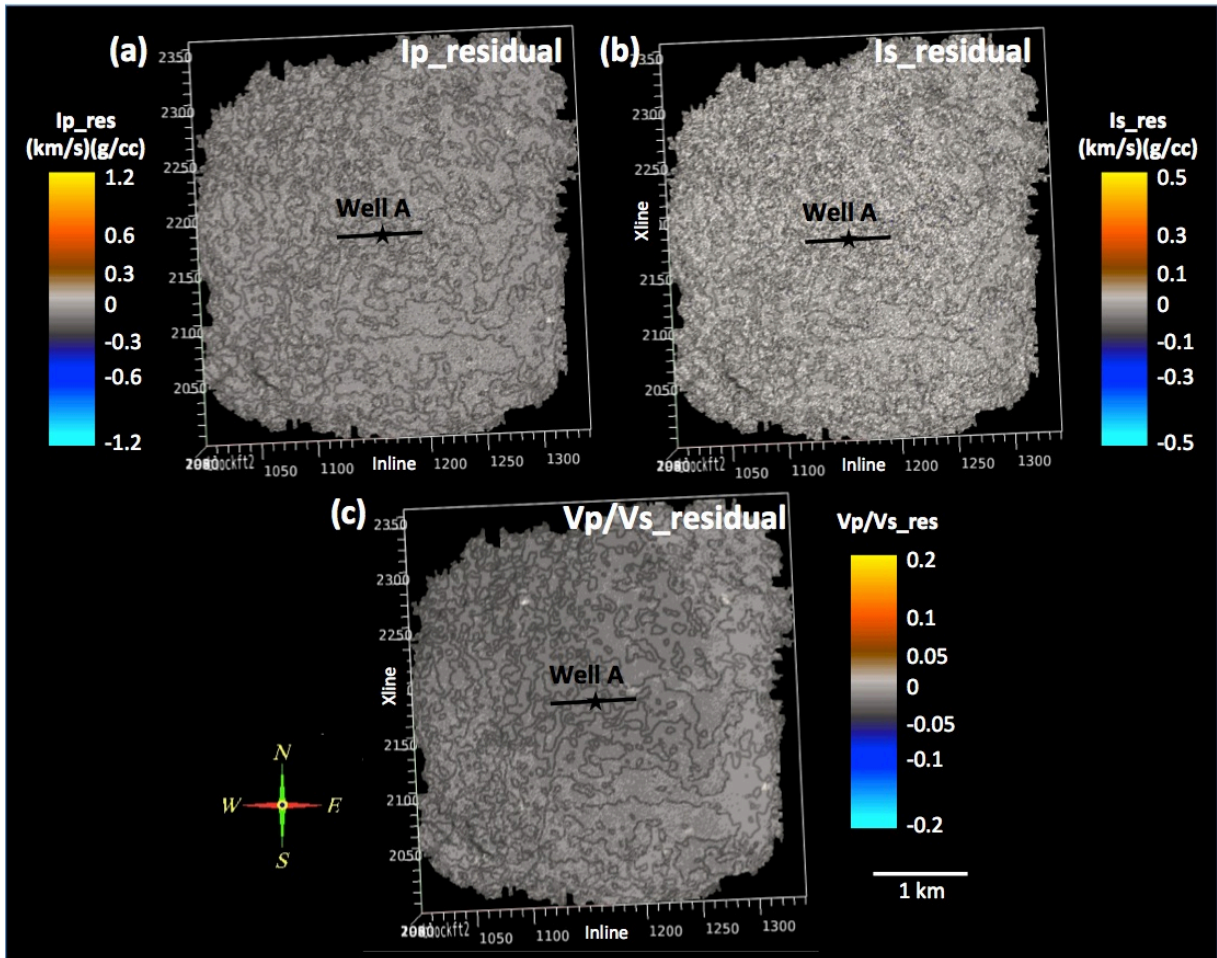
Figure 5.19: A map view showing showing the residual of P-impedance (a), S-impedance (b) and V_P/V_S (c) for the horizon at the base of the Haynesville Shale (black dashed curve in Figure 5.9). Those residuals are the difference between the rock-property derived elastic properties and the seismic-inverted elastic properties.

5.6 DISCUSSION

The rock properties were estimated at the seismic scale, and they were correlated with the seismic amplitude variations. Some correlations are explicit, which include the negative correlation between porosity and P- and S-impedances, the negative correlation between quartz fraction and V_P/V_S, the positive correlation between clay fraction and V_P/V_S, the positive correlation between pore shape and quartz fraction, and the negative correlation between pore shape and clay fraction. Some correlations are implicit, e.g., the relationship between composition and impedances, and the relationship between the pore shape and impedances. The rock property estimation result shows low clay fraction and high quartz fraction between about 720 ms and 740 ms (Figure 5.12 and 5.13), whereas P- and S-impedances are low between the same time range (Figure 5.9). In map view, the rock property estimation result shows low clay fraction and high quartz fraction in the south area and the north-south strip between inline 1200 and 1300 (Figure 5.17), whereas P- and S-impedances are low in the same areas (Figure 5.16). These relationships seem contrary to the normal case that stiffer quartz matrix has a higher impedance and softer clay matrix has a lower impedance. In fact, the porosity in the Haynesville Shale is mostly interparticle and sits in between stiffer mineral grains (i.e., quartz and calcite) instead of clay platelets (Figure 2.16b, Chalmers et al., 2012). Accordingly, the estimated porosity is higher where the quartz fraction is higher (and clay fraction is lower), and vice versa. The higher porosity generates the lower P- and S-impedances. Similarly, once the above relationship between composition and porosity is taken into account, the presented relationship between pore-shape distribution and impedances would not be difficult to

129

interpret. The explicit and implicit relationships between the rock properties and elastic properties imply that the rock properties need to be investigated simultaneously when interpreting the seismic attribute variations. These interpretations also rely on the prior distributions of the correlations between them and the weight that has been put on for P- and S-impedances during the rock-physics modeling.

In the seismic reservoir characterization workflow presented here, there are three major parts: rock-physics modeling, seismic inversion, and grid searching. Each of these affects the characterization accuracy. The rock-physics model accounted for the anisotropy of shales and was calibrated in Jiang and Spikes (2013a), generating good results at the log scale. The grid searching results depend on the objective function (equation 5.1). On the one hand, if the maximum values for Obj_P and Obj_S were too small, then the constraint would be too harsh. On the other hand, if the maximum values for Obj_P and Obj_S were too large, then there would be almost no constraint, and the estimated rock properties would be quite random. The objective function used in this chapther was the L_1 norm, and other types of objective function might provide different estimations of the rock properties.

The accuracy of seismic inversion is very important. If the elastic properties were not inverted correctly, then the estimated rock properties would also be inaccurate, and it would be difficult to correlate the rock properties with the observed seismic attributes. For the Haynesville Shale case, the impedance contrast at the bottom is very large and steep (about 40% increase in about 10 m), due to the formation change from shale to limestone. Therefore, it is difficult to obtain an accurate inversion result at the bottom of

the Hayneville Shale. In addition, the seismic-inversion algorithm is isotropic, whereas the rock-physics modeling is anisotropic. On the one hand, it is difficult to perform anisotropic seismic inversion with a lack of anisotropy measurements at both the log scale and laboratory scale. On the other hand, theoretically, the anisotropic features would mainly be related to the far offset signals in the seismic data, whereas in our case, the data quality is poor in the far offset (Figure 5.3). Therefore, isotropic seismic inversion was performed in this study. Anisotropic seismic inversion could be performed if there were anisotropy measurements, and the seismic data quality at far offset was better.

The study combines rock-physics modeling with seismic inversion. During these two processes, different types of velocities are mixed. The rock-physics model calculates phase velocities, and the well log data is close to phase velocity because it was acquired in a vertical well perpendicular to bedding. However, the seismic data does not provide phase velocity. The recorded seismic data typically corresponds to group velocity, and the seismic-derived velocities are a geometric type of velocity that is composed of some type of NMO velocity with some VTI residual. For anisotropic media, such as the Haynesville Shale, the group velocity has different value from the phase velocity. The phase velocity (V_{phase}) is calculated from the rock-physics derived stiffness tensor components and the phase angle (θ). The group velocity (V_{group}) can be calculated from phase velocity (Tsvankin, 2012), indicated as

$$V_{Gx} = V_{phase} \sin\theta + \frac{\partial V_{phase}}{\partial \theta} \cos\theta$$

$$V_{Gz} = V_{phase} \cos\theta - \frac{\partial V_{phase}}{\partial \theta} \sin\theta$$

$$V_{group} = \sqrt{V_{Gx}^2 + V_{Gz}^2}$$

$$\text{,} \qquad (5.2)$$

and the group angle (ϕ) can be calculated from phase angle (θ) (Thomsen, 1986) using

$$\tan(\phi) = \frac{V_{phase} \sin\theta + \dfrac{\partial V_{phase}}{\partial \theta} \cos\theta}{V_{phase} \cos\theta - \dfrac{\partial V_{phase}}{\partial \theta} \sin\theta}. \qquad (5.3)$$

We observed the difference between the phase velocity and group velocity for a model that contains compositions similar to core-measured results from Well A and with total porosity of 5% that is close to the average porosity of the Haynesville Shale (Figure 5.20). The phase velocity and group velocity for V_P, V_{SH} and V_{SV} were all calculated with phase angle varying from 0° to 90°. For this particular case, the group velocities were slightly larger than the phase velocities away from the symmetry planes. Also, the group angle (ϕ) and phase angle (θ) are very close (Figure 5.21). Similarly, the impedances generated from the group velocities were slightly larger than the impedances generated from the phase velocities at non-zero and non-ninety degrees. These differences were smaller than the comparison values of the objective function in the grid searching (equation 5.1) and were not able to be distinguished. Therefore, mixing phase and group velocities in our case does not have an adverse effect.
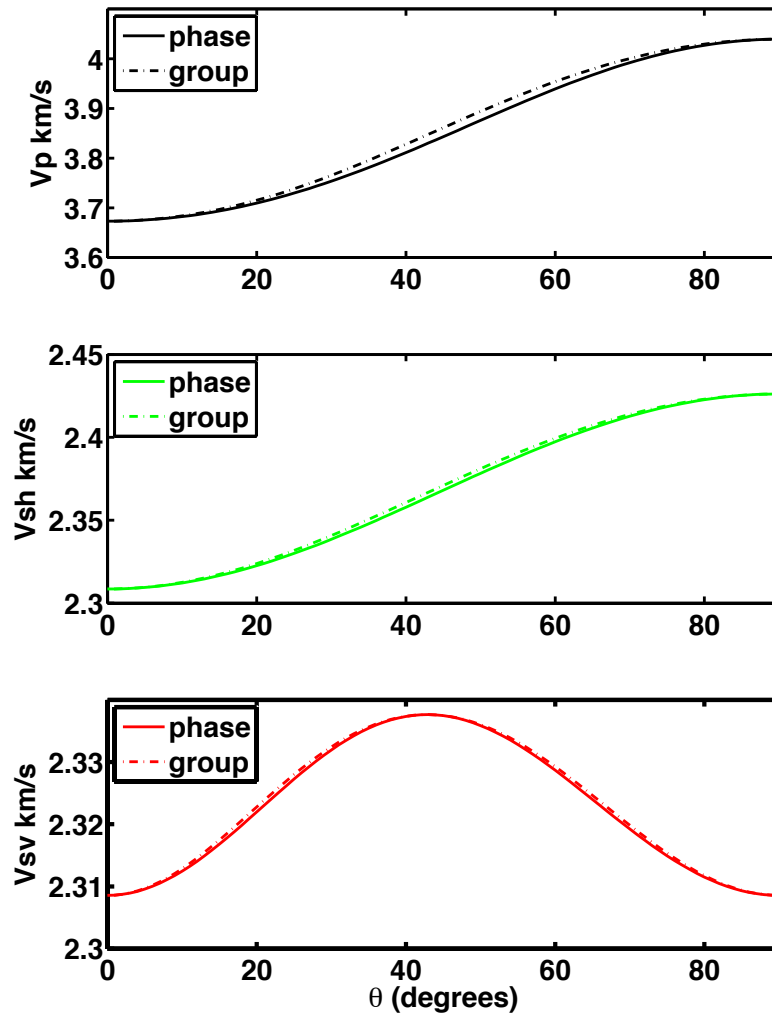
Figure 5.20: Phase velocities and group velocities for V_P (upper), V_{SH} (middle) and V_{SV} (lower) for a model. In the model, the composition includes quartz, calcite, kerogen and clay with percentages similar to core-measured results for Well A. The total porosity was set as 5%, which is close to the average values of the Haynesville Shale. The phase angle varies from 0° to 90°. The solid curves show phase velocities, and dashed curves show group velocities.

133
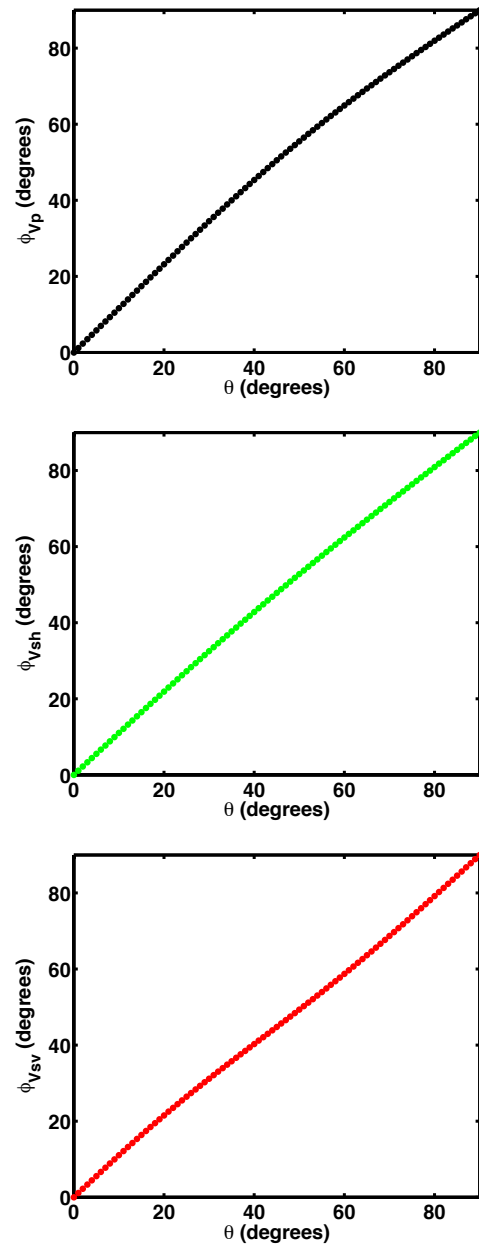
Figure 5.21: Phase angles and group angles for V_P (upper), V_{SH} (middle) and V_{SV} (lower) for a model. In the model, the composition includes quartz, calcite, kerogen and clay with percentages similar to core-measured results for Well A. The total porosity was set as 5%, which is close to the average values of the Haynesville Shale. The group angles are very close to phase angles.

To verify the reliability of estimated rock properties, the P- and S-impedances derived from the rock properties and the ones from inversion results were compared. Furthermore, synthetic seismic traces can be generated from the two sets of impedances, and those two sets of synthetic seismic traces can be compared with the observed seismic traces. Because the Haynesville Shale itself is only about 50 ms in two way travel time, it is too thin to generate reliable synthetic seismic traces given that the dominant frequency is about 25 Hz. Although the further validation step may not be applicable for the Haynesville Shale, it would be a good approach for other shales that are thicker than the Haynesville Shale or for other datasets that have higher frequency seismic data.

5.7 CONCLUSION

In this chapter, rock properties were estimated at the seismic scale through rock-physics modeling, grid searching, and prestack seismic inversion. Different distributions of the rock properties helped to interpret the seismic amplitude variations. All these rock properties affect the seismic velocities, and their effects on the seismic amplitude were investigated simultaneously. Generally, the P- and S-impedances are negatively related to porosity, and V_P/V_S is positively related to clay fraction distribution, and negatively related to pore shape and quartz fraction distributions. Based on the estimated rock properties, it is suggested to do hydraulic fracturing in areas with higher porosity, larger pore aspect ratio, more quartz, and less clay.

The seismic reservoir characterization procedure for the Haynesville Shale presented in this chapter considered the complex mineral and pore phases, as well as

135

anisotropy. Each step (rock-physics modeling, prestack seismic inversion and grid searching) in the workflow affected the accuracy of the rock property estimations, so it was important to validate the estimations. The characterization helped to interpret the correlations between the seismic amplitude variations and the rock properties. The same seismic reservoir characterization procedure could be applied to other unconventional gas shales.

Chapter 6: Conclusions and future work

6.1 CONCLUSIONS

In this dissertation, the relationships between the rock properties and elastic properties of the Haynesville Shale were investigated. The combination of the self-consistent model and Chapman's model represented both P- and S-wave velocities or P- and S-impedances. A workflow was built to estimate the rock properties based on rock-physics modeling, prestack seismic inversion and grid searching. Those rock properties were correlated with the seismic data amplitude variations.

The result from Chapter 3 indicated that in addition to porosity, the pore shape and composition also have significant effects on the elastic properties of the Haynesville Shale. We showed how the trends in velocity measurements corresponding to joint variations of composition and pore shape in the Haynesville Shale could be modeled using an effective-medium model. In general, larger porosity, softer composition, and smaller pore aspect ratios correspond to lower seismic velocities. The investigated relationships between the rock properties and elastic properties of the Haynesville Shale provided guidance for estimating the rock properties in Chapter 4.

In Chapter 4, porosity, composition and pore shape for the Haynesville Shale were estimated from our workflow that combined an isotropic and an anisotropic effective medium model with a grid-search method. The rock-physics models were calibrated using well log data and core measurements, and they explained both P- and S-wave velocities. The rock properties inverted from this workflow were compared to the ones from well log data or core measurements. The estimated porosity was very close to

the density porosity, in terms of both the variation trend within the Haynesville Shale and the measured values. The estimated composition contained very similar average percents of quartz, calcite, clay, pyrite and kerogen to the ones from core measurements. The pore shape estimation suggested that the pores, cracks, and fractures within the Haynesville Shale have elongated shapes, which generally matched from the current observations from the microstructure images. The rock-physics modeling assumed a constant fluid (25% water and 75% gas) in the entire Haynesville Shale formation. In fact, the fluid affects both the density and bulk modulus of rocks. Given that the porosity for the Haynesville Shale is small (about 5% on average), the assumption of constant fluid was valid. The fluid effect may need to be considered when applying the workflow to other plays. Nonetheless, this workflow was also a very important step for interpreting the spatial variations of the seismic attributes in Chapter 5.

Chapter 5 applied the workflow from Chapter 4 to the seismic reservoir characterization of the Haynesville Shale. The procedure was performed on a 2D section, and also on a full 3D volume of seismic data. P- and S-impedances were inverted from prestack seismic data and were subsequently input into the workflow to estimate the rock properties at seismic scale. Each step (rock-physics modeling, prestack seismic inversion and grid searching) in the procedure affected the accuracy of the estimations. These estimated rock properties were correlated with the seismic amplitude data. All the above rock properties (porosity, composition, and pore shape) affected the seismic velocities, and their combined effects on the seismic amplitude helped to interpret the seismic attribute spatial variations. The P- and S-impedances correlated negatively with porosity,

138

and the V_P/V_S correlated positively with clay fraction and negatively with the pore-shape distribution and quartz fraction. These rock properties were validated through the comparisons between the elastic properties derived from the estimated rock properties and the ones inverted from the prestack seismic data. The differences between the two sets of elastic properties were less than a few percent.

The main contributions of this dissertation include multiple aspects. First, in the rock-physics modeling, both P- and S-wave velocities (and P- and S-impedances) were simultaneously calibrated, while most of the previous studies only focused on P-wave data. Therefore, our process provided two independent pieces of known information in the problem of inverting multiple rock properties. This additional information from S-wave data helped to reduce the non-uniqueness in the rock-property inversion. Second, an inverse calculation of the rock-physics modeling (grid searching) was developed to estimate the rock properties at both well log scale and seismic scale. This inverse calculation provided distributions of porosity, pore shape and composition for sonic logs at each depth and for seismic-inverted impedances at each time and location. Those estimated rock properties provided useful information in determining locations with relatively high porosities and relatively large fractions of brittle components favorable for hydraulic fracturing. The rock properties also helped to interpret the spatial variations observed from the seismic data. Third, a wide range of scales, including the seismic scale, well log scale and lab scale (microstructure images), were considered in this dissertation. These scales were linked together to interpret the rock property estimations and seismic data observations.

6.2 FUTURE WORK

In this dissertation, the rock-physics modeling accounted for anisotropy of the Haynesville Shale through aligned fractures. However, the anisotropy of shales comes from alignment of clay platelets and/or alignment of pores, cracks or fractures. Including the orientation of clay platelets would make the rock-physics modeling more representative of shales. Although the rock-physics modeling was anisotropic, the seismic-inversion algorithm was isotropic. Due to the far offset data quality and the lack of anisotropy measurements at both the log scale and laboratory scale, it was difficult to perform anisotropic seismic inversion. Performing anisotropic seismic inversion with such constraints would make the workflow more comprehensive. When combining the rock-physics modeling and seismic inversion, we chose zero incidence angle for the rock-physics modeled velocities. We also chose zero incidence angle for the seismic-inverted velocities because we did isotropic seismic inversion. However, when anisotropy is taken into account at both well log scale and seismic scale, the incidence angles of the seismic-inverted velocities will be difficult to determine. Therefore, it is challenging to resolve the incidence angle for the rock-physics modeled velocities at the seismic scale. The choice of the angle-dependent rock-physics modeled velocities would be a very good future research direction.

Appendix A: Composition of Well A from XRD (Abundance in volume percent) and Core Analysis

Courtesy Dr. Ursula Hammes

Artificial Depth (m)	quartz	feldspar	plag	calcite	dolomite	pyrite	kerogen	total clay
2293	28.7	0.7	5.4	3.5	0.6	2.1	0.9	57.9
2296	33.7	0	5.9	2.3	1	3.2	1.7	52.2
2299	28.7	0.7	5.2	4.4	0.6	1.6	0.9	57.8
2302	25.4	1	5.3	4.2	0.6	1.4	0.7	61.4
2305	26.1	0.6	4.3	3.6	0.8	2.1	1	61.5
2308	28.4	0	5.8	3.3	0.7	1.1	1	59.8
2311	30.9	0	6.1	3.9	1.2	1.1	1	55.8
2314	31.2	0	5.4	4.5	2.3	2.2	1	53.4
2317	29.7	0	5.8	6.1	1.4	2.3	1.1	53.6
2321	32.3	0	6	7.1	1.3	2	2.1	49.2
2323	28.2	0	6.7	5.3	1	2.3	1	55.5
2327	29.6	0	6.5	3.3	1.5	2.4	1.2	55.5
2329	26.3	0.7	5.2	5.1	1.4	2	1.2	58.1
2333	28	0.8	5.1	5.1	1	1.6	0.8	57.5
2336	32.1	0	6.3	6.3	2	2.1	1.3	49.8
2339	28.2	0.7	5.7	3.4	0.5	1.2	0.7	59.6
2342	29.2	0	6.2	6.7	1.1	2.5	1.6	52.6
2345	28.1	0	4.4	5.3	0.5	1.6	1	59.1
2348	26.6	0	5.6	6.1	1.6	2.6	1.3	56.4
2351	26.2	0	6.3	6.7	1	2.3	1.8	55.7
2354	33.6	0	8.1	10.2	1.1	1.6	1.7	43.8
2357	35.8	0	7.2	4.7	0.6	3.6	2.7	45.6
2360	37.4	0	10.6	15.9	1.6	1.4	4.5	28.6
2363	40.4	0	8.1	6.8	0	2.8	5	36.8
2366	34.6	0.8	9.5	22.1	0	2.1	4.3	26.6
2368	12.8	0	5.3	26.5	40.2	1.9	2.8	10.4
2372	30.2	0	7.8	21.9	1.4	2.2	6.7	29.7
2375	36.6	0	8.1	10.2	0.4	1.9	6.9	35.8
2378	33.2	0.4	8.2	18.2	0.7	1.7	6.6	31
2381	21.8	0	8	31.2	3.2	1.7	4.8	29.2
2384	32.3	0	8.2	13	0	1.8	6	38.8
2387	31.3	0	8.6	10.8	0	3	7.1	39.2

2390	34.8	0.6	8.7	11	0.3	1.9	6.4	36.4
2393	34.1	0	7.6	15.3	0.8	2.4	4.5	35.4
2396	34.6	0	8.6	14.7	1.1	1.9	5.2	34
2399	33.8	0	6.8	6.9	0	1.6	4.8	46.2
2402	24.4	0	7	31.2	2.9	1.9	6.6	26
2405	36	0.8	8.1	12.3	0.4	2.3	6.7	33.4
2408	36.6	0.8	7.5	8	0.6	2.1	5.4	39
2412	38.1	0.5	9.7	9	0.6	1.7	5.9	34.4
2414	30	0.7	7.8	21	1.3	1.5	6.4	31.4
2418	33.8	0.7	6.8	7.3	0	2.1	4.5	44.8
2420	31.1	0	8.5	10.4	0.3	1.6	6.4	41.7
2423	32.5	0	7.4	9.6	1	1.5	4.3	43.7
2426	32.7	0	8.2	6	0.2	2.5	4.3	46.2
2430	16.6	0	5.5	12.3	29.1	1.1	4.1	31.2
2433	23.9	1	6.8	22.4	2	1.1	5.8	36.9
2435	33.8	0	7.7	8.6	0	1.8	6.2	41.8

Appendix B: Modeling the Haynesville Shale using Differentiate Effective Medium (DEM) model

The DEM models the effective moduli of the porous elastic materials by incrementally adding inclusions of one phase (phase 2) to the background phase (phase 1) (Figure B.1a). The matrix starts with only phase 1 as the background material, then phase 2 with a specified aspect ratio is added, and the effective medium of the new material is calculated as the new background material. The process is continued until phase 1 and 2 have the desired proportions.

In the DEM, the effective moduli of the elastic material depend on the way the host material is treated. Specifically, treating phase 1 as background material will result to different effective moduli as treating phase 2 as background material. In addition, given phase 1 as background material, the order in which phase 2 inclusions are added also affect the effective moduli (Figure B.1b).

I modeled the elastic properties in Well A and Well B using different compositions and pore shapes. The mineral and pore properties used in the modeling are shown in Table B.1.

Table B.1: Mineral and pore properties used in the modeling

Material	Quartz	Kerogen	Clay	Limestone	Pyrite	Pore
ρ (g/cc)	2.65	1.3	2.58	2.71	4.93	0.8
μ (Gpa)	45	2.7	7	33	132.5	0
K (Gpa)	36.6	2.9	18	69	147.4	1
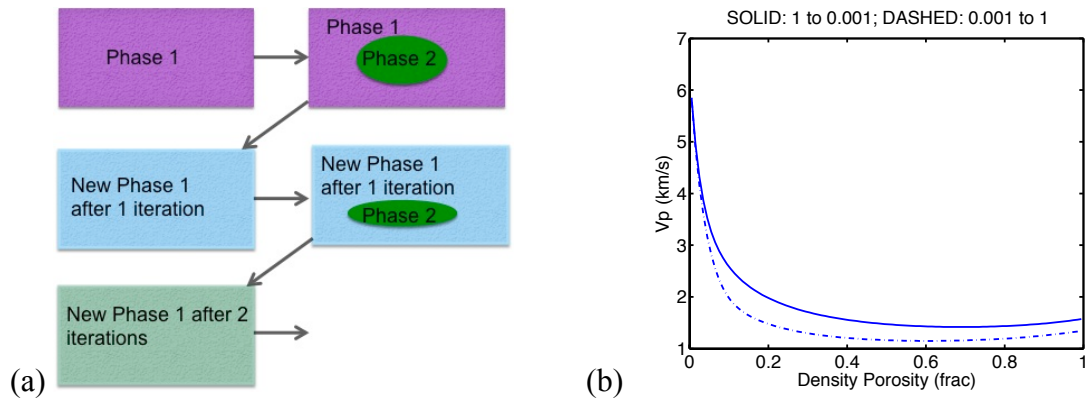
Figure B.1: (a) Illustration of the differential effective medium model. The rock with effective moduli is created through multiple steps. (b) The effect of adding phase 2 inclusions to phase 1 (limestone) in different orders. The phase 2 inclusions are 4 pores with aspect ratios of 0.001, 0.01, 0.1, and 1. The solid line represents adding the 4 pores in descending aspect ratio order; while the dashed line represents adding the 4 pores in ascending aspect ratio order.

Figure B.2 shows the result of modeling the pore-shape effect for Well A using the DEM. The colored lines are calculated using 50 pore inclusions whose aspect ratios were normally distributed as shown in Figure B.2a. The mineral phase was fixed as limestone, and the aspect ratio of mineral phase was 0.1. The lines with larger mean values of pore aspect ratios have higher V_P, because larger pore aspect ratios have greater stiffness. Within each line, V_P decreases as porosity increases, which is consistent with the trend from the data. The results show that the Haynesville Shale can be modeled using pores with aspect ratios in the range of 0.1–0.01, for a constant composition. In Figure B.2b, there are a group of solid and dashed lines, which can be clearly seen in Figure B.2c as a zoomed in view of Figure B.2b. The solid lines from DEM represent adding the pore inclusions in descending order in terms of aspect ratio. The dashed lines represent adding the pore inclusions in ascending order.

144
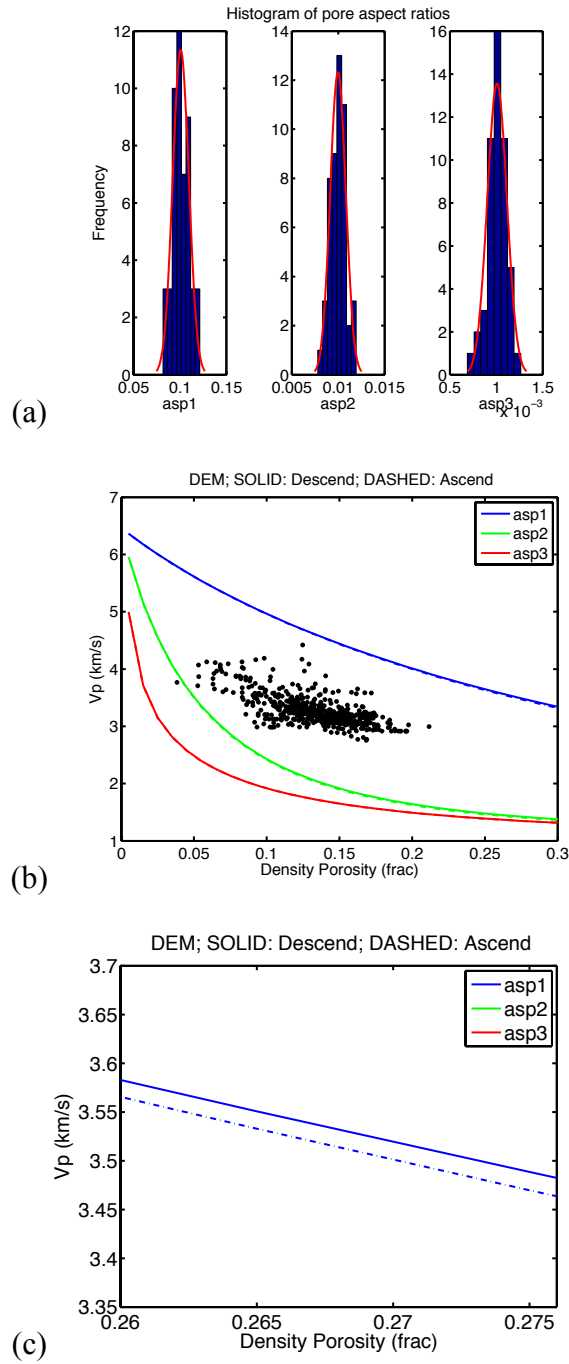
Figure B.2: (a) Histograms of the pore inclusions. (b) DEM results showing the pore-shape effect for Well A in the Haynesville Shale formation. (c) A zoomed in view of (b) showing the separation of solid and dashed lines.

145

Figure B.3 shows the result of modeling the composition effect for Well A using DEM. Five individual compositions were examined: pyrite, quartz, clay, limestone, and kerogen. Aspect ratios were 0.1 for clay, 0.01 for kerogen, and 1 for quartz, limestone, and pyrite. Aspect ratios for 50 pores were normally distributed as shown in Figure B.3a. For both models, along each line, V_P decreases as the porosity increases. As porosity increases, the lines converge, which implies that the composition effect on the velocity is more significant for rocks with lower porosities than rocks with higher porosities. The solid and dashed lines in Figure B.3b and B.3c illustrate the effect of the order in which the pore inclusions were added. Solid lines are from stiffest to softest, and dashed are in the reverse order.

In Figure B.4, different mineral combinations were examined using the DEM. For the matrix, the percentages of kerogen and pyrite are fixed as 7% and 1%; the percentages of limestone, quartz, and clay are varied. All the lines follow the trend shown in the data very well, which indicates that modeling lines from different composition combinations can explain the variation in the data.

Figure B.5 shows the DEM results for Well B, simultaneously varying both composition and pore shape effects. The data points are colored by gamma ray count. There is no clear trend between V_P and density, which might due to multiple reasons, such as various compositions, porosities, and fluid saturation. The lines from left to right represent porosity changes from 16.5% to 0.5%. Within each line, both composition and pore shape vary. The composition assemblage is 56% limestone with grain aspect ratio of 1, 3% kerogen with grain aspect ratio of 0.01, 4% pyrite with aspect ratio of 1, 10.5%

quartz on the bottom to 35% quartz on the top with grain aspect ratio of 1, and 26.5% clay on the bottom to 2% clay on the top with aspect ratio of 0.1. The pore aspect ratio varies from 0.005 on the bottom to 0.12 on the top. Each line is nearly vertical, which indicates that along each line, the modeling result does not depend on the density. From the data, the high gamma ray count data points correspond to velocity of about 3 km/s. For the modeling lines, the velocities for the high-clay content near the bottom of each line follow a decreasing trend from high density to low density, which is not consistent with the data.

The models presented here provide the ability to understand relationships between the reservoir and elastic properties. The purpose is not to model each data point individually. By representing trends in the data, these modeled relationships can be used to interpolate between and extrapolate to reservoir property combinations that are not present in the log data. These extended values are important to include in seismic inversion scenarios where geologic conditions might differ from what is observed at the well.

(a)
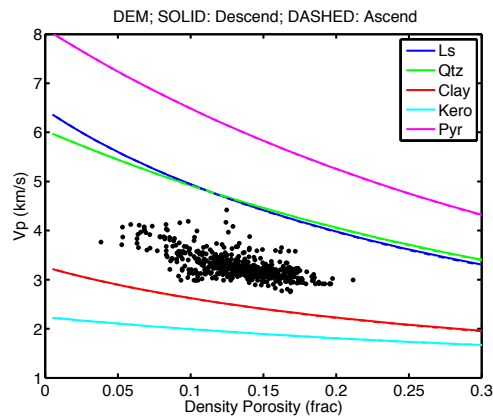
(b)
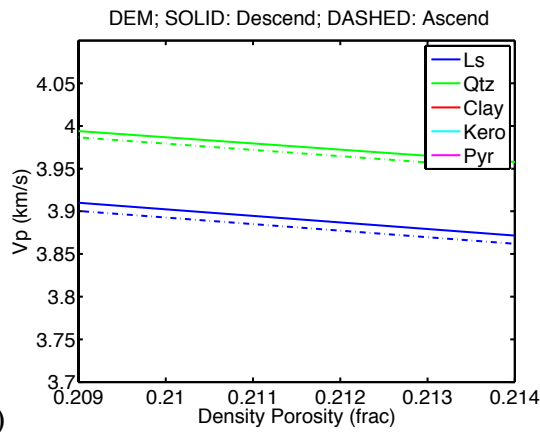
(c)

Figure B.3: (a) Histogram of pore inclusion aspect ratios used in both the DEM modeling. (b) The DEM result showing the composition effect for Well A in the Haynesville Shale formation. (c) A zoomed in view of (b) showing the separation of solid and dashed lines.
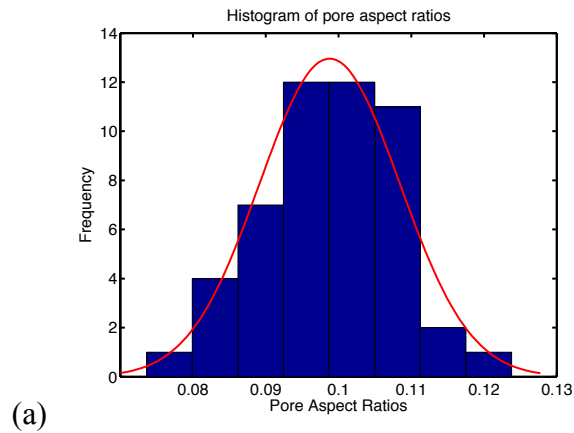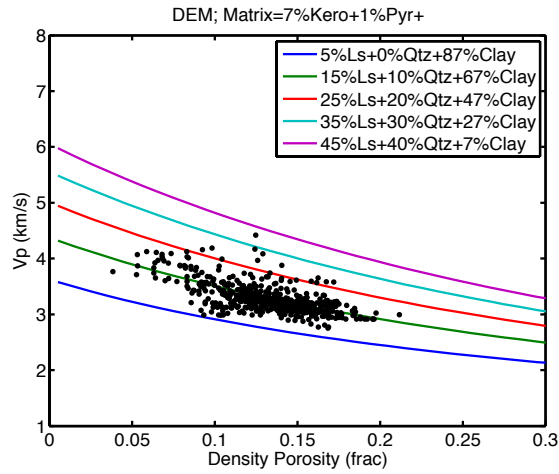
Figure B.4: The DEM result showing the different combinations of the five minerals.
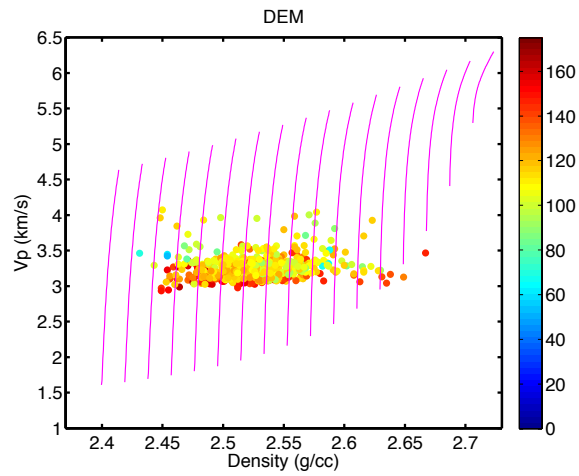
Figure B.5: The DEM result for Well B in the Haynesville Shale formation. Different lines represent results from different porosities, and within each line, both compositions and pore shapes are varied from bottom to top.

Appendix C: Using isotropic self-consistent model to estimate the porosity and pore aspect ratio of the Haynesville Shale

The self-consistent model is combined with a grid search method to estimate the porosity and pore aspect ratio distributions. In the grid search method, the solutions of the reservoir properties are obtained by systematically searching through each point in the decision space, which is modeled P-impedance (I_P). At each point, the objective function (absolute errors between the modeled and observed grid points) is evaluated. The point that provides the minimum value of the objective function corresponds to the best solution of the reservoir properties. In this work, we not only obtained the best solution, but also a probability distribution of multiple solutions.

Two algorithms were built in this work: one is for estimating porosity, and one is for estimating pore aspect ratio. The detailed procedure for estimating porosity is shown in Figure C.1. We first calibrated a specific SCM with a representative composition assemblage and pore aspect ratio distribution. Then 1000 porosity values that were uniformly distributed from 0 to 0.2 at each depth were input into the SCM. The resulting I_P values represented the decision space. After that, the observed I_P from the well was compared with the modeled I_P, and the absolute errors between them were calculated as the objective function. By evaluating the objective function, the porosity was estimated. The modeled I_P that provided the smallest absolute error corresponded to the best

solution of porosity, and the ones that provided larger absolute errors corresponded to

porosities with lower probabilities.
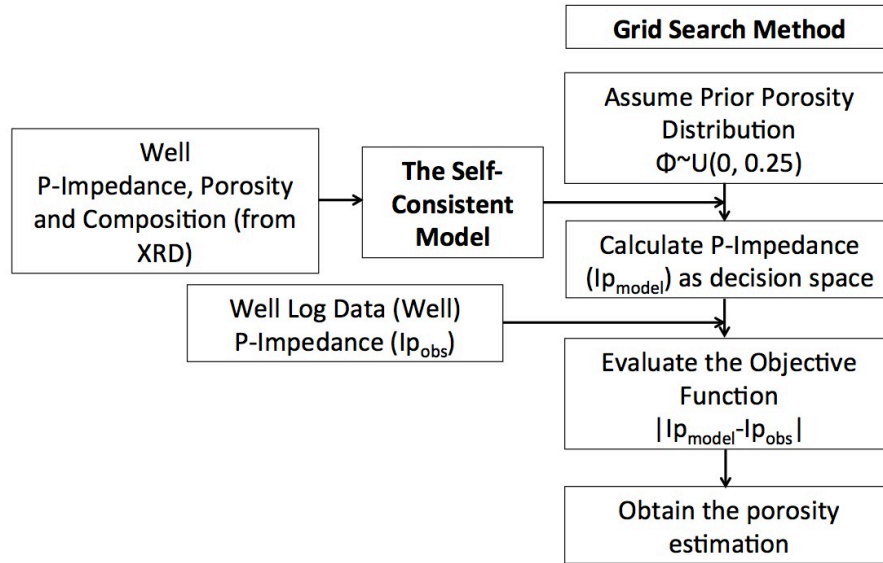
Figure C.1: Flowchart to estimate porosity. A uniform prior distribution of porosity was input into the specific SCM calibrated from the well to calculate the I_P in the decision space. Then the absolute error between the modeled and observed I_P was calculated as objective function. By evaluating the objective function, the distribution of porosity was estimated.

The flowchart of the algorithm used to estimate pore aspect ratio is shown in

Figure C.2. We first generated a group of SCMs that contained all the possible pore

aspect ratios from 0.001 to 1. Then distributions of porosity and I_P were estimated based

on the well log data. They were both normally distributed with mean values equal to the

observations. Then the assumed porosities and I_P were compared with the ones from the

SCMs. If the absolute errors between them were smaller than certain values (1e-3 for

porosity, and 1e-2 for I_P), the corresponding pore aspect ratios in the SCMs were

accepted. The whole process was repeated at each depth in order to estimate aspect ratio distribution for the whole Haynesville Shale formation, using data from Well A.

Repeat at Each Depth

Porosity (Φ) and P-impedance (Ip) distribution from data
$\Phi \sim N(\Phi_{obs}, 0.02^2)$; $Ip \sim N(Ip_{obs}, 0.1^2)$

SCMs with all possible Pore Aspect Ratios

$|\Phi - \Phi_{model}| <= 1e\text{-}3$
$|Ip - Ip_{model}| <= 1e\text{-}2$

Accept the corresponding Pore Aspect Ratio
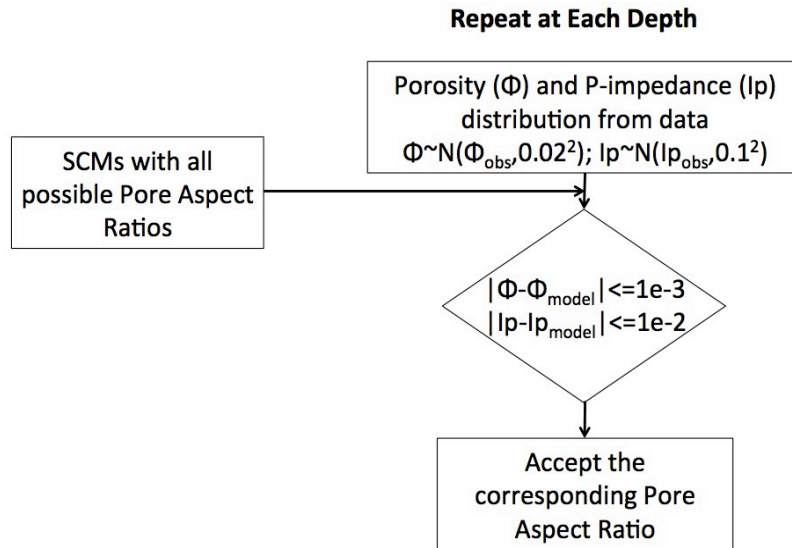
Figure C.2: Flowchart to estimate pore aspect ratio. The distributions of porosity and I_P based on the log data were compared with the ones from the group of SCMs with all possible pore aspect ratios. If porosities and I_P satisfied the specific criteria, the corresponding pore aspect ratios were accepted.

Based on the analysis of the composition and pore aspect ratio effects on I_P, as well as composition based on core analysis and XRD measurements, we obtained a SCM with a specific composition assemblage and pore aspect ratio distribution (Figure C.3). The composition assemblage included 37% clay, 33% quartz, 14% limestone, 8% plagioclase, 5% kerogen, 2% pyrite, 0.8% dolomite, and 0.2% feldspar; the pore aspect ratios were normally distributed with mean value 0.05 and standard deviation 0.01. In the crossplot of I_P and porosity (Figure C.3a), the I_P approximation (blue line) follows the

152

overall trend of the data. In Figure C.3b, the I_P approximation (blue curve) matches with the observed I_P (black curve) in terms of both overall trend and amplitude. The difference between the observed and modeled I_P is mostly around zero, with an average of about 7%. This indicates that the SCM with the specific composition assemblage and pore aspect ratio distribution effectively represents the data from the well.

To perform the grid search, 1000 porosity values were uniformly distributed between 0 and 0.2 at about 600 depth locations ($\sim$ 91 m sampled at 0.15 m). This number (1000) of porosity values at each depth is enough to keep high accuracy but low computational cost. The upper limit (0.2) was selected as about 30% larger than the maximum observed value. Values above 0.2 were assumed unlikely to occur. The modeled I_P from the SCM, calibrated from the well, was then calculated at every point in the grid. The absolute error between this modeled I_P and observed I_P (Figure C.4a) was calculated in the objective function. At each depth, the modeled I_P with the smallest error corresponded to the best solution of porosity. The I_P with larger errors corresponded to porosity solutions with smaller possibilities (Figure C.4b). In Figure C.4b, the color is the error in the porosity estimation from the grid search, the green curve is the best solution of porosity, and the black curve is the observed porosity. The estimated porosity generally fits the observed porosity in terms of both overall trend and amplitudes. The misfit of porosity is primarily due to using only one composition assemblage.

(a)

(b)
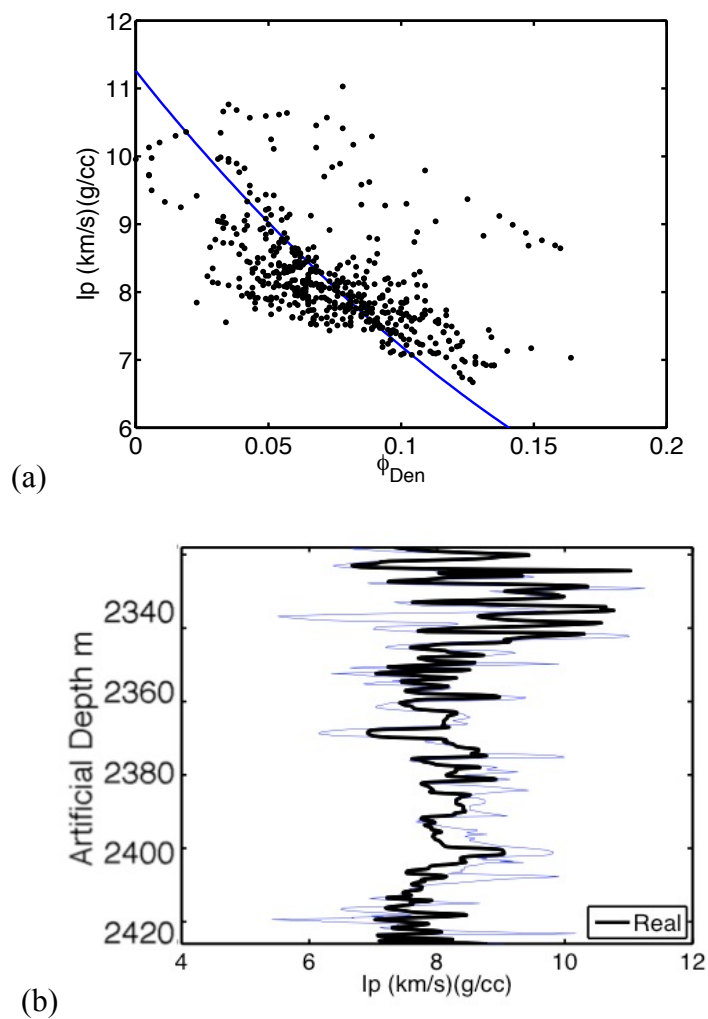
Figure C.3: (a) Cross plot of I_P versus porosity for the well. Black points are from well log data. The blue line is the SCM approximation with pore aspect ratio ~ N(0.05, 0.01^2), and composition assemblage of 37% clay, 33% quartz, 14% limestone, 8% plagioclase, 5% kerogen, 2% pyrite, 0.8% dolomite, and 0.2% feldspar. (b) I_P from well log data (black curve) and the SCM approximation (blue curve).

Estimation of pore aspect ratios includes generating a group of SCMs that contains all possible aspect ratios, assuming input porosity and I_P distributions from observed well log data, and evaluating the differences between the input and modeled porosities and I_P. Both the input porosity (Figure C.5a) and I_P (Figure C.5b) were normally distributed with mean values equal to the observed values at each depth. Figure C.6a shows the group of SCMs that contained all the possible aspect ratios from 0.001 to 1, with an increment of 0.001. The composition assemblage was the same as the one from Figure C.3. As the composition assemblage is fixed, the modeled I_P depends on porosity and pore aspect ratio. Therefore, by using the I_P and porosity from log data, we can obtain the corresponding pore aspect ratio. The estimation for the pore aspect ratio is shown in Figure C.6b. Most of the pore aspect ratios are about 0.05. We are not able to verify the pore aspect ratio estimation at every location. However, microstructure images from core samples provide useful information. By looking at the pore shapes from SEM images, we will be able to obtain an average pore aspect ratio at specific locations, and therefore get constraint on our estimation.

The workflows presented here estimated porosity and pore shape distribution separately by using P-impedance. Similarly, the relationship between S-impedance and porosity and pore shape (Figure C.7) could be included to add one more constrain. If both P- and S-impedances can be modeled by the rock-physics modeling, the porosity and pore shape distribution can be estimated simultaneously.

(a)

(b)
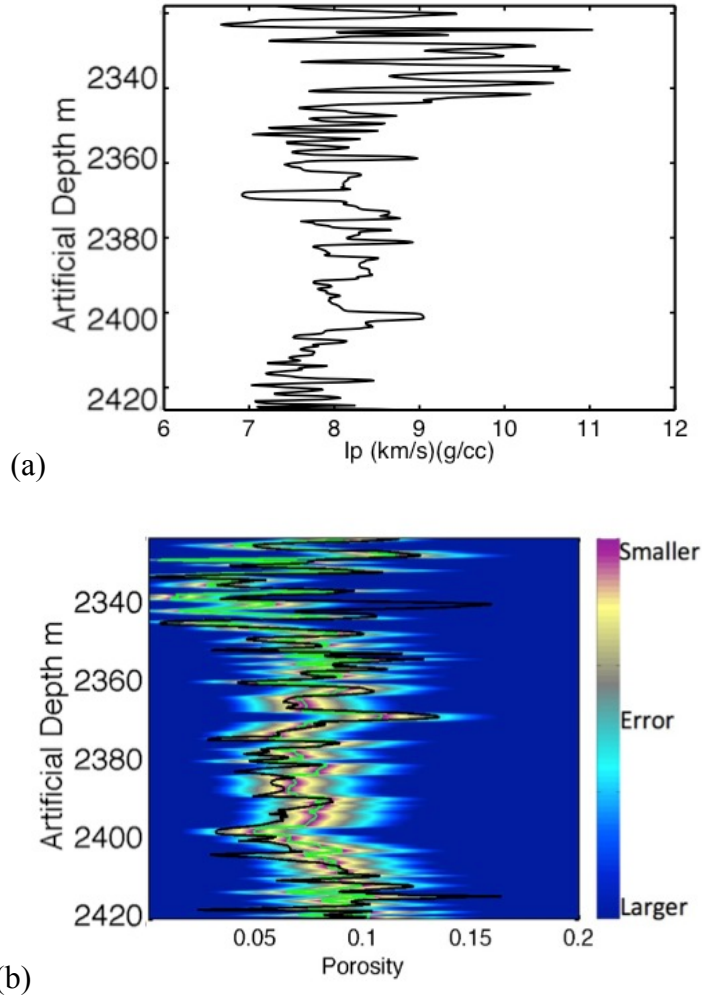
Figure C.4: (a) Observed I_P from the well. (b) Porosity estimations. Hot colors represent porosity with smaller error, and cold colors represent porosity with larger error. The solid black curve is the observed porosity, and the green curve is the estimated porosity with smallest error.

(a)

(b)
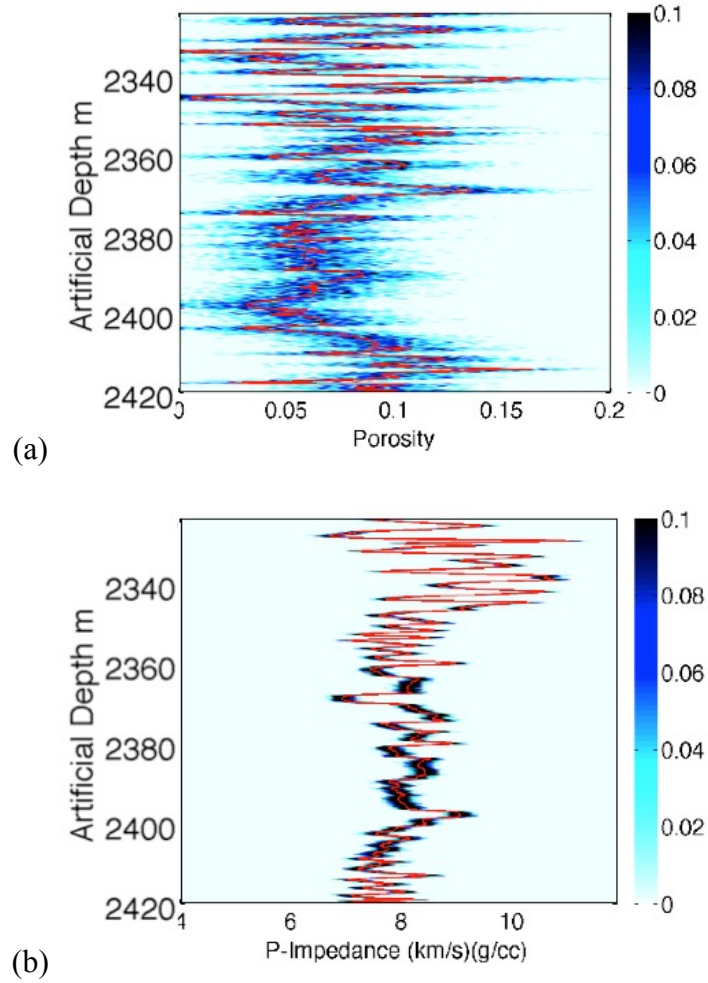
Figure C.5: (a) The input porosity distributions within the Haynesville Shale formation. The black curve is the observed porosity. At each depth, porosity was normally distributed with mean value equal to the observed porosity. Background color shows probability. (b) The input I_P distribution, plotted in the same way as in a).

(a)

(b)
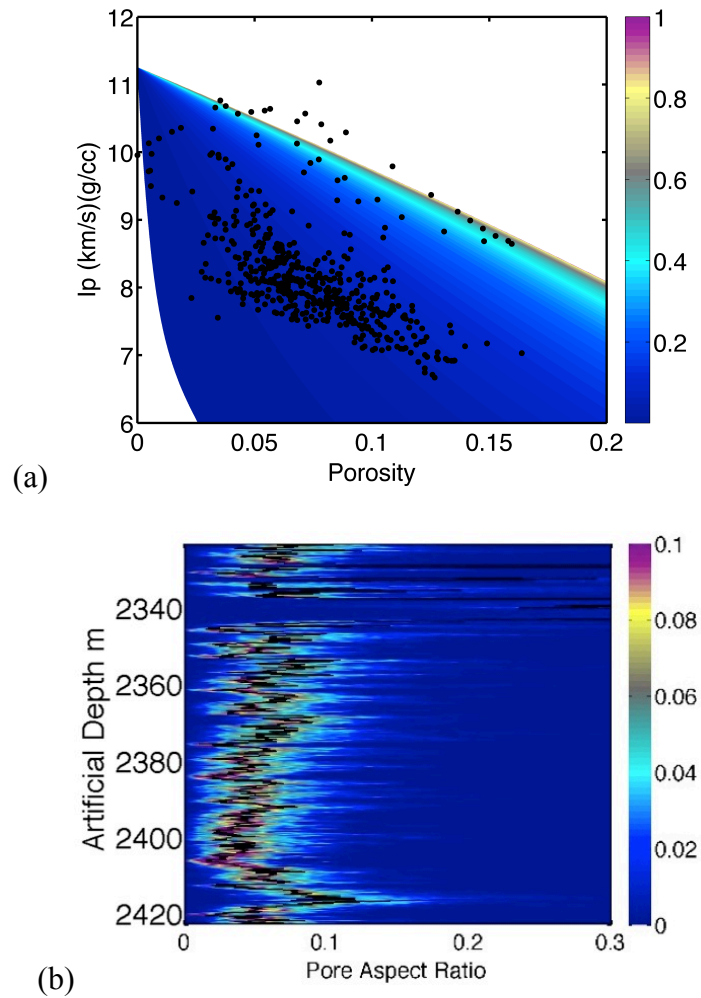
Figure C.6: (a) Crossplot of S-impedance versus porosity, colored by pore shape, with possible aspect ratio values from 0.001 to 1. Background color shows the variation for aspect ratio. Black points are from well log data. (b) Pore aspect ratio estimation. The background color represents probability. Black curve marks the pore aspect ratio estimation with the highest probability.
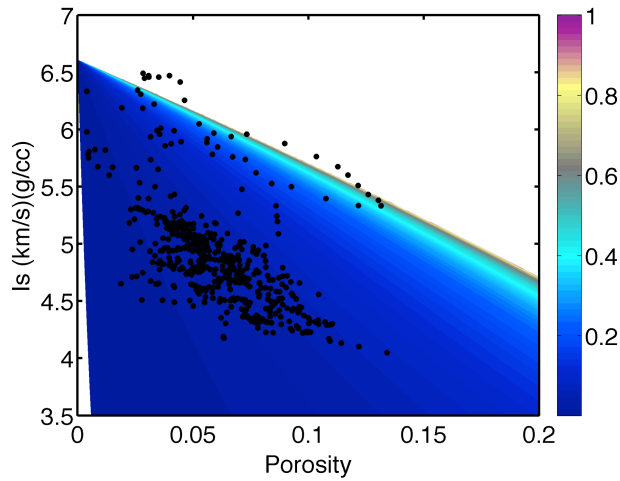
Figure C.7: Crossplot of S-impedance versus porosity, colored by pore shape, with possible aspect ratio values from 0.001 to 1. Background color shows the variation for aspect ratio. Black points are from well log data.

As conclusion, this study introduced a method that combines rock-physics modeling with a grid search method to estimate independently the porosity and pore aspect ratio for the Haynesville Shale. The self-consistent model provided constraints on the composition and pore shape based on P-impedance. The rock-physics modeling P-impedance with composition and pore shape constraints matched the well log measured P-impedance in terms of both variation trend and amplitude. The matching between the rock-physics modeling results and the log measurements provided porosity estimation and pore shape estimation separately. The porosity estimation matched with the observed porosity in terms of both overall trend and absolute value. The pore aspect ratio estimation was about 0.05, which is consistent with the fact that the pores in the Haynesville Shale are mostly flattened.

Appendix D: Chapman's Model

In Chapman's (2003) model, the following equations (equations D1–D5) were used to calculate the five independent stiffness tensor components. These equations are the same as equations 51, 52, 54, 59, and 61 in Chapman (2003). The stiffness components calculated from equations D1–D5 are complex numbers. The real parts provide frequency-dependent velocities, and the imaginary parts give frequency-dependent attenuation. The five stiffness tensor components (C_{11}, C_{33}, C_{44}, C_{66}, and C_{13}) are

$$C_{11} = (\lambda + 2\mu) - \phi_c[\frac{L_2}{\sigma_c} + \frac{32}{15}\frac{1-\nu}{(2-\nu)\pi r}\mu - (\frac{L_2}{\sigma_c} + \kappa)G_1 - (\frac{3\kappa^2}{\sigma_c} + 3\kappa)G_2 - (\frac{\lambda\kappa}{\sigma_c} + \lambda)G_3]$$

$$-\phi_p[\frac{3}{4\mu}\frac{1-\nu}{1+\nu}(3\lambda^2 + 4\lambda\mu + \frac{36+20\nu}{7-5\nu}\mu^2) - (1+\frac{3\kappa}{4\mu})(3\kappa D_1 + \lambda D_2)]$$

$$-\phi_f[\frac{\lambda^2}{\sigma_c} - (\frac{3\lambda\kappa}{\sigma_c} + 3\kappa)F_1 - (\frac{\lambda^2}{\sigma_c} + \lambda)F_2] \qquad ,\text{(D1)}$$

$$C_{33} = (\lambda + 2\mu) - \phi_c[\frac{L_2}{\sigma_c} + \frac{32}{15}\frac{1-\nu}{(2-\nu)\pi r}\mu - (\frac{L_2}{\sigma_c} + \kappa)G_1 - (\frac{3\kappa^2}{\sigma_c} + 3\kappa)G_2$$

$$-(\frac{(\lambda+2\mu)\kappa}{\sigma_c} + \lambda + 2\mu)G_3]$$

$$-\phi_p[\frac{3}{4\mu}\frac{1-\nu}{1+\nu}(3\lambda^2 + 4\lambda\mu + \frac{36+20\nu}{7-5\nu}\mu^2) - (1+\frac{3\kappa}{4\mu})(3\kappa D_1 + (\lambda+2\mu)D_2)]$$

$$-\phi_f[\frac{(\lambda+2\mu)^2}{\sigma_c} - (\frac{3(\lambda+2\mu)\kappa}{\sigma_c} + 3\kappa)F_1 - (\frac{(\lambda+2\mu)^2}{\sigma_c} + (\lambda+2\mu)F_2] \qquad ,\text{(D2)}$$

$$C_{44} = \mu - \phi_c\left[\frac{4}{15}\frac{\mu^2}{\sigma_c}(1-G_1) + \frac{8}{5}\frac{1-v}{(2-v)\pi r}\mu\right] - 15\phi_p\left[\frac{1-v}{7-5v}\mu - \phi_f\frac{4(1-v)}{(2-v)\pi r}\mu\right]$$, (D3)

$$C_{12} = \lambda - \phi_c\left[\frac{L_4}{\sigma_c} - \frac{16}{15}\frac{1-v}{(2-v)\pi r}\mu - (\frac{L_4}{\sigma_c}+\kappa)G_1 - (\frac{3\kappa^2}{\sigma_c}+3\kappa)G_2 - (\frac{\lambda\kappa}{\sigma_c}+\lambda)G_3\right]$$

$$-\phi_p\left[\frac{3}{4\mu}\frac{1-v}{1+v}(3\lambda^2+4\lambda\mu - \frac{4(1+5v)}{7-5v}\mu^2) - (1+\frac{3\kappa}{4\mu})(3\kappa D_1 + \lambda D_2)\right]$$

$$-\phi_f\left[\frac{\lambda^2}{\sigma_c} - (\frac{3\lambda\kappa}{\sigma_c}+3\kappa)F_1 - (\frac{\lambda^2}{\sigma_c}+\lambda)F_2\right]$$, (D4)

$$C_{13} = \lambda - \phi_c\left[\frac{L_4}{\sigma_c} - \frac{16}{15}\frac{1-v}{(2-v)\pi r}\mu - (\frac{L_4}{\sigma_c}+\kappa)G_1 - (\frac{3\kappa^2}{\sigma_c}+3\kappa)G_2 - (\lambda+\mu)(1+\frac{\kappa}{\sigma_c})G_3\right]$$

$$\frac{3}{}-\phi_p\left[\frac{3}{4\mu}\frac{1-v}{1+v}(3\lambda^2+4\lambda\mu + \frac{4(1+5v)}{7-5v}\mu^2) - (1+\frac{3\kappa}{4\mu})(3\kappa D_1 + (\lambda+\mu)D_2)\right]$$

$$-\phi_f\left[\frac{\lambda(\lambda+2\mu)}{\sigma_c} - 3\kappa(1+\frac{\lambda+\mu}{\sigma_c})F_1 - (\frac{\lambda(\lambda+\mu)}{\sigma_c}+\lambda+\mu)F_2\right]$$. (D5)

Contained in equations D1–D5 are Lame's constant (λ), the shear modulus (μ), and Poisson's ratio of the matrix material (v). Furthermore, r is the aspect ratio for cracks and fractures, ϕ_p is round pore porosity, ϕ_c is crack porosity, and ϕ_f is fracture porosity and

$$\sigma_c = \frac{\pi\mu r}{2(1-v)}$$

$$\kappa = \lambda + \frac{2}{3\mu}$$. (D6)

The D_1 and D_2 are terms to calculate pore pressure:

$$D_1 = [(1-\iota)\gamma + \frac{(1-\iota)\beta}{1+i\omega\tau_f} + (\iota + \frac{\iota\beta}{1+i\omega\tau_f})(\frac{1+i\omega\gamma\tau_m}{1+i\omega\tau_m})]^{-1}$$

$$\times [\frac{\iota}{3(1+K_c)} + (1-\iota)\gamma' - \frac{i\omega\tau_m}{1+i\omega\tau_m} \times (\frac{1}{3(1+K_c)} - \gamma')(\iota + \frac{\iota\beta}{1+i\omega\tau_f})]$$

(D7)

$$D_2 = [(1-\iota)\gamma + \frac{(1-\iota)\beta}{1+i\omega\tau_f} + (\iota + \frac{\iota\beta}{1+i\omega\tau_f})(\frac{1+i\omega\gamma\tau_m}{1+i\omega\tau_m})]^{-1} \times (\frac{\beta}{(1+K_c)(1+i\omega\tau_f)}).$$

Crack pressure comes from the G_1, G_2, and G_3 are terms as

$$G_1 = \frac{i\omega\tau_m}{(1+K_c)(1+i\omega\tau_m)}$$

$$G_2 = \frac{1+i\omega\gamma\tau_m}{1+i\omega\tau_m}D_1 - \frac{i\omega\tau_m\gamma'}{1+i\omega\tau_m}$$

(D8)

$$G_3 = \frac{1+i\omega\gamma\tau_m}{1+i\omega\tau_m}D_2 \ .$$

The F_1 and F_2 terms provide the fracture pressure

$$F_1 = \frac{1}{1+i\omega\tau_f}[\frac{1+i\omega\gamma\tau_m}{1+i\omega\tau_m}\iota D_1 + (1-\iota)D_1 + \frac{i\omega\tau_m}{1+i\omega\tau_m}(\frac{1}{3(1+K_c)} - \gamma')]$$

$$F_2 = \frac{1}{1+i\omega\tau_f}[\frac{i\omega\tau_f}{1+K_c} + \iota\frac{1+i\omega\gamma\tau_m}{1+i\omega\tau_m}D_2 + (1-\iota)D_2]$$

(D9)

In equations D7–D9, ω is frequency, and τ_m and τ_f are relaxation-time terms for cracks and fractures that account for squirt flow, which depend on crack/fracture size, fluid viscosity, grain size, and matrix bulk and shear moduli. In addition, these equations contain

$$K_c = \frac{\sigma_c}{K_f},$$

(D10)

$$\gamma = \frac{3 p_v \sigma_c (1 + K_p)}{4 \mu c_v (1 + K_c)},$$ (D11)

$$\gamma' = \gamma \frac{1 - v}{1 + v} \frac{1}{1 + K_p},$$ (D12)

$$K_p = \frac{4\mu}{3K_f},$$ (D13)

$$\iota = \frac{\frac{4}{3} \pi \varepsilon}{\frac{4}{3} \pi \varepsilon + \phi_p},$$ (D14)

and

$$\beta = \frac{\frac{4}{3} \pi \varepsilon_f}{\frac{4}{3} \pi \varepsilon + \phi_p},$$ (D15)

where K_f is bulk modulus of fluid and p_v and c_v are volumes of individual pores and cracks, respectively. The two terms ι and β are related to crack density (ε) and fracture density (ε_f).

Finally, L_2, L_3, and L_4 are calculated from λ and μ by

$$L_2 = \lambda^2 + \frac{4}{3} \lambda \mu + \frac{4}{5} \mu^2$$

$$L_3 = 4(\lambda^2 + \frac{4}{3} \lambda \mu + \frac{8}{15} \mu^2)$$ (D16)

$$L_4 = \lambda^2 + \frac{4}{3} \lambda \mu + \frac{4}{15} \mu^2$$

163

References

Aki, K., and P. G. Richards, 2002, Quantitative Seismology, 2nd Edition: W. H. Freeman and Company.

Archie, G. E., 1942, The electrical resistivity log as an aid in determining some reservoir characteristics: *Petroleum Transactions of the American Institute of Mining Engineers*, **146**, 54–62.

Avseth, P., J. Dvorkin, G. Mavko, and J. Rykkje, 2000, Rock physics diagnostic of North Sea sands: Link between microstructure and seismic properties: *Geophysical Research Letters*, **27**, 2761–2764.

Avseth, P., A. Dræge, A.-J. van Wijngaarden, T. A. Johansen, and Jorstad, A., 2008, Shale rock physics and implications for AVO analysis: A North Sea demonstration: *The Leading Edge*, **27**(**6**), 788–797.

Bachrach, R., 2006, Joint estimation of porosity and saturation using stochastic rock-physics modeling: *Geophysics*, **71**, o53–o63.

Bachrach, R., K. Osypov, D. Nichols, Y. Yang, Y. Liu, and M. Woodward, 2013, Applications of deterministic and stochastic rock physics modelling to anisotropic velocity model building: *Geophysical Prospecting*, **61**, 404–415, doi: 10.1111/j.1365-2478.2012.01133.x

Backus, G., 1962. Long-wave elastic anisotropy produced by horizontal layering: *Journal of Geophysical Research*, **67**, 4427-4440.

Bai, J.-Y., C.-Q .Yue, Y.-Q. Liang, Z.-X. Song, S. Ling, Y. Zhang, and W. Wu, 2013, Variable aspect ratio method in the Xu-White model for shear-wave velocity estimation: *Journal of Geophysics and Engineering*, **10**, doi: 10.1088/1742-2132/10/3/035008.

Batzle, M., D.-H. Han, and R. Hofmann, 2006, Fluid mobility and frequency-dependent seismic velocity–Direct measurements: *Geophysics*, **71**, N1–N9.

Bayuk, I., M. Ammerman, and E. M. Chesnokov, 2007, Elastic moduli of anisotropic clay: *Geophysics*, **72**, D107–D117.

Becker, S.P., P. Eichhubl, S.E. Lauback, R.M. Reed, R.H. Lander, and R.J. Bodnar, 2010, A 48 m.y. history of fracture opening, temperature, and fluid pressure: Cretaceous Travis Peak Formation, East Texas basin: *Geological Society of America Bulletin*, **122**, 1081–1093, doi 10.1130/B30067.1.

Berryman, J. G., 1980, Long-wavelength propagation in composite elastic media: *Journal of the Acoustical Society of America*, **68**, 1809–1831.

Berryman, J. G., 1995, Mixture theories for rocks. In Rock Physics and Phase Relations: a Handbook of Physical Constants, ed. T.J. Ahrens: *American Geophysical Union Reference Shelf*, **3**, 205–228.

Blangy, J. P., 1992, Integrated seismic lighologic interpretation: the petrophycical basis, PhD thesis, Stanford University.

Brie, A., F. Pampuri, A. F. Marsala, and O. Meazza, 1995, Shear sonic interpretation in gas-bearing sands: *SPE 30595*, 701–710.

Carmichael, R. S., 1989, Practical handbook of physical properties of rocks and minerals, Boca Raton, FL: CRC Press.

Castagna, J. P., M. L. Batzle, and R. L. Eastwood, 1985, Relationships between compressional-wave and shear-wave velocities in clastic silicate rocks: *Geophysics*, **50**, 571–581.

Chalmers, G. R., R. M. Bustin, and I. M. Power, 2012, Characterization of gas shale pore systems by porosimetry, pycnometry, surface area, and field emission scanning electron microscopy/transmission electron microscopy image analyses: Examples from the Barnett, Woodford, Haynesville, Marcellus, and Doig units: *AAPG Bulletin*, **96**, 1099–1119, doi: 10.1306/10171111052.

Chapman, M., 2001, Modelling the wide-band laboratory response of rock samples to fluid and pressure changes, PhD thesis, University of Edinburgh.

Chapman, M., Zatsepin, S.V. & Crampin, S., 2002. Derivation of a microstructural poroelastic model, *Geophysical Journal International*, **151**, 427–451.

Chapman, M., 2003, Frequency-dependent anisotropy due to meso-scale fractures in the presence of equant porosity: *Geophysical Prospecting*, **51**, 369–379.

Chapman, M., 2009, Modeling the effect of multiple sets of mesoscale fractures in porous rock on frequency-dependent anisotropy: *Geophysics*, **74**, D97–D103.

Chopra, S., R. K. Sharma, and K. J. Marfurt, 2013, Current workflows for shale gas reservoir characterization: Unconventional Resources Technology Conference, Denver, Co, USA.

Ciz, R. and S. A. Shapiro, 2009, Stress-dependent anisotropy in transversely isotropic rock: Comparison between theory and laboratory experiment on shale: *Geophysics*, **74**, D7–D12.

Curtis, J., 2002, Fractured shale-gas systems: *AAPG Bulletin*, **86**, 1921–1938.

Curtis, M. E., R. J. Ambrose, C. H. Sondergeld, and C. S. Rai, 2010, Structural characterization of gas shales on the micro- and nano-scales: *SPE Paper 138145*.

Delle Piane, C., D. N. Dewhurst, A. F. Siggins, and M. D. Raven, 2011, Stress-induced anisotropy in brine saturated shale: *Geophysical Journal International*, **184**, 897–906.

Dræge, A.M. Jakobsen, and T. A. Johansen, 2006, Rock physics modeling of shale diagenesis: *Petroleum Geoscience*, **12**, 49–57.

Dvorkin, J., and A. Nur, 1993, Dynamic Poroelasticity: A unified model with the squirt and the Biot mechanisms: *Geophysics*, **58**, 524–533.

Dvorkin J., R. Nolen-Hoeksema, and A. Nur, 1994, The squirt-flow mechanism: Macroscopic description: *Geophysics*, **59**, 428–438.

Dvorkin, J., and A. Nur, 1996, Elasticity of high-porosity sandstones: theory for two North Sea datasets: *Geophysics*, **61**, 1363–1370.

Eastwood, R., and U. Hammes, 2011, Log model development for the Bossier and Haynesville Shales: *SPWLA 52nd Annual Logging Symposium*, Colorado Springs, Co, USA.

Eberli, G. P., G. T. Baechle, F. S. Anselmetti, and M. L. Incze, 2003, Factors controlling elastic properties in carbonate sediments and rocks: *The Leading Edge*, **22**, 654–660.

Eidsvik, J., P. Avseth, H. More, T. Mukerji, and G. Mavko, 2004, Stochastic reservoir characterization using prestack seismic data: *Geophysics*, **69**, 978–993.

Ewing, T. E., 2001, Review of Late Jurassic depositional and potential hydrocarbon plays, northern Gulf of Mexico basin: *Gulf Coast Association of Geological Societies Transactions*, **51**, 85–96.

Gal, D., J. Dvorkin, and A. Nur, 1998, A physical model for porosity reduction in sandstones: *Geophysics*, **63**, 454–459.

Gale, J. F. W., R. M. Reed, and J. Holder, Nature fractures in the Barnett Shale and their importance for hydraulic fracture treatments: *AAPG Bulletin*, **91**, 603–622.

Gassmann, F., 1951, Uber die elastizitat poroser medien: *Veirteljahrsschrift der Naturforschenden Gesellschaft in Zurich*, **96**, 1–23.

Grana, D., and E. Della Rossa, 2010, Probabilistic reservoir-properties estimation integrating statistical rock physics with seismic inversion: *Geophysics*, **75**, o21–o37.

Greenberg, M. L., and J. P. Castagna, 1992, Shear-wave velocity estimation in porous rocks; theoretical formulation, preliminary verification and applications: *Geophysical Prospecting*, **40**, 195–209.

Guo, Z., X.-Y. Li, C. Liu, X. Feng, and Y. Shen, 2013, A shale rock physics model for analysis of brittleness index, mineralogy and porosity in the Barnett Shale: *Journal of Geophysics and Engineering*, **10**, doi: 10.1088/1742-2132/10/2/025006.

Hammes, U., H. S. Hamlin, and T. E. Ewing, 2011, Geologic analysis of the Upper Jurassic Haynesville Shale in east Texas and west Louisiana: *AAPG Bulletin*, **95**, 1643–1666.

Hampson, D. P., B. H. Russell, and B. Bankhead, 2005, Simultaneous inversion of pre-stack seismic data: 75th Annual International Meetings, SEG, Expanded Abstracts, 1633–1636.

Han, D.-H., A. Nur, and D. Morgan, 1986, Effects of porosity and clay content on wave velocities in sandstones: *Geophysics*, **51**, 2093–2107.

Hornby, B., L. M. Schwartz, and J. A. Hudson, 1994, Anisotropic effective–medium modeling of the elastic properties of shales: *Geophysics*, **59**, 1570–1583.

Horne, S., J. Walsh, and D. Miller, 2012, Elastic anisotropy in the Haynesville Shale from dipole sonic data: *First Break*, **30**, 37–41.

Hudson, J. A., 1980, Overall properties of a cracked solid: *Mathematical proceedings of the Cambridge Philosophical Society*, **88**, 371–384.

Jenkins, J., D. Johnson, L. L. Ragione, and H. Makse, 2005, Fluctuations and the effective moduli of an isotropic, random aggregate of identical, frictionless spheres: *Journal of Mechanical and Physical Solids*, **53**, 197–225.

Jiang, M., and K. T. Spikes, 2011, Pore-shape and composition effect on rock-physics modeling in the Haynesville Shale: 81st Annual International Meetings, SEG, Expanded Abstracts **30**, 2079, doi:10.1190/1.3627618

Jiang, M., and K. T. Spikes, 2012, Estimation of the porosity and pore aspect ratio of the Haynesville Shale using the self-consistent model and a grid search method: 82nd Annual International Meetings, SEG, Expanded Abstracts, http://library.seg.org/doi/abs/10.1190/segam2012-0134.1.

Jiang, M., and K. T. Spikes, 2013a, Estimation of reservoir properties of the Haynesville Shale by using rock physics modeling and grid searching: *Geophysical Journal International*, **195**, 315-329.

Jiang, M., and K. T. Spikes, 2013b, Correlation between rock properties and spatial variations in seismic attributes for unconventional gas shales – a case study on the Haynesville Shale: 83rd Annual International Meetings, SEG, Expanded Abstracts, http://dx.doi.org/10.1190/segam2013-0187.1.

Knight, R., and R. Nolen-Hoeksema, 1990, A laboratory study of the dependence of elastic wave velocities on pore scale fluid distribution: *Geophysical Research Letters*, **17**, 1529–1532.

Koesoemadinata, A., G. El-Kaseeh, N. Banik, J. Dai, M. Egan, A. Gonzalez, and K. Tamulonis, 2011, Seismic reservoir characterization in Marcellus shale: 81st Annual International Meetings, SEG, Expanded Abstract, http://dx.doi.org/10.1190/1.3627970.

Kuila, U., D. N. Dewhurst, A. F. Siggins, and M. D. Raven, 2011, Stress anisotropy and velocity anisotropy in low porosity shale: *Tectonophysics*, **503**, 34–44.

Kuster, G. T., and M. N. Toksöz, 1974, Velocity and attenuation of seismic waves in two-phase media: *Geophysics*, **39**, 587–618.

LaValle, S. M., M. S. Branicky, and S. R. Lindemann, 2004, On the relationship between classical grid search and probabilistic roadmaps: *International Journal of Robotics Research*, **23**, 673–692.

Loseth, H., L. Wensaas, M. Gading, K. Duffaut, and M. Springer, 2011, Can hydrocarbon source rocks be identified on seismic data?: *Geology*, **39**, 1167–1170, doi: 10.1130/G32328.1.

Lucier, A. M., R. Hofmann, and L. T. Bryndzia, 2011, Evaluation of variable gas saturation on acoustic log data from the Haynesville Shale gas play, NW Louisiana, USA: *The Leading Edge*, **30**, 300–311.

Mavko, G., T. Mukerji, and J. Dvorkin, 2009, The Rock Physics Handbook: Tools for Seismic Analysis of Porous Media: Cambridge, University Press, 511 p.

Mindlin, R. D., 1949, Compliance of elastic bodies in contact: *Journal of Applied Mechanics*, **16**, 259–268.

Moyano, B., K. T. Spikes, T. A. Johansen, and N. H. Mondol, 2012, Modeling compaction effects on the elastic properties of clay-water composites: *Geophysics*, **77**, D171–D183.

Mukerji, T., A. Jorstad, P. Avseth, G. Mavko, and J. R. Granli, 2001, Mapping lithofacies and pore-fluid probabilities in a North Sea reservoir: seismic inversions and statistical rock physics: *Geophysics*, **66**, 988–1001.

Nadri, D., J. Sarout, A. Bona, and D. Dewhurst, 2012, Estimation of the anisotropy parameters of transversely isotropic shales with a tilted symmetry axis: *Geophysical Journal International*, **190**, 1197–1203.

Norris, A. N., 1985, A differential scheme for the effective moduli of composites: *Mechanical Materials*, **4**, 1–16.

Norris, A. N., and D. L. Johnson, 1997, Nonlinear elasticity of granular media: *Journal of Applied Mechanics*, **64**, 39–49.

Nunn, J., 2011, Burial and thermal History of the Haynesville Shale: Implications for gas generation, overpressure, and natural hydrofracture (abs.): AAPG 2011 Meeting Abstracts, Houston, 90124.

O'Connell, R. J. and B. Budiansky, 1974, Seismic velocities in dry and saturated cracked solids: *Journal of Geophysical Research*, **82**, 5719–5735.

Pervukhina, M, B. Gurevich, P. Golodoniuc, and D. N. Dewhurst, 2011, Parameterization of elastic stress sensitivity in shales: *Geophysics*, **76**, WA147–WA155.

Rimstad, K., P. Avseth, and H. More, 2012, Hierarchical Bayesian lithology/fluid prediction: A North Sea case study: *Geophysics*, **77**, B69–B85.

Roth, M., 2011, North American shale gas reservoirs − similar, yet so different: AAPG Convention, 12–15 September, Calgary, Canada.

Saffer, D. M., and C. Marone, 2003, Comparison of smectite- and illite-rich gouge frictional properties: application to the updip limit of the seismogenic zone along subduction megathrusts: *Earth and Planet Science Letters*, **215**, 219–235.

Sayers, C., 2010, Geophysics under stress: Geomechanical applications of seismic and borehole acoustic waves: SEG Distinguished Instructor Series, No. 13.

Sayers, C. M., and L. D. den Boer, 2011, Rock physics-based relations for density and S-velocity versus P-velocity in deepwater subsalt Gulf of Mexico shales: *The Leading Edge*, **30**, 1376–1381.

Sayers, C. M., 2013, The effect of anisotropy on the Young's moduli and Poisson's ratios of shales: *Geophysical Prospecting*, **61**, 416–426, doi: 10.1111/j.1365-2478.2012.01130.x

Schoenberg, M., and J. Douma, 1988, Elastic wave propagation in media with parallel fractures and aligned cracks: *Geophysical Prospecting*, **36**, 571–590.

Sen, M. and P. L. Stoffa, 1995, Global optimization methods in geophysical inversion, ELSEVIER Science.

Sena, A., G. Castillo, K. Chesser, S. Voisey, J. Estrada, J. Carcuz, E. Carmona, and P. Hodgkins, 2011, Seismic reservoir characterization in resource shale plays: stress analysis and sweet spot discrimination: *The Leading Edge*, **30**, 758-764.

Spikes, K. T. and M. Jiang, 2013, Rock physics relationships between elastic and reservoir properties in the Haynesville Shale: *AAPG Memoir*, **105**, 189–203.

Spikes, K. T., T. Mukerji, J. Dvorkin, and G. Mavko, 2007, Probabilistic seismic inversion based on rock-physics models: *Geophysics*, **72**, R87–R97.

Smith, T. M., C. H. Sondergeld, and C. S. Rai, 2003, Gassmann fluid substitutions: A tutorial: *Geophysics*, **68**, 430-440.

Theng, B. K. G., 1974, The chemistry of clay-organic reactions, pp. 343, Hilger, London.

Thomsen, L., 1986, Weak elastic anisotropy: *Geophysics*, **51**, 1954–1966.

Tosaya, C. A., 1982, Acoustical properties of clay-bearing rocks: PhD dissertation, Stanford University, Stanford, 136 p.

Tosaya, C. A., and A. Nur, 1982, Effects of diagenesis and clays on compressional velocities in rocks: *Geophysical Research Letters*, **9**, 5–8.

Tsvankin, I., 2012, Seismic signatures and analysis of reflection data in anisotropic media: SEG Geophysical References Series **19**, 438 p.

Vanorio, T., M. Prasad, and A. Nur, 2003, Elastic properties of dry clay mineral aggregates, suspensions and sandstones: *Geophysical Journal International*, **155**, 319–326.

Vanorio, T., T. Mukerji, and G. Mavko, 2008, Emerging methodologies to characterize the rock physics properties of organic-rich shales: *The Leading Edge*, **27**(6), 780–787.

Wang, F. P., and U. Hammes, 2010, Effects of reservoir factors on Haynesville fluid flow and production: *World Oil*, **231**, D3–D6.

Wang, Z., H. Wang, and M. E. Cates, 2001, Effective elastic properties of solid clays: *Geophysics*, **66**, 428–440.

Ward, J. A., 2010, Kerogen density in the Marcellus Shale: *SPE paper 131767*.

Whitney, G., 1990, Role of water in the smetite-to-illite reaction: *Clays and Clay Minerals*, **38**, 343–350.

Xu, S., and R. E. White, 1995, A new velocity for clay sand mixtures: *Geophysical Prospecting*, **43**, 91–118.

Xu, S., and R. E. White, 1996, A physical model for shear-wave velocity predicting: *Geophysical Prospecting*, **44**, 687–717.

Yilmaz, O., 2001, Seismic Data Analysis: Processing, Inversion, and Interpretation of Seismic Data, Society of Exploration Geophysicists, Tulsa.

Zhu, Y., E. Liu, A. Martinez, M. A. Payne, and C. E. Harris, 2011, Understanding geophysical responses of shale-gas plays: *The Leading Edge*, **30**, 332–338.

Vita

Meijuan Jiang received her B.S. degree in Geophysics from the University of Science and Technology of China in Hefei, Anhui, China in 2005. She received a M.S. degree in Statistics in May 2010 at University of Illinois at Urbana-Champaign. In August 2010, she entered the Jackson School of Geosciences at the University of Texas at Austin as a Ph.D. student.

Email: jmjzsx@gmail.com

This dissertation was typed by Meijuan Jiang.